

**AFRL-ML-WP-TR-1999-4026**

**CORE PROGRAMS OF HIGH-PERFORMANCE  
COMPOSITE MATERIALS**

**A. CRASTO, D. ANDERSON, R. ESTERLINE,  
K. HAN, C. HILL, R. KIM, W. LEE, W. PRICE,  
B. RICE, A. ROY, D. SCHMIDT, K. THORP,  
AND J. WHITNEY**



**UNIVERSITY OF DAYTON RESEARCH INSTITUTE  
300 COLLEGE PARK AVENUE  
DAYTON, OH 45469-0168**

**DECEMBER 1998**

**INTERIM REPORT FOR 09/15/1997 – 09/14/1998**

**APPROVED FOR PUBLIC RELEASE; DISTRIBUTION UNLIMITED.**

**MATERIALS AND MANUFACTURING DIRECTORATE  
AIR FORCE RESEARCH LABORATORY  
AIR FORCE MATERIEL COMMAND  
WRIGHT-PATTERSON AIR FORCE BASE OH 45433-7750**

**DTIC QUALITY INSPECTED 4**

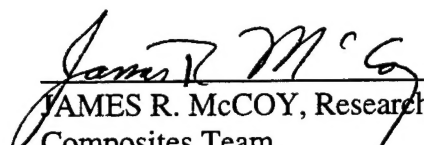
**19990820 085**


## NOTICE

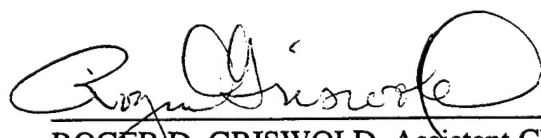
Using Government drawings, specifications, or other data included in this document for any purpose other than Government procurement does not in any way obligate the U.S. Government. The fact that the Government formulated or supplied the drawings, specifications, or other data does not license the holder or any other person or corporation; or convey any rights or permission to manufacture, use, or sell any patented invention that may relate to them.

This report is releasable to the National Technical Information Service (NTIS). At NTIS, it will be available to the general public, including foreign nations.

This technical report has been reviewed and is approved for publication.

  
JAMES R. McCOY, Research Chemist  
Composites Team  
Structural Materials Branch

  
L. SCOTT THEIBERT, Chief  
Structural Materials Branch  
Nonmetallic Materials Division

  
ROGER D. GRISWOLD, Assistant Chief  
Nonmetallic Materials Division  
Materials and Manufacturing Directorate

Do not return copies of this report unless contractual obligations or notice on a specific document requires its return.

REPORT DOCUMENTATION PAGE			Form Approved OMB No. 0704-0188	
Public reporting burden for this collection of information is estimated to average 1 hour per response, including the time for reviewing instructions, searching existing data sources, gathering and maintaining the data needed, and completing and reviewing the collection of information. Send comments regarding this burden estimate or any other aspect of this collection of information, including suggestions for reducing this burden, to Washington Headquarters Services, Directorate for Information Operations and Reports, 1215 Jefferson Davis Highway, Suite 1204, Arlington, VA 22202-4302, and to the Office of Management and Budget, Paperwork Reduction Project (0704-0188), Washington, DC 20503.				
1. AGENCY USE ONLY (Leave blank)		2. REPORT DATE DECEMBER 1998		3. REPORT TYPE AND DATES COVERED INTERIM REPORT FOR 09/15/1997 - 09/14/1998
4. TITLE AND SUBTITLE CORE PROGRAMS OF HIGH-PERFORMANCE COMPOSITE MATERIALS			5. FUNDING NUMBERS C F33615-95-D-5029 PE 62102 PR 4347 TA 34 WU 10	
6. AUTHOR(S) A. CRASTO, D. ANDERSON, R. ESTERLINE, K. HAN, C. HILL, R. KIM, W. LEE, W. PRICE, B. RICE, A. ROY, D. SCHMIDT, K. THORP AND J. WHITNEY				
7. PERFORMING ORGANIZATION NAME(S) AND ADDRESS(ES) UNIVERSITY OF DAYTON RESEARCH INSTITUTE 300 COLLEGE PARK AVENUE DAYTON, OH 45469-0168			8. PERFORMING ORGANIZATION REPORT NUMBER  UDR-TR-98-00153	
9. SPONSORING/MONITORING AGENCY NAME(S) AND ADDRESS(ES) MATERIALS AND MANUFACTURING DIRECTORATE AIR FORCE RESEARCH LABORATORY AIR FORCE MATERIEL COMMAND WRIGHT-PATTERSON AFB, OH 45433-7750 POC: JAMES R. McCOY, AFRL/MLBC, 937-255-9063			10. SPONSORING/MONITORING AGENCY REPORT NUMBER  AFRL-ML-WP-TR-1999-4026	
11. SUPPLEMENTARY NOTES				
12a. DISTRIBUTION AVAILABILITY STATEMENT  APPROVED FOR PUBLIC RELEASE; DISTRIBUTION UNLIMITED			12b. DISTRIBUTION CODE	
13. ABSTRACT (Maximum 200 words) Evaluation of composites and components continued from the previous contract. Materials used to RTM carbon-carbon preforms were evaluated. RDS data analysis software was written and modulated DSC evaluated as an analysis tool. Bridge rehabilitation successfully tested a new embedded rod technique. The measured CTE changes of composites were found to correlate with cracking densities. Damage during loading around holes in composites consisted of longitudinal cracks and delaminations. Transverse cracking was also studied including using a local shear deformation theory. A cruciform sample allowed the fiber/matrix interfacial normal stress to be measured on model composites. Problems with current lap shear tests and alternatives were examined. Three-dimensional micromechanics of textile weaves was continued. The processing science of composites continues examining the causes of shrinkage, sensors for resin infusion, 3D flow models, and hardware to test these models. Encapsulated oxidants as a new way of stabilizing pitch was investigated; the stabilization of bicomponent pitch was also examined. A method to prepreg carbon fibers with pitch powder was demonstrated. C-C heat-exchanger components were examined by microscopy. A class of high-char yield resins was investigated as a carbon-carbon resin but not found suitable. Graphitic foam structures were quantified as functions of both blowing gas and net-shape processing techniques.				
14. SUBJECT TERMS carbon-carbon, carbon-epoxy, carbon fiber, carbonization, CTE, dimensional control, expert system, fabric, foams, graphite-epoxy, graphitic foams, infrastructure, mechanics modeling, microcellular, morphology, microscopy, oxidation, pitch, ply cracking, polyimides, prepreg, process modeling, qualitative process controls, sensors, shear testing, stabilization, thermal analysis, thermal cycling, thermosets, and XRD			15. NUMBER OF PAGES 158	
			16. PRICE CODE	
17. SECURITY CLASSIFICATION OF REPORT  UNCLASSIFIED		18. SECURITY CLASSIFICATION OF THIS PAGE  UNCLASSIFIED		19. SECURITY CLASSIFICATION OF ABSTRACT  UNCLASSIFIED
				20. LIMITATION OF ABSTRACT  SAR

## CONTENTS

Section		Page
	<b>EXECUTIVE SUMMARY</b>	<b>1</b>
<b>1</b>	<b>CHARACTERIZATION OF FIBERS/MATRIX RESINS AND COMPOSITES</b>	<b>4</b>
	1.1 Composite Mechanical Testing	4
	1.2 Characterization of Composites and their Constituents	4
	1.2.1 RTM Resins for Carbon-Carbon Materials	4
	1.2.2 Ad Hoc Programming for the Analysis of RDS Data	7
	1.3 Lifetime Prediction of Composite Performance	9
	1.4 Rehabilitation of Concrete Bridge Beams with Fiber-Reinforced Composites	11
<b>2</b>	<b>MECHANICS OF POLYMER-MATRIX COMPOSITES</b>	<b>17</b>
	2.1 Damage Development for Composite Laminates with Center Holes	17
	2.1.1 Experiment	19
	2.1.2 Results	20
	2.2 Changes in Laminate CTE Due to Microcracking	32
	2.2.1 Experiment	34
	2.2.2 Experimental Results	35
	2.3 Interfacial Normal Strength Evaluation in Unidirectional Glass/Epoxy Composites	37
	2.3.1 Experiment	39
	2.3.2 Analytical Background	41
	2.3.3 Results and Discussion	43
	2.4 Analysis of Bidirectional Laminates with Transverse Ply Cracks	47
	2.4.1 Effective Moduli	47
	2.4.2 Effective Thermal Expansion Coefficients	51
	2.5 Stress Analysis of Alternative Shear Tests	53
	2.5.1 Cylindrical Composite Lap Joints	53
	2.5.2 Analysis of a Composite Notched-Lap Joint Using Higher-Order Plate Theory	55
	2.6 Three-Dimensional Mixed Variational Micromechanics Model for Textile Composites	56



## CONTENTS (Continued)

Section		Page
<b>3</b>	<b>PROCESSING SCIENCE OF COMPOSITES</b>	<b>68</b>
3.1	Processing for Dimensional Control	68
3.1.1	Experimental Details	70
3.1.2	Cure of AS4/3501-6	72
3.1.3	Cure of IM7/977-3	74
3.1.4	Cure of IM7/5250-4	75
3.2	Integration of Sensors for Intelligent Composites Processing	76
3.2.1	Modeling Reaction Kinetics of Resin Systems with a Crystalline Phase	78
3.3	Composite Manufacturing Concepts for Reduced Cost	79
3.3.1	Material Characterizations	79
3.3.2	Modeling Manufacturing Composite Processes	80
3.3.3	Low-Cost Resin Infusion Processing	81
<b>4</b>	<b>CARBON-CARBON AND CARBONACEOUS MATERIALS</b>	<b>84</b>
4.1	Economical Carbon-Carbon	84
4.1.1	New Precursors for C-C	84
4.1.1.1	Carbonization/Graphitization of Pitch and Other C-C Precursors	84
4.1.1.2	Characterization of University of Akron Carbon Fibers	84
4.1.1.3	Evaluation of a Class of New High Char Yield Resins	84
4.1.2	New Processes for C-C	
4.1.2.1	Intelligent Processing of Carbon-Carbon	91
4.1.2.2	Stabilization of Pitch	91
4.1.2.3	Carbon-Carbon Heat Exchangers	93
4.1.2.4	Water-Based Suspension Prepregging of Pitch Powder	102
4.1.2.4.1	Jet-milling	103
4.1.2.4.2	Oxidation of powders	103
4.1.2.4.3	Preparation of suspension mixtures	104
4.1.2.4.4	Prepreg vertical die and spreader bar position	104
4.1.2.4.5	Air-comb fiber spreader	107
4.1.2.4.6	Results using vertical die	107
4.1.2.4.7	Horizontal prepregging bath	110
4.1.2.4.8	Panel fabrication	112

## CONTENTS (Concluded)

Section		Page
	4.1.2.5 Encapsulated Oxidants for Mesophase Pitch Stabilization	113
	4.1.2.5.1 Evaluation of composite specimen	114
	4.1.2.5.2 Moisture pickup of microcapsules	115
	4.1.2.5.3 Evaluation of heat-treatment process	116
4.2	Graphitic Foams	118
	4.2.1 Cellular Structure of Net-Shaped Pitch-Based Microcellular Carbon-Foams	119
	4.2.2 Characterization of Foams made with Various Blowing Gases	130
	4.2.3 Foam Structural Modeling	136
	4.2.4 X-ray Diffraction of Graphitic Foams from Several Sources	136
4.3	Technical Assessment of Critical AF Materials Issues and Opportunities	138
5	PUBLICATIONS AND PRESENTATIONS	140
6	REFERENCES	142

## FIGURES

Figure		Page
1	RDS Data for the EJ410b34m2 Nanocomposite Sample showing the Shifted Data Relative to 0°C with the Loss Modulus Shifted using the Storage Modulus Shift Factors	8
2	RDS Data for the EJ40000 Nanocomposite Sample showing the Shifted Young's Modulus Data Relative to 0°C	8
3	Selected RDS Storage Modulus Data for the EJ410b34m2 Nanocomposite Sample showing Anomalous Data at Lower Temperatures (Shifted Relative to 0°C)	10
4	Comparison of Maximum Bending Moments of 8.5-m Concrete Beams without External Reinforcement, with Composite Plate Reinforcement and with Composite Rod Reinforcement, vs. Measured Central Deflections	14
5	Comparison of Maximum Bending Moments of a Deteriorated 10.4-m Concrete Beam without External Reinforcement, vs. Measured Central Deflections	16
6	Comparison of Maximum Bending Moments of a Deteriorated 10.4-m Concrete Beam Externally Reinforced with Four Rods 0.625" in Diameter, vs. Measured Central Deflections	16
7	Comparison of Maximum Bending Moments of a Deteriorated 10.4-m Concrete Beam Externally Reinforced with Four Rods, Two of 0.625" Diameter and Two 0.75" Diameter, vs. Measured Central Deflections	17
8	Specimen Dimensions and Strain Gage Locations	20
9	Stress-Strain Curves for $[0]_{8T}$	21
10	Stress-Strain Curves for $[90]_{8T}$	21
11	Stress-Strain Curves for $[\pm 45]_{2S}$	22
12	Stress-Strain Curves for $[\pm 30/90_2]_S$	23
13	Stress-Strain Curves for $[0_2/90_2]_S$	24

## FIGURES (Continued)

Figure		Page
14	Stress-Strain Curves for $[0/90]_{2s}$	25
15	Radiographs of Damage: $[0]_{8T}$	27
16	Radiograph of Damage: $[\pm 45]_{2s}$	28
17	Radiographs of Damage: $[\pm 30/90_2]_s$	29
18	Radiographs of Damage: $[0_2/90_2]_s$	30
19	Radiograph of Damage: $[0/90]_{2s}$	31
20	Longitudinal Thermal Strain vs. Temperature for $[0]_{8T}$ after Subjecting to Thermal Cycles	36
21	Transverse Thermal Strain vs. Temperature for the $[0]_{8T}$ Laminate after Subjecting to Thermal Cycles	36
22	Thermal Strain vs. Temperature for the $[0/90]_{2s}$ Laminate after Subjecting to Thermal Cycles	38
23	Specimen Geometry: (a) Straight-Sided Specimen and (b) Cruciform Specimen	39
24	Comparison of Stress Concentration Factor in Model Single Fiber Composites	42
25	Stress-Strain Curves at Various Locations along the Fiber Length	44
26	Photograph Showing Failed Specimens	45
27	Photomicrograph Showing the Fracture Surface	46
28	Photomicrographs Showing Photoelastic Fringes for the Applied Stresses	46
29	Photomicrograph Showing the Separation of Fiber from the Matrix after Failure	48
30	A Representative Cross-Sectional Micrograph of a 8HS Woven T300/938 (Graphite/Epoxy) Composite after 50% of Failure Load	57

## FIGURES (Continued)

Figure		Page
31	(a) RVE of a 2D Textile Composite; (b) RVE of the Model	58
32	(a-f) Subregion Surfaces of the RVE	59
33	Sketch of the Experimental Setup to Measure the Buildup of Residual Strains During Composite Cure in an Autoclave	71
34	Plots of Strain Generated in a $[0]_{16}$ Composite of AS4/3501-6, Measured with Embedded Strain Gages, During Vacuum-Bag Cure in an Oven	72
35	Section of a Plot of Strains Generated in a $[0/90_3]_{48T}$ Laminate of AS4/3501-6, at Different Ply Interfaces, During Cure in an Autoclave	74
36	Plots of Strain Generated in a $[0]_{16}$ Composite of IM7/977-3, Measured with Embedded Strain Gages, During Cure in the Autoclave	75
37	Plots of Strain Generated in a $[0]_{16}$ Composite of IM7/5250-4, Measured with Embedded Strain Gages, During Cure and Postcure in the Autoclave	76
38	DSC Curve for 3:1 APcP Resin	87
39	Typical TGA Curve for APcP Resins	87
40	FTIR of Allyl-Chloride and Propargyl-Bromide	88
41	FTIR Scans of AcP Resin Before and After Distillation and After Partial Cure	89
42	FTIR Scans of PcP Resins as a Function of Cure State	90
43	Mass Change versus Time for a High Melting ( $285^{\circ}\text{C}$ ) Bicomponent Pitch	92
44	Mass Change versus Time for a Low Melting ( $241^{\circ}\text{C}$ ) Bicomponent Pitch	92
45	Schematic of the Carbon-Carbon Heat Exchanger Design	94

## FIGURES (Continued)

Figure		Page
46	Optical Micrograph (Crossed Polarized Light with a Wave Plate Converted to a Gray-Scale Image) of the Conventional C-C Parting Sheet/Fin Heat Exchanger	95
47	Typical SEM and Backscatter Image of the C-C Parting Sheet Separated from the Brazed Fins	98
48	SEM of Separated Parting Sheet and Fin	99
49	Backscatter SEM Image of Two Integral Construction Parting Sheet and Fins Brazed Together by their Parting Sheets	100
50	Optical Micrograph of C-C Parting Sheets Brazed Together	101
51	CT Cross Section of C-C Heat Exchanger (Color Removed and Contrast Inverted)	102
52	Vertical Infiltration Bath with Die	105
53	Spreader Bar Positions and Fiber Paths: (A) 1/2 Bars, (B) Standard Bars	106
54	Air-Comb Fiber Spreader	108
55	Fluorescence Illuminated Fiber Tow Cross Section showing Lack of Powder Infiltration	108
56	Polarized Light Image of Transverse Section showing Shrinkage Cracks between Tows	109
57	Arrangement of Horizontal Infiltration Bath	110
58	Fluorescence Image of Composite Fabricated with Encapsulated Oxidants	115
59	SEM Image of Microcapsules after Drying	116
60	Cutting Diagram for the Foam Samples: a) for Rectangular Blocks and b) for the Cylindrical Pieces	121
61	Photographs of "Net-Shaped" Foams	122

## FIGURES (Concluded)

Figure		Page
62	Archimedes "Apparent Porosity" Results by Sample and Location	124
63	SEM of Molded Foam: Typical Uniformity of all the Foam Samples	125
64	Average Bubble Sizes in the Center of the Foam Specimens as a Function of Viewing Direction	125
65	Fluorescent Micrographs of Foams: a) Typical Small-Celled Foam and b) Typical Large-Celled Foam	127
66	Average Bubble Sizes in the Central Part of the Foam Specimens as a Function of LOCATION from the Center of the Foam to the Outer Part (but not at the Edges)	128
67	Average Bubble Sizes in the Central Part of the Foam Specimens as a Function of POSITION from the Center of the Foam to the Outside Edge, Top Edge and Bottom Edge	128
68	Example of Crushed Cells in the Extruded Foam	129
69	Example of Occasional Very Large Cells	130
70	Volume Expansion during Foaming	131
71	Porosity Data for the Foams	132
72	Bulk Density Results for the Foams	132
73	Fluorescent Micrograph of Stabilized Helium Foams showing a) an Open Cellular Structure and b) a Collapsed Cellular Structure	135
74	Cell Size Results for the Foam Samples	135
75	Model Results for a Constant Volume Strut Expanding	137
76	D-Spacing versus Heat-Treatment Temperatures in AR Pitch-Based Fibers	137
77	Crystallite Sizes and Orientations versus Heat-Treatment Temperatures in AR Pitch-Based Fibers	138

## TABLES

Table		Page
1	Composite Mechanical Testing for the Period 15 Sep 97-14 Sep 98	5
2	Summary of Test Results	32
3	Elastic Properties of Constituents	42
4	Composite Panels Cured with Embedded Strain Gages	71
5	Summary of Transverse Residual Strains in Unidirectional Composites, Measured during Cure with Embedded Strain Gages	77
6	FTIR Bands of Allyl-Chloride and Propargyl-Bromide	89
7	Oxidation Weight Gains	103
8	Composition of Pitch Powder Suspensions used in Prepregging	105
9	Conditions for Pitch Powder Prepregging	106
10	Pressing Conditions for Vertically Prepregged Composites	109
11	Heat Treatment of Pitch and Oxidant Mixtures	117
12	Archimedes Displacement Average Results	124



## **FOREWORD**

This report was prepared by the University of Dayton Research Institute under Air Force Contract No. F33615-95-D-5029, Delivery Order No. 0001. The work was administered under the direction of the Nonmetallic Materials Division, Materials and Manufacturing Directorate, Air Force Research Laboratory, Air Force Materiel Command, with Dr. James R. McCoy (AFRL/MLBC) as Project Engineer.

This report was submitted in February 1999 and covers work conducted from 15 September 1997 through 14 September 1998.

## EXECUTIVE SUMMARY

Routine evaluation of composites and components continued from the previous contract. Routine evaluations of materials were facilitated by the production of several composite panels for mechanical testing. Materials used to RTM carbon-carbon preforms were examined by thermal analysis to help discover why they have a mass loss problem after carbonization. Software to analyze RDS data over a broad range of conditions and type was completed. Modulated DSC was evaluated as a means to make lifetime predictions of polyimides such as AFR700. The degradations observed at short time and elevated temperature were found to be different from long-time reactions; therefore, this technique was not considered applicable.

Also continued was evaluation of bridge rehabilitation materials. The elimination of large thin sheets bonded to concrete beams was accomplished with embedded rods. The same composite cross-sectional area was maintained while significantly reducing the amount of concrete preparation. The problem of holding large area panels against the concrete while curing the glue was eliminated as well as reducing the bond area between concrete and composite. The embedded rods also have the advantage that the bonding agent also forms the environmental barrier. Baseline mechanical testing showed this concept to perform as well as the flat panels.

Damage development around holes in composites was evaluated for inclusion in damage models. Interply delaminations and longitudinal cracking were measured. Strain gages allowed CTE changes in composites to be correlated with crack development. The CTE decreases as the number of cracks increase in agreement with model predictions. Transverse cracking was also studied as a function of steady-state mechanical loading and thermally-induced cracking. Interfacial normal stress was measured in glass/epoxy model

composites using a cruciform sample geometry. Many experimental difficulties were eliminated by using this technique. Transverse ply cracking was modeled using a local shear deformation theory. This model extends the predictions of modulus to include all nine elastic constants and the composite CTE changes.

Several shear tests were examined to find one that reduces the bending and free-edge stress concentrations of the conventional lap shear tests. A concentric cylindrical lap joint and a composite notched lap joint were examined analytically. Analysis showed that not all the problems of the lap shear test can be avoided in these tests, but several assumptions in the analysis need to be verified. Three-dimensional micromechanics of textile weaves was continued. While stiffness predictions are well known, the failure mechanisms in these systems are not well understood. The complex 3D problem was bounded to include an enormous number of unknowns, particularly in the interlace regions.

The processing science of composites continues to improve with research to separate the thermal and cure shrinkage components. Embedded strain gages were used to measure the buildup of residual strains during cure. Sensors to measure resin infusion into a composite preform were successfully integrated into the control systems. Equipment to measure permeability of preforms was successfully set up. These data can then be put into the 3D flow model developed. Hardware to implement the sensors and models was also developed.

The synthesis of new high-char yield resins for use as carbon-carbon matrix materials was completed. While much information was learned about the chemistry of these resins, problems with prepregging the resins, toxicity, and the continued uncontrolled exotherms during cure caused the termination of this research. Work continued on making the GC/MS apparatus usable for carbonization studies with the completion of the heat transfer line from

the Cahn microbalance. The stabilization behavior of Conoco bicomponent pitch was investigated; mass loss during the oxygen heat-treatment makes this material difficult to understand. Microscopy support for a carbon-carbon heat-exchanger program identified several problems which were then addressed by the production contractors.

The reliable prepregging of pitch was finally accomplished. Various changes in the process have allowed the incorporation of pitch into fiber bundles which can then be processed into carbon-carbon composites. This is an alternative to the currently used liquid pitch infiltration of carbon preforms. The work on internal stabilizers to prevent bloating in carbon-carbon composites continues with the encapsulated ammonium nitrate and calcium peroxide being the best ones evaluated. Heat-treating the composites before carbonization was found to assist the stabilization process.

The cell structure of net-shaped pitch-based foams was examined; blowing the foam in a mold produced the best net shape. Cell uniformity was good with all the blowing methods, and the cell sizes were dependent on blowing gases and temperatures rather than shaping technique. Examination of the cell structure of foams made with different gases under different conditions showed that larger gas molecules can blow larger cells than smaller gas molecules, and blowing is easier at higher temperatures. Visualization of the foam-blowing model was accomplished with CAD software.

The assessment of carbon-carbon composites for the Air Force identified two critical areas. Carbon-carbon composites can be used for thermal management when thinner plates are required than the currently allowable pyrolytic graphite plates. The degradation effects of lower temperature oxidation on carbon-carbon composites were reviewed.

## **1. CHARACTERIZATION OF FIBERS/MATRIX RESINS AND COMPOSITES**

### **1.1 Composite Mechanical Testing**

A list of composite mechanical testing performed during this reporting period is given in Table 1.

### **1.2 Characterization of Composites and their Constituents**

Following is a list of small projects carried out under this task.

Several TGA and Rheometrics scans were conducted on AS4/3501-6 prepreg to evaluate potential profiles for solvent removal prior to autoclave cure. This work was done in support of the C-17 program.

Tensile tests were performed on medical Teflon tubing intended for blood vessel replacements.

Stress relaxation experiments were conducted on PMR-15 composites in support of GE Aircraft Engines.

The density column was set up for a student working for MLPJ.

A composite laminate was fabricated with various inserts in support of the NDE Branch.

Six composites were fabricated with piezoceramic actuators in support of an AFIT program.

Five composite laminates were fabricated from IM7/5250-4 to be sent to VPI.

#### **1.2.1 RTM Resins for Carbon-Carbon Materials**

The loss of matrix in the carbon composites made at NC A&T was investigated. Composites which had been exposed to 1100°C for many hours were still losing mass on repeated heatings to 1000°C. Since the mass loss in the composite was five percent, which amounts to almost 12 percent in the matrix, this is a significant problem.

**Table 1**  
**COMPOSITE MECHANICAL TESTING FOR THE PERIOD 15 SEP 97 – 14 SEP 98**

Composite	Mechanical Tests					Remarks
	Tension	Compression	Flex	Shear	Other	
IM7/5250-4	124				1	Mode I
IM7/977-3	87					
IM7/Resin (cloth)	6					
AS4/3501-6	43			70	51	CTE, panel cure, deflection, residual stresses
AS4/APC-2	15					
AS4/PR500	4					
AS4C/1995	15		10	10		
APC-2/P4A	7					
AFR700B (neat)	4		58		10	Compact tension
AFR700 (fabric)		35				
XN70/RS3					6	CTE, thermocycling
Neat Resin	5		15		64	Compact tension, E-beam cure
1080 Fiberglass	10					
2116 Fiberglass	10					
7628 Fiberglass	10					
Glass (fabric)		15				
Polyester	10					
Glass Epoxy	18		65		3	CTE
FM300 (adhesive)					1	CTE
FM300-2U (neat)	3					
Hysol (adhesive)	9				1	CTE
Magnolia (adhesive)	9				1	CTE

**Table 1 (Concluded)**  
**COMPOSITE MECHANICAL TESTING FOR THE PERIOD 15 SEP 97 – 14 SEP 98**

Composite	Mechanical Tests					Remarks
	Tension	Compression	Flex	Shear	Other	
EA9396 Epoxy	5				1	CTE
CFRP Rod	9		14			
Laser-Cured Resin					9	Compact tension
T300/LTM45	52				5	Mode II
828/D230	17		9			Model
828/D230 Single Fiber	22					
828/D230 Glass Fiber	21					
828/D230 Polyester			33		2	Aluminum beam flex
828/D230 SCS	16					Model
828/D230 Aluminum Rod	24					
Aluminum/Adhesive					30	Mode I, Mode II
Aluminum/Resin/Fiber					8	Mode II
Aluminum	1					
Kevlar/3501-6	4				2	CTE
Teflon	2					
Vascular Graft	7				3	Torsion
Carbon/Carbon			4			
Graphite Foam	30				6	Torsion
Liquid Crystal RM82T5					8	Compact tension (neat)
Steel (Rebar)	4					
Concrete (cubes)					2	CTE
Composite Rod/Concrete			6			Beam
Composite Rod/Concrete/Hysol				35		Push-out
T650/AFR700B					12	Compact Tension

FTIR analysis did not reveal any significant changes in the material between carbonization and subsequent heating to 1000°C. EDS analysis of these composites showed a substantial amount of sodium and oxygen on the surface; sodium hydroxide was considered the most likely source of this contamination. This problem was similar to one found in early PAN-based fibers which required a heat treatment to 1300°C before repeated weight losses were eliminated. Increasing the initial carbonization temperature to 1300°C has apparently solved the problem.

#### 1.2.2 Ad Hoc Programming for the Analysis of RDS Data

The Excel program that was used to analyze RDS (dynamic mechanical spectra) data was found not to satisfactorily handle the current data. This program assumed gently sloping monotonically decreasing data which was acceptable for finding frequency shifts of earlier storage modulus data. Since the loss modulus usually has a peak in the data, a new method of finding the correct frequency shifts for the data was needed. Figure 1 shows an example of the shifted RDS data. The storage modulus,  $G'$ , was shifted satisfactorily relative to 0°C. In this example the loss modulus,  $G''$ , was shifted using the  $G'$  shift factors which was not as satisfactory as the  $G'$  shifting.

A straight-line fit was used in the regions of small increases in the data similar to the previous program. A third-order polynomial was fit to the loss modulus data near the peak. This allows shifting even if the data from different temperatures didn't overlap. Visual identification of the location of the peak is needed, but this was not considered a serious problem. Vertical shifting of the data was incorporated to account for changes in the sample when the heating cycle passed from liquid nitrogen temperatures through ambient. An example of RDS data shifted according to their own shift factors is shown in Figure 2.



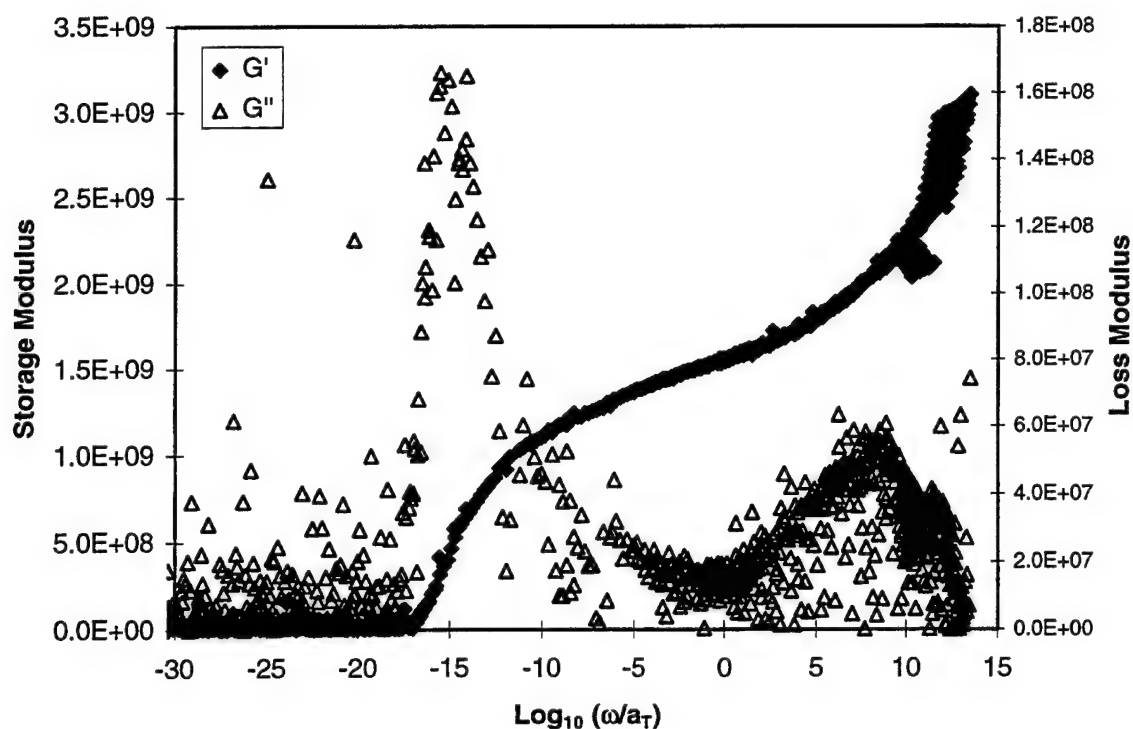


**Figure 1. RDS Data for the EJ410b34m2 Nanocomposite Sample showing the Shifted Data Relative to 0°C with the Loss Modulus Shifted using the Storage Modulus Shift Factors.**

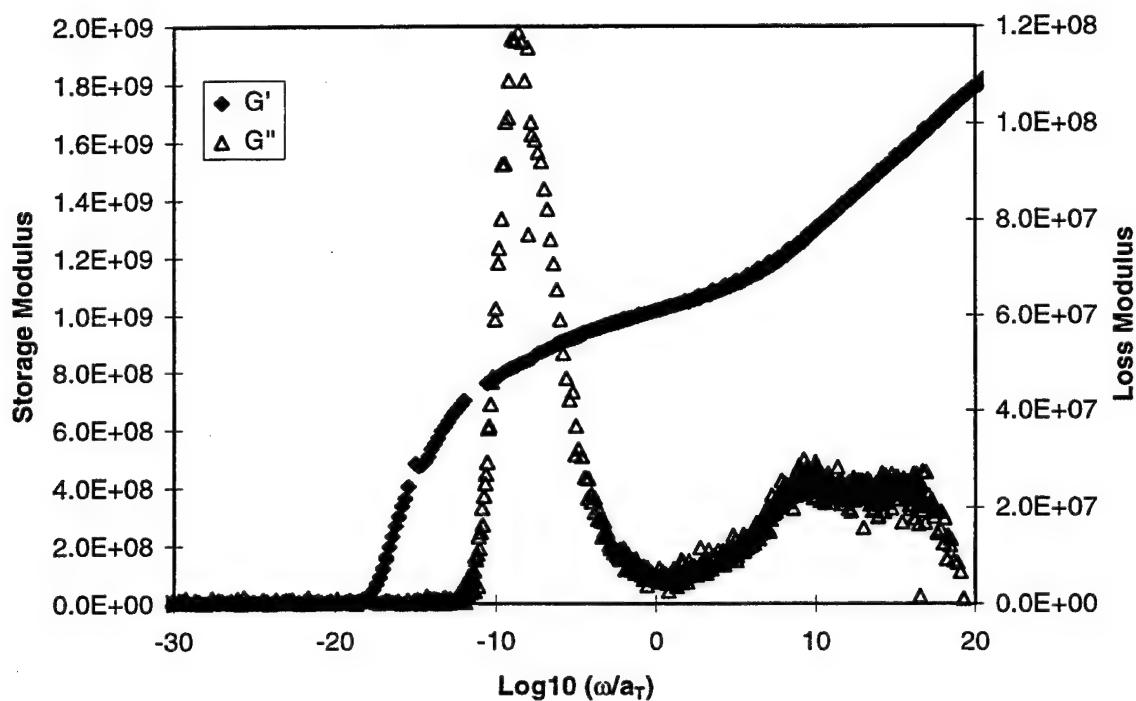


**Figure 2. RDS Data for the EJ40000 Nanocomposite Sample showing the Shifted Young's Modulus Data Relative to 0°C.**

The shift factors are frequency multipliers or additives to the  $\log_e$  of the frequency used to adjust the data to a specific temperature. This is done because the experimentally-accessible frequencies are limited to only a few orders of magnitude, and the principles of time-temperature superposition allow the results from one temperature and frequency to show the results at another temperature and frequency. The master curve produced represents the results which would be obtained if the results could be obtained at the reference temperature over a much larger frequency range. The reference temperature was taken as 0°C; lower temperature data is shifted up representing a shorter response time (right of 0 above) and higher temperature data is shifted down (left of 0 above). Shifting to temperatures beyond those of major transitions is not valid; note that the data significantly above the G'' peak are all essentially zero.

A second problem discovered while adjusting the shifting program was that some of the data at lower temperatures showed a significant split. This is seen in Figure 1 but is more clearly seen in the close-up detail of that plot shown in Figure 3. The reason for these data anomalies was never identified.

### **1.3 Lifetime Prediction of Composite Performance**

Modulated DSC was shown to be an effective technique to detect the glass transition temperature of as-cured AFR700B. The most pronounced T<sub>g</sub> transition was measured using operation conditions of  $\pm 2^\circ\text{C}$  at a period of 60 seconds and a heating rate of  $5^\circ\text{C}/\text{minute}$ .

A study was conducted to determine the equivalency of degradation for specimens degraded at different temperatures in saturated steam. Specimens were exposed for different times at 120, 140, 160, and  $180^\circ\text{C}$  in an attempt to achieve the same level of

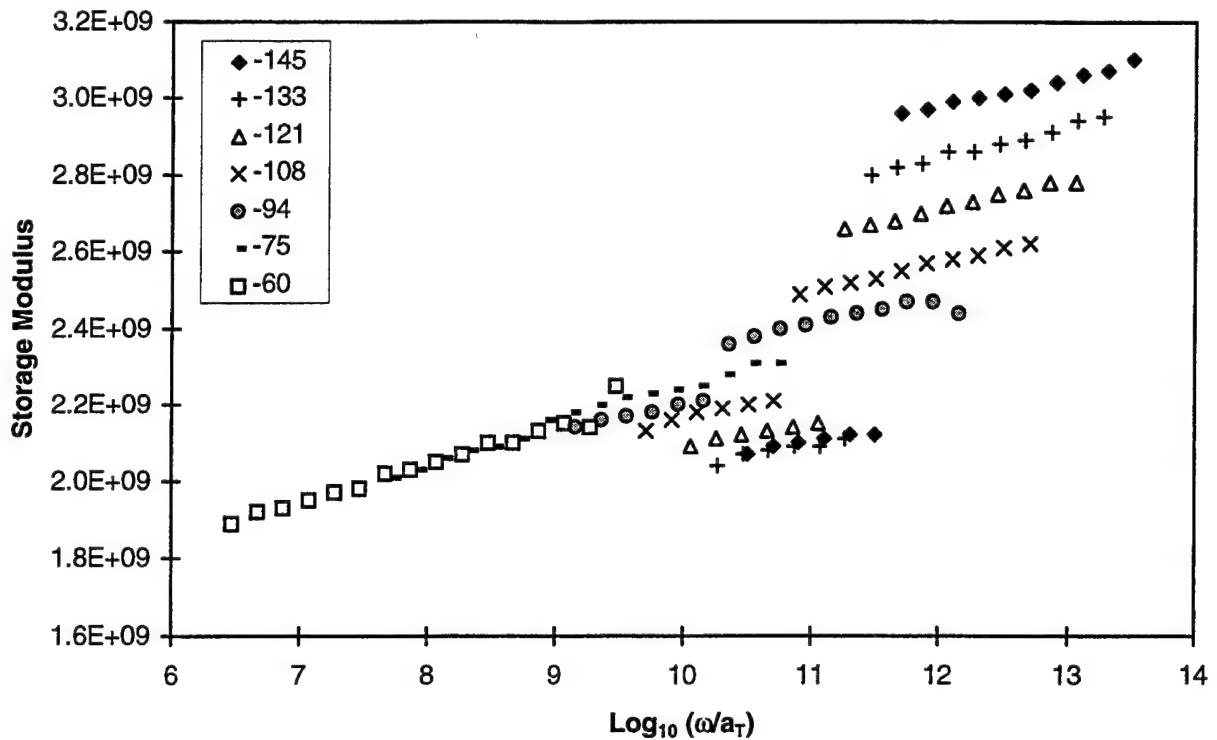


**Figure 3. Selected RDS Storage Modulus Data for the EJ410b34m2 Nanocomposite Sample showing Anomalous Data at Lower Temperatures (Shifted Relative to 0°C).**

degradation for each specimen. The data suggested that the degradation processes may change with temperature and saturation conditions. The conditions (temperature and humidity) used to saturate the specimens prior to exposure affected the results. Specimens saturated under mild conditions experienced a permanent weight gain after bomb exposure, while specimens exposed to harsher conditions experienced a permanent weight loss.

Work was conducted to establish standard test conditions for hygrothermal degradation using the pipe bomb. Placement of a thermocouple in a pipe bomb suggested that it takes approximately two hours for the interior of the bomb to reach temperature during a 150-200°C exposure. Using a water quench of the bomb, the specimen returned to approximately room temperature in less than two minutes. These results suggest that kinetics of degradation cannot be determined accurately from short time exposure data.

An experimental plan was established to understand the variations in  $T_g$  throughout the lateral dimensions of an AFR700B panel. The results showed the  $T_g$  was relatively constant throughout the panel, with the exception of regions extremely close to the specimen edge. This is not surprising, since the edges of the specimen are typically altered in appearance from the center regions, suggesting less compaction and resultant chemical variation.

A literature search was conducted to identify characteristic peaks which can be correlated to degradation and cure processes. A variety of model compounds were selected to study the effect of chemical structure on hydrolytic stability of norbornene-terminated addition polyimides.

#### **1.4 Rehabilitation of Concrete Bridge Beams with Fiber-Reinforced Composites**

Over the last two years appropriate composite and adhesive M&P has been developed in the lab [1] and implemented in the rehabilitation of a concrete box-beam bridge in the field [2]. In the latter study, composite plates were bonded to the lower face of 8.5 m concrete beams in a bridge deck, across the entire span, with an ambient-cure epoxy adhesive. Doubler joints were introduced at four locations along the beam's length to connect the composite plates. Flexural tests showed a significant increase in maximum bending moment of such an externally-reinforced beam compared to a beam without composite reinforcement. There are, however, a number of disadvantages to employing composite *plate* reinforcement for the rehabilitation of concrete bridge beams:

- Plates have to be fabricated in sizes that are practical and convenient to transport to the field site, necessitating the development of efficient composite joining techniques for beams with long spans.

- Plate reinforcement typically covers the entire lower surface of the rehabilitated beam, restricting the drainage of absorbed water in the concrete; accumulation of this water at the bondline accelerates its degradation.
- Optimum bonding requires careful and consistent surface preparation of the plate and application of pressure during adhesive cure, to promote intimate contact between adhesive and adherends and minimize voids.
- Free-edge, thermal and residual stresses, in conjunction with the service environment, can promote plate debonding and consequent loss of reinforcing capability over time.

Some of these disadvantages can be overcome by using composite rods (of the same cross-sectional area as the plate) embedded in parallel, longitudinal grooves cut into the tensile face of the beam. Continuous lengths of pultruded rods can be transported to the field in rolls and cut to the necessary length, thereby avoiding composite joints. Since the rods cover a small fraction of the beam's lower surface, drainage of absorbed water is not hindered. The ratio of composite bonded surface to volume is substantially lower than for a plate; this, coupled with the fact that the rods are completely embedded in the adhesive makes them less susceptible to interfacial degradation in service. Pultruded rods are also less expensive to fabricate than precured composite plates and easier to employ in the field, requiring no applied pressure during adhesive cure. This rehabilitation concept was investigated with virgin 2.6-m beams in the lab and scaled up to 8.5-m beams identical to those employed in replacement bridge decks [3]. In this approach pultruded continuous composite rods were embedded in longitudinal grooves machined into a beam's lower face using an ambient-cure epoxy adhesive. The success of this approach is evident from the plot

shown in Figure 4, where the maximum bending moment is compared with those of a baseline beam (without composite reinforcement) and a beam with composite plate reinforcement (of equivalent cross-sectional area as the composite rods). In the case of deteriorated beams, however, weak concrete surrounding the embedded composite rods can fail cohesively when the beam is loaded in flexure, preventing the rods from imparting improved strength and stiffness. To avoid premature failure in the weak concrete, the longitudinal grooves may be machined to greater depths, up to where the concrete has not been degraded. This modified approach, with grooves of extended depth, was initially attempted on 2.6-m virgin beams in the lab. It was then scaled up to 10.4-m deteriorated beams removed from the Smith Road bridge in Butler County, OH.

In this work unidirectional pultruded T-300/vinyl ester rods from DFI Pultruded Composites, Inc., were used as the reinforcement. The adhesive used was a two-part epoxy (EA9460 from Dexter Hysol, Inc.) which cures under ambient conditions. Rectangular grooves were machined into the tensile faces of these beams with a portable masonry power cutter. Composite rods, the length of the beam, were sanded, wiped clean with acetone, and embedded in the epoxy within the grooves. The adhesive was then allowed to cure overnight under ambient conditions. The beams were tested in four-point flexure in accordance with ASTM C78-84, as described in earlier reports [1-3].

Initially, 2.6-m steel-reinforced concrete beams cast for earlier studies were employed to optimize the composite reinforcement and validate analytical predictions of beam behavior under flexural loading. The variables in these studies were the composite/steel reinforcement ratio and the depth to which composite rods were embedded in the tensile surface of the beam. Based on the results from these tests and the dimensions and constituent properties of

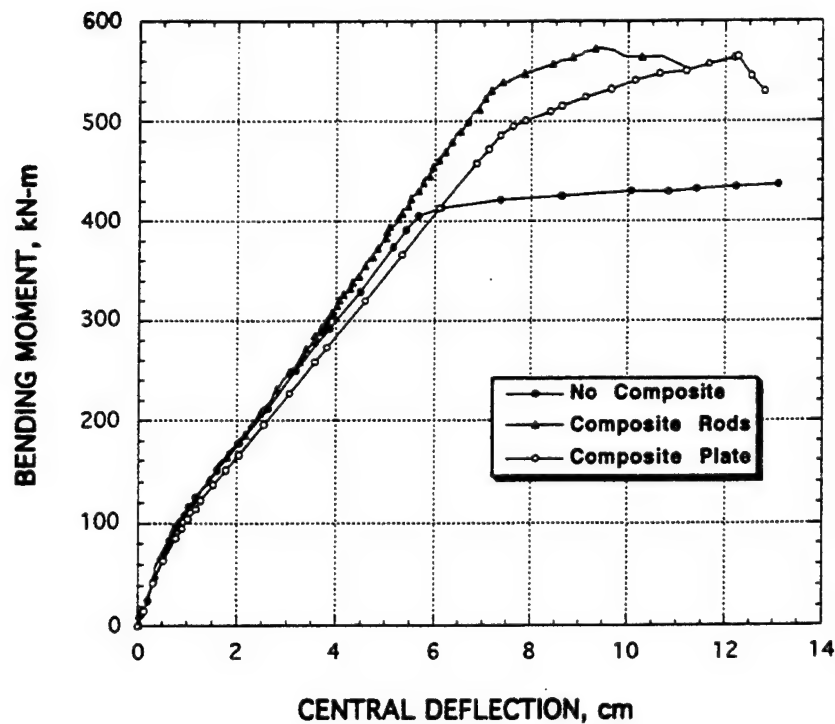


**Figure 4. Comparison of Maximum Bending Moments of 8.5-m Concrete Beams without External Reinforcement, with Composite Plate Reinforcement and with Composite Rod Reinforcement, vs. Measured Central Deflections.**

the deteriorated 10.4-m beams from the Smith Road bridge, the rehabilitation scheme was designed for these full-size beams. The original bridge deck appeared to be cast integrally with the beams; consequently, the beams had to be sectioned out at the site and were received for testing with a section of the concrete deck attached. Three beams were received in all, deteriorated to different extents. One beam was tested as received, while the remaining two were reinforced with composite rods in the tensile surface, embedded in grooves machined down to where the concrete did not appear to be degraded. Different composite/steel ratios were employed for these two rehabilitated beams. Since all beams were deteriorated or damaged to different extents, none of them could serve as an adequate baseline for comparison with a beam rehabilitated with composite rods. Consequently, the flexural

response of the second and third bridge beams was characterized prior to their reinforcement with composite rods; this response served as the baseline for comparison to the flexural response of the beams after reinforcement with composites.

The flexural response of all three beams is shown in Figures 5-7 as plots of maximum bending moment vs. central deflection. The as-received beam (Figure 5) displays a knee in the plot early in the load application; based on the low load level at which the knee is seen and the fact that it is reversible (as seen from two consecutive loadings), the knee does not result from steel yielding. Past this knee, the plot continues almost linearly to ultimate failure of the beam (via compression fracture of the concrete) with no evidence of steel yielding, which is highly unusual. Figure 6 shows the response for a rehabilitated beam with a composite/steel ratio of 0.25, before and after composite rod reinforcement. Ultimate failure occurred via fracture of the concrete on the compression face followed by concrete failure in the tensile face, in the region surrounding the composite rods. From a comparison of the preloading and the loading curves to failure, the flexural stiffening provided by the composite reinforcement is apparent. Throughout this failure process the concrete/adhesive/composite bond, for the most part, remained intact. The plots in Figure 7 are similar to those in Figure 6, but with the composite/steel ratio increased to 0.3. Ultimate failure in this case was precipitated by tensile fracture of a steel rebar, which is unusual. Tests on both beams externally reinforced with composite rods adequately demonstrate the viability of this rehabilitation concept with deteriorated beams.



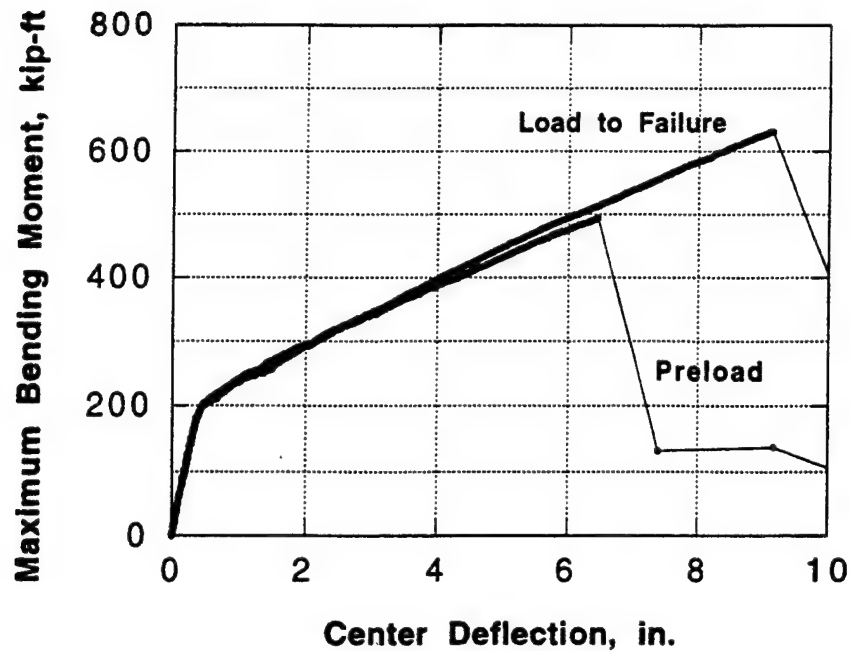


Figure 5. Comparison of Maximum Bending Moments of a Deteriorated 10.4-m Concrete Beam without External Reinforcement, vs. Measured Central Deflections.

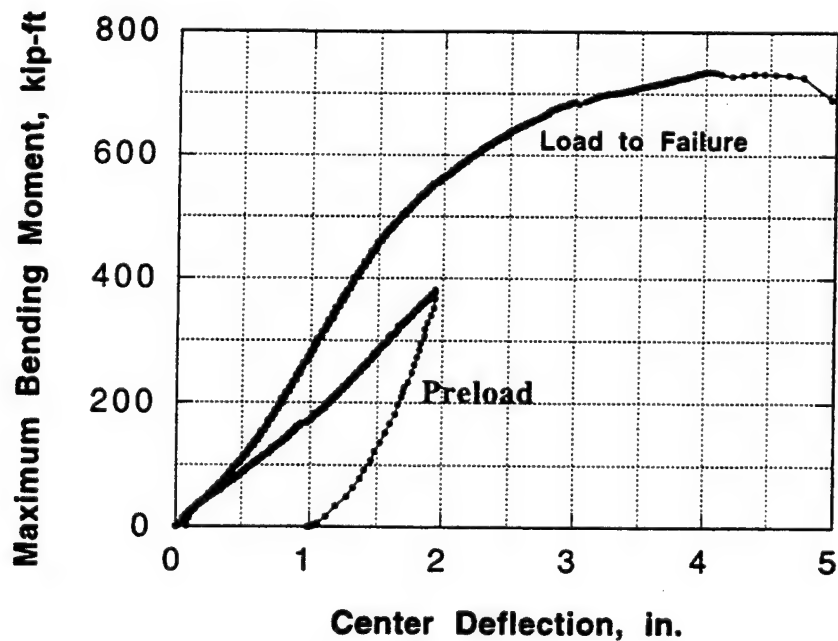


Figure 6. Comparison of Maximum Bending Moments of a Deteriorated 10.4-m Concrete Beam Externally Reinforced with Four Rods 0.625" in Diameter, vs. Measured Central Deflections.

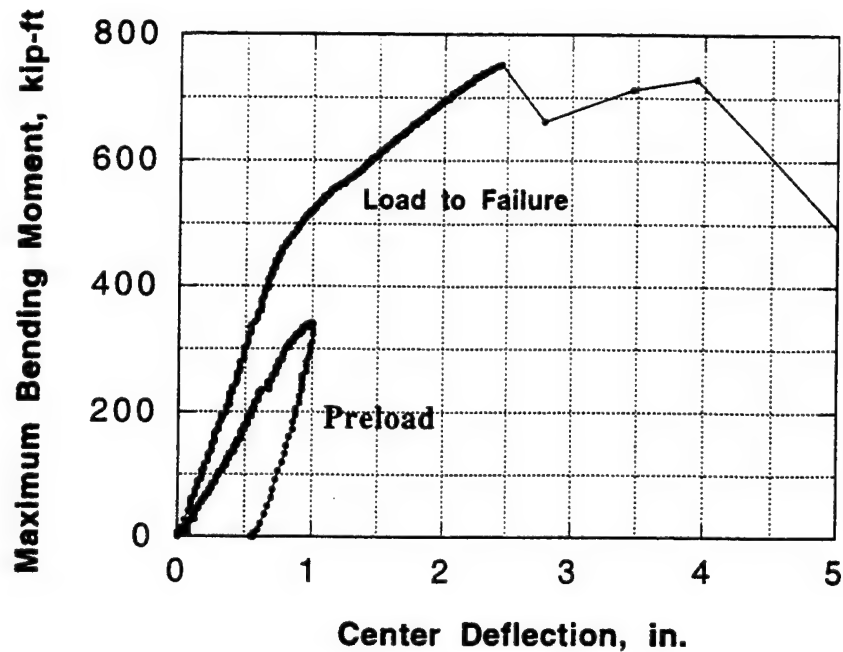


Figure 7. Comparison of Maximum Bending Moments of a Deteriorated 10.4-m concrete Beam Externally Reinforced with Four Rods, Two of 0.625" Diameter and Two 0.75" Diameter, vs. Measured Central Deflections.

## 2. MECHANICS OF POLYMER-MATRIX COMPOSITES

### 2.1 Damage Development for Composite Laminates with Center Holes

The occurrence of holes in load-bearing composite structures is pervasive in the aerospace industry as a result of the use of mechanical fasteners in the assembly and use of cutouts to accommodate wiring and hydraulic lines. The design of laminates with holes or with fasteners in composite structures is largely based on experimental test data [4]. The most widely utilized analysis methods are those based on the two-dimensional elasticity solution provided by Lekhnitskii [5] for an infinite orthotropic plate with an open hole. Although the aforementioned analyses are useful design tools, a more rigorous stress analysis

method and failure criterion is needed to predict the strength of laminates with holes and with fasteners.

Recently, Larve [6,7] developed a three-dimensional stress analysis method for a composite laminate with an open hole or an elastic inclusion. This method is based on the spline variational theory and was verified through comparisons of in-plane and interlaminar stresses with results obtained from an asymptotic solution. An experimental program was initiated on the damage initiation and its progression in composite laminates with open and filled holes. The main objective of this program is to validate the spline variational elastic laminate theory (SVELT) and to assess the damage evolution for development of a suitable failure prediction theory. The two laminate groups considered are: basic laminates,  $[0_8]_T$ ,  $[90_8]_T$ , and  $[\pm 45]_{2S}$ , and multidirectional laminates,  $[\pm 30/90_2]_S$ ,  $[0_2/90_2]_S$ ,  $[0/90]_{2S}$ ,  $[45/0/-45/90]_S$ , and  $[\pm 45/90/0]_S$ . Hole size effect on the damage initiation and final failure is being investigated by employing five different hole diameters: 0.125, 0.25, 0.5, 0.75, and 1.0 inch.

Monotonic and incremental experiments were conducted to observe the initiation and growth of damage and to record changes in the strain field. For each loading increment axial strain was recorded in close proximity to the hole, and the specimen was x-rayed. Acoustic emission data were collected during loading and compared to strain measurements and radiographic images to identify significant damage events. Additional analysis was conducted by comparing experimental strain data to results obtained from the spline variational theory.

### 2.1.1 Experiment

The material system chosen was graphite/toughened epoxy, IM7/5250-4. Composite panels were fabricated in an autoclave according to the manufacturer's cure cycle and subjected to postcure at 440°F for four hours. All cured panels were examined by ultrasonic C-scan to insure the quality of the panel. The fiber volume was determined using the acid digestion method. Straight-sided specimens were cut from the panels using a diamond-impregnated saw with water cooling. The specimen width was three inches for a hole diameter equal to or greater than 0.5 inch and 1.5 inches for a hole diameter less than 0.5 inch, and 1.0 inch for coupons. A milling machine was used to drill holes using diamond-impregnated core drill bits. The drill speed and pressure were previously established to produce a damage-free hole. Hole edge regions are inspected prior to test by x-radiography to examine any damage induced due to drilling.

Specimens were tested under incremental loading and monotonic loading for a damage evolution study. The strain on or near the vicinity of the hole edge is measured using miniature strain gages of 0.008 inch (on the hole edge) and 0.032 inch in gage length. Figure 8 shows the strain gage locations. The damage initiation and progression of damage in the vicinity of the hole was observed using x-radiography after each incremental loading. Acoustic emission was also incorporated to determine the onset of matrix cracking. The location, magnitude, and load corresponding to the occurrence of transverse cracks, longitudinal cracks, and delamination were recorded. For coupon specimens the stress at the onset of damage initiation and ultimate strength was also determined to compare with the hole specimen results. Specimens for two quasi-isotropic laminates,  $[45/0/-45/90]_s$  and  $[\pm 45/90/0]_s$ , and filled-hole compression were prepared for testing.

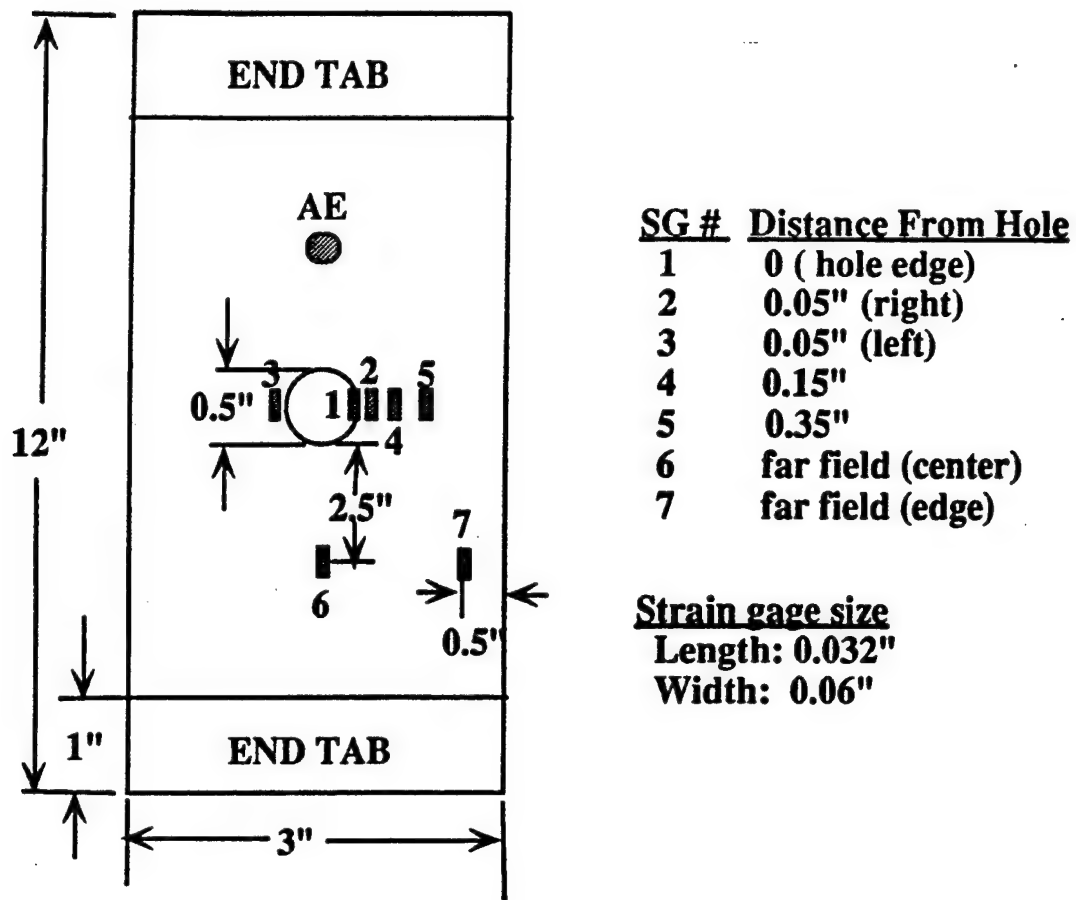


Figure 8. Specimen Dimensions and Strain Gage Locations.

### 2.1.2 Results

Some of the results for open-hole tension are presented in this report. All strains were recorded during each incremental loading and then x-radiographs were taken. Incremental loadings consisted of 2-30 increments dependent upon the type of laminates and test objective. In this report selected stress-strain curves and x-radiographs will be included, and the other data are available by request.

The stress-strain curves are shown in Figures 9-14. The stress-strain relation is initially linear and becomes nonlinear as the applied stress increases for all cases except  $[0]_{8T}$  and  $[90]_{8T}$  laminates. The proportional limit varies as a function of the distance

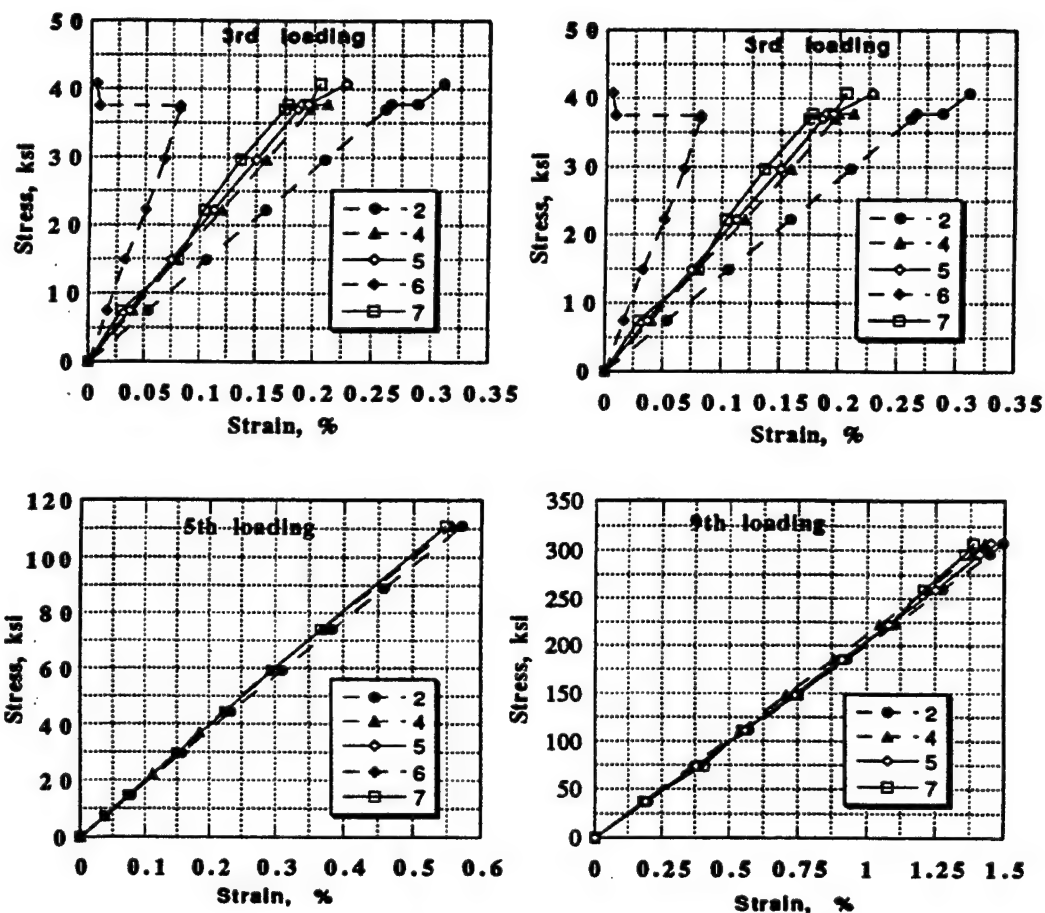


Figure 9. Stress-Strain Curves for  $[0]_{BT}$ .

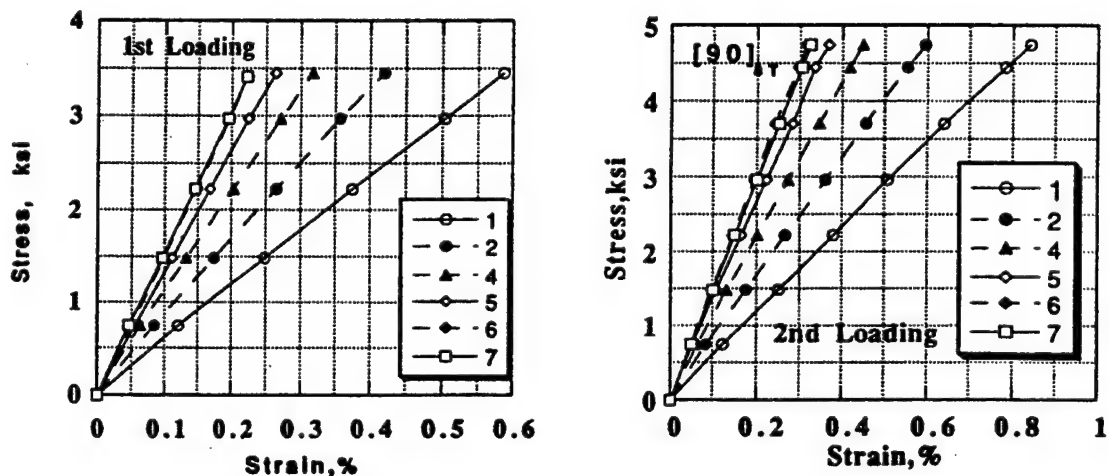


Figure 10. Stress-Strain Curves for  $[90]_{BT}$ .

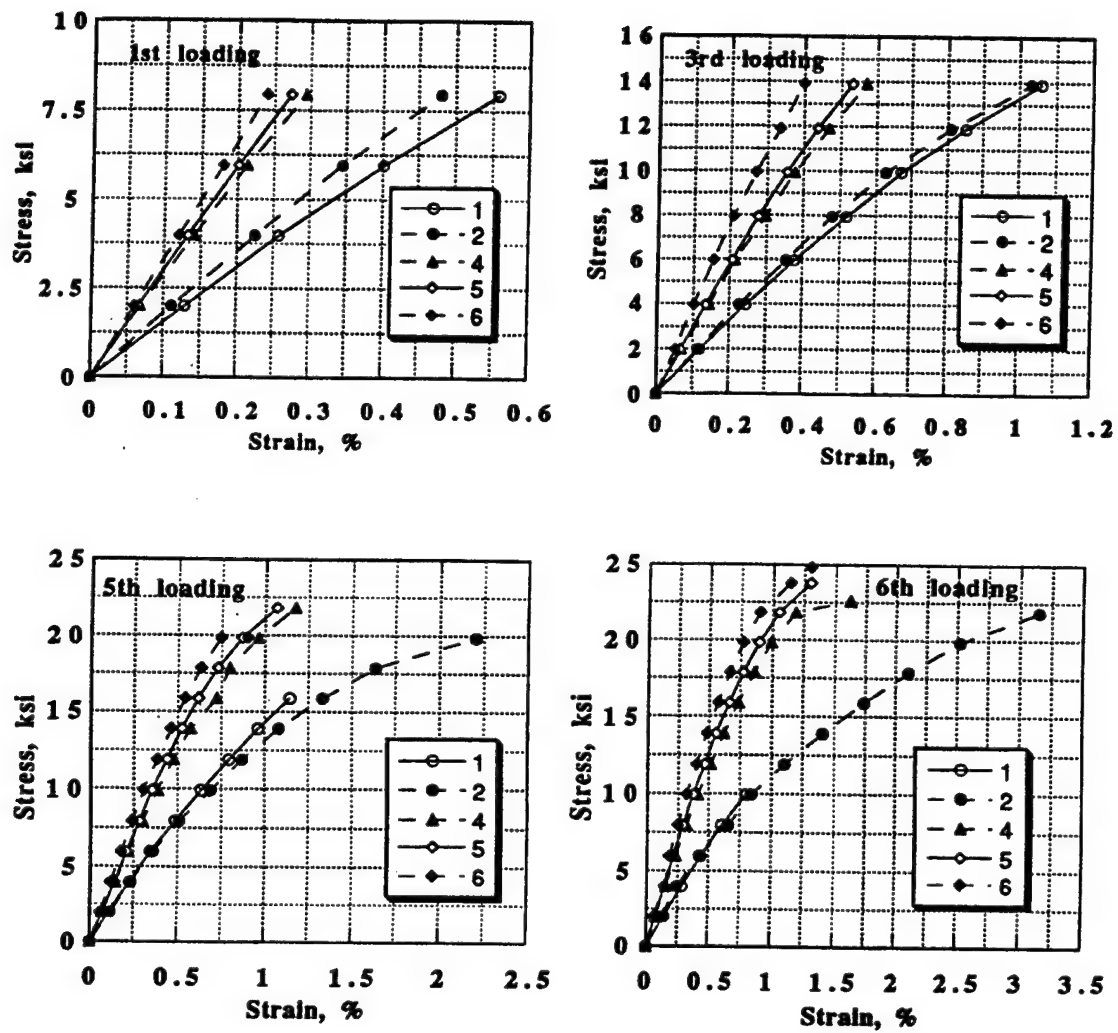


Figure 11. Stress-Strain Curves for  $[\pm 45]_{25}$ .

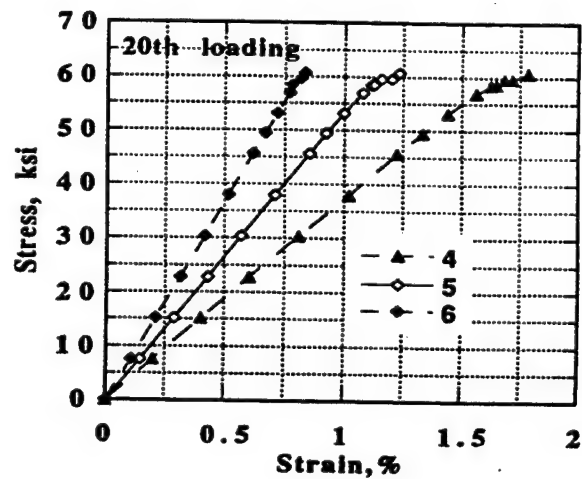
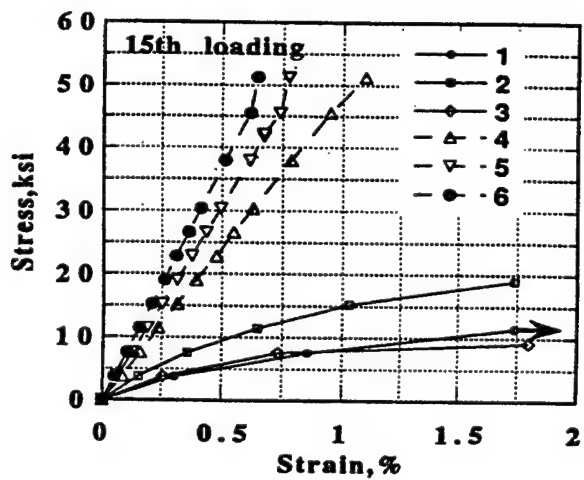
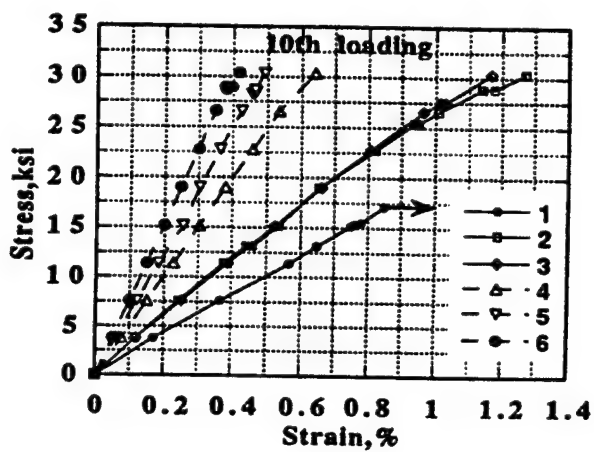
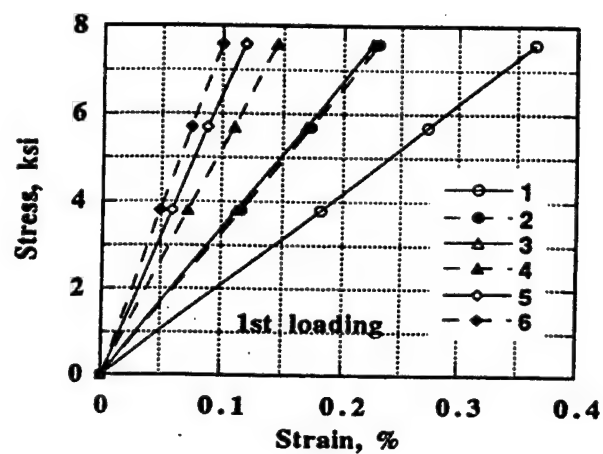


Figure 12. Stress-Strain Curves for  $[\pm 30/90]_s$ .



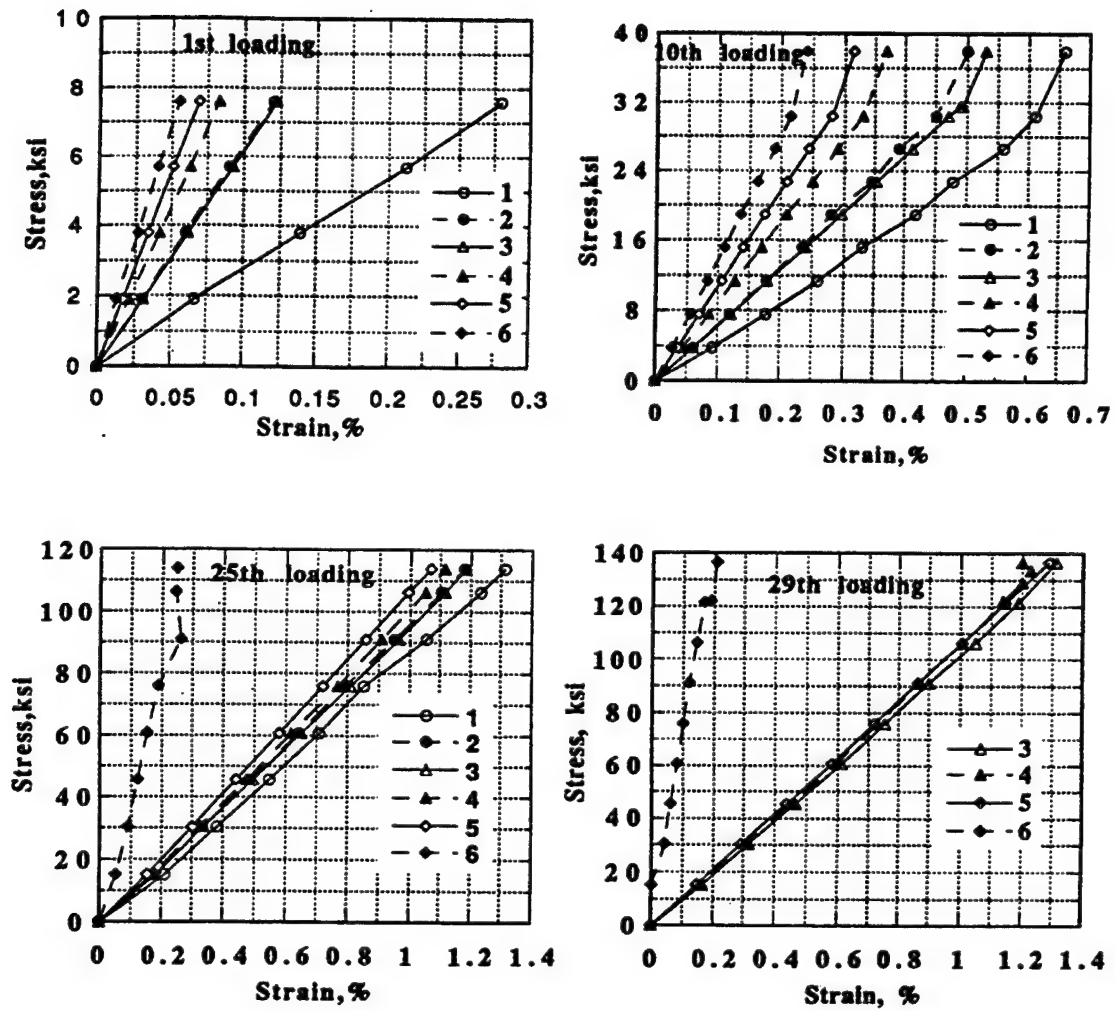


Figure 13. Stress-Strain Curves for  $[0_2/90_2]_S$ .

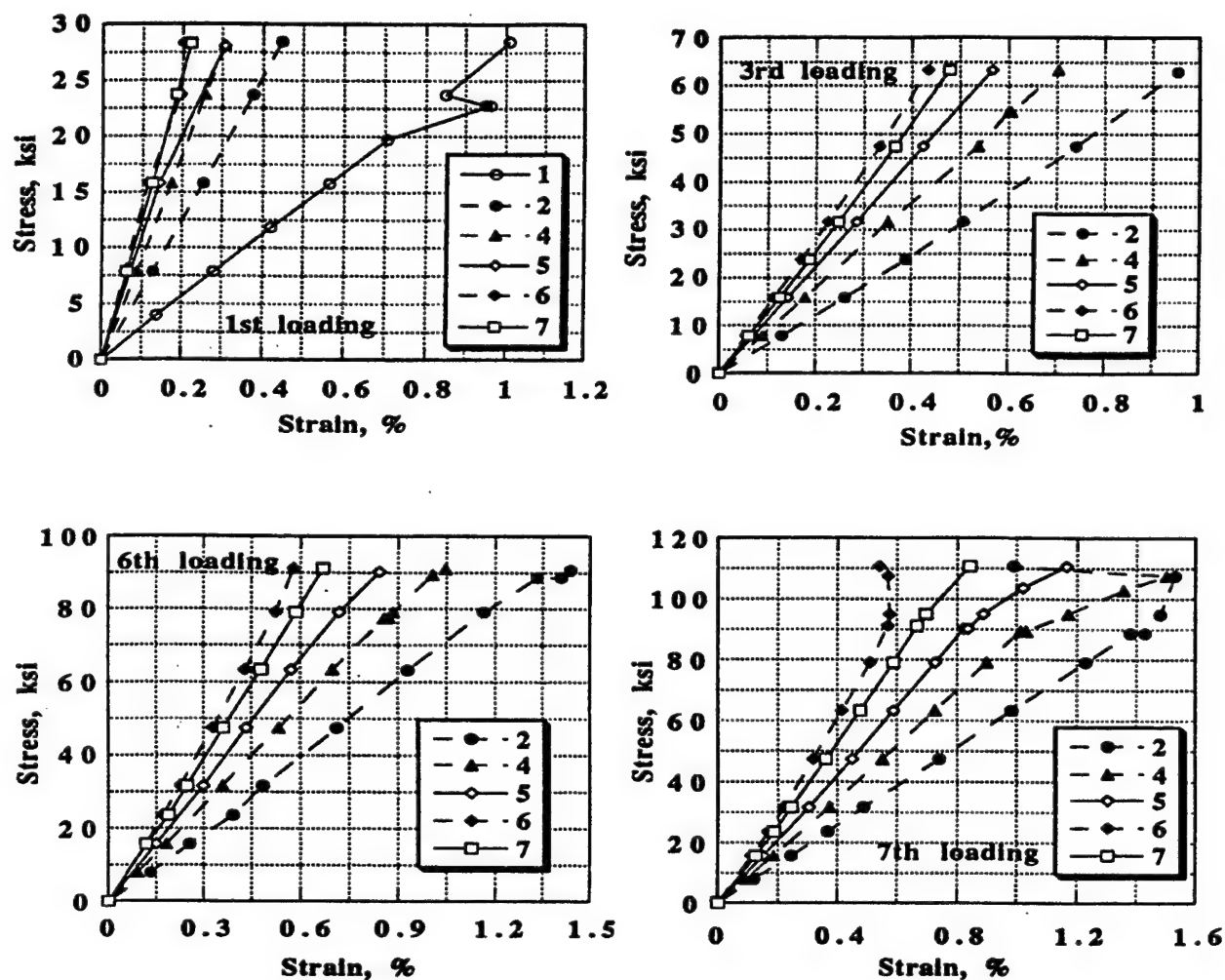


Figure 14. Stress-Strain Curves for  $[0/90]_{2S}$ .

from the hole edge. The stress-strain curves demonstrate the damage initiation and its growth to a certain extent. The initial strain concentration factor (the ratio of the hole edge strain to far-field strain) decreases as the damage growth for all laminates except for  $[90]_{8T}$ . For  $[0]_{8T}$  and  $[0_2/90_2]$  laminates, the strains in the proximity of the hole appear to approach the far-field strain. This indicates that the strain concentration around the hole appears to ease as the damage reaches a certain stage. However the stress-strain behavior of two incremental loadings for the  $[90]_{8T}$  laminate are identical to each other, which implies no damage

occurred until final failure. Figures 15-19 show damage obtained by x-radiographs. Longitudinal cracks in the  $[0]_{8T}$  emanated from the hole edge and propagated along the fiber at subsequent incremental loadings. The SVELT analysis indicated that the shear stress appears to be responsible for the longitudinal crack. The  $[90]_{8T}$  specimens failed without exhibiting any damage prior to final failure, and show net tension failure along the ligament between the hole and straight free edge. For the  $[\pm 45]_S$  laminate, cracks occurred at the hole edge and propagated along the fiber direction ( $45^\circ$ ) and reached the free edge before final failure. For the  $[\pm 0/90_2]_S$  laminate, the damage initiated at the hole edge in the form of a transverse crack in the  $90^\circ$  layer, and further matrix cracks occurred along the fiber direction in the  $\pm 30^\circ$  layer as stress increased. Thereafter, extensive delamination occurred around the hole edge as well as the straight edge as shown in Figure 17. Transverse cracks in the  $90^\circ$  layer and longitudinal cracks in the  $0^\circ$  layer appear to occur simultaneously in the  $[0_2/90_2]_S$  and  $[0/90]_{2S}$  laminates. The longitudinal cracks reached the end tab in the  $[0_2/90_2]_S$  laminate, whereas the cracks terminated prior to reaching the end in the  $[0/90]_{2S}$  laminate. An extensive delamination occurred along the longitudinal cracks as shown in Figures 18 and 19. Ply dispersion in laminates reduces the damage growth remarkably, but strain concentration to a lesser degree compared with the undispersed ply group. Table 2 presents a summary of the test results.

The damage initiation stress is affected by strain concentration factors, where no damage initiation occurs. As damage develops, effective stress concentration decreases, and net ligament stress at failure approaches the static strength of the unnotched coupon for  $[0]_{8T}$ ,  $[\pm 45]_{2S}$ ,  $[\pm 30/90_2]_S$ , and  $[0_2/90_2]_S$  lay-ups, but not for  $[90]_{8T}$  and  $[0/90]_{2S}$

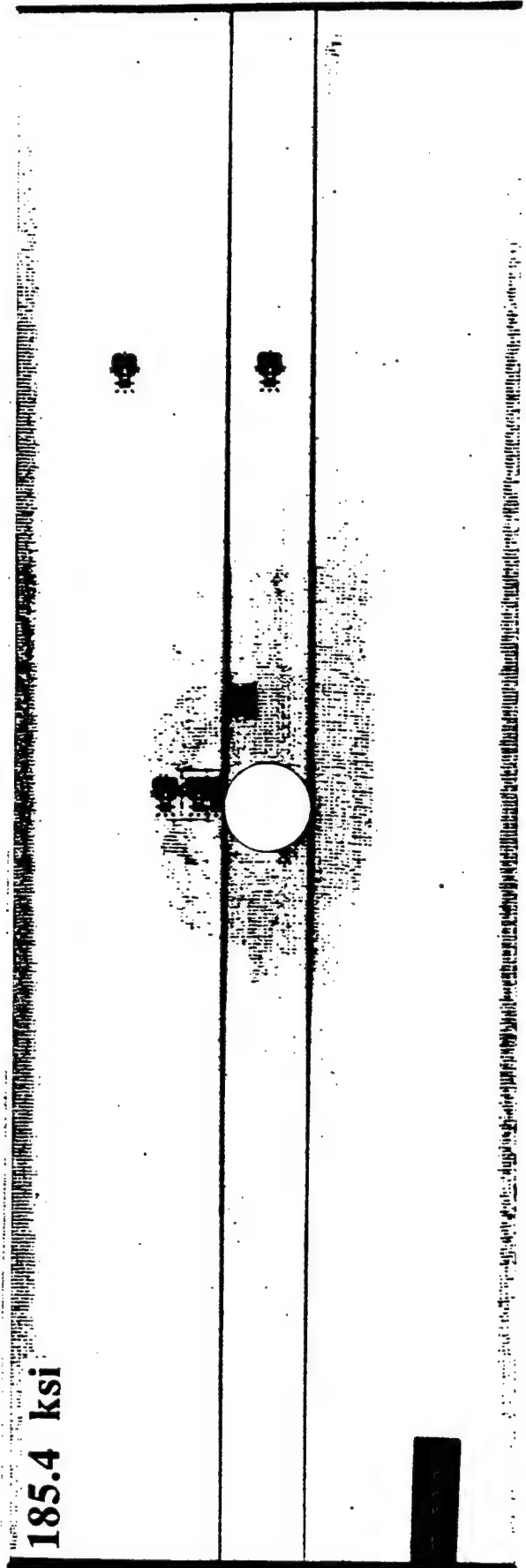
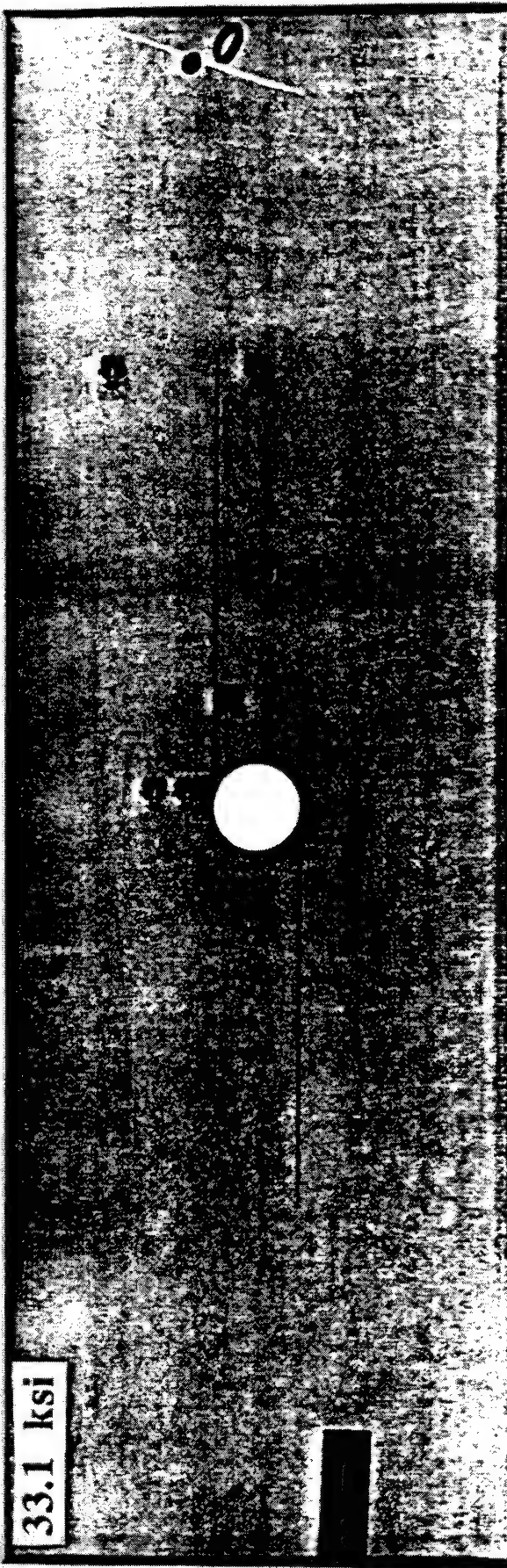


Figure 15. Radiographs of Damage:  $[0]_{67}$

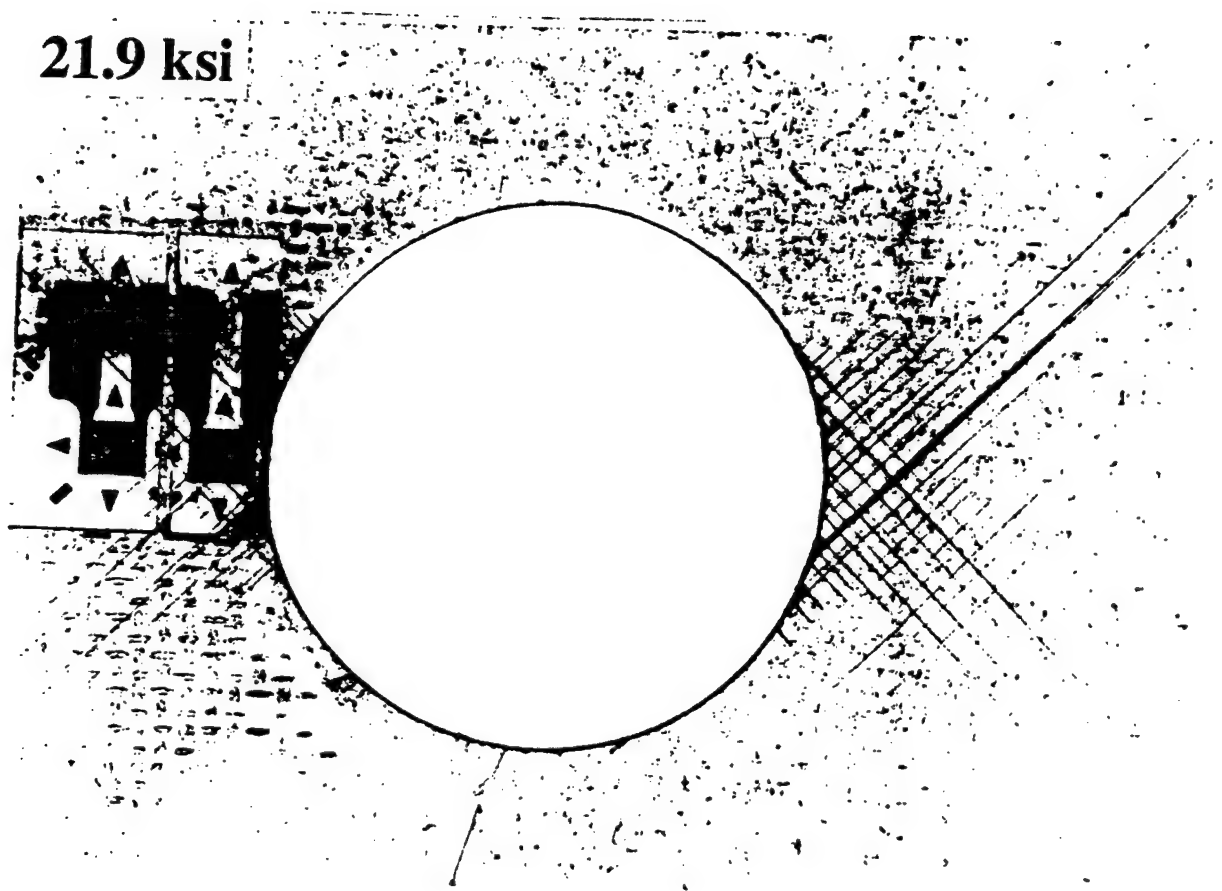


Figure 16. Radiograph of Damage:  $[\pm 45]_{2S}$ .

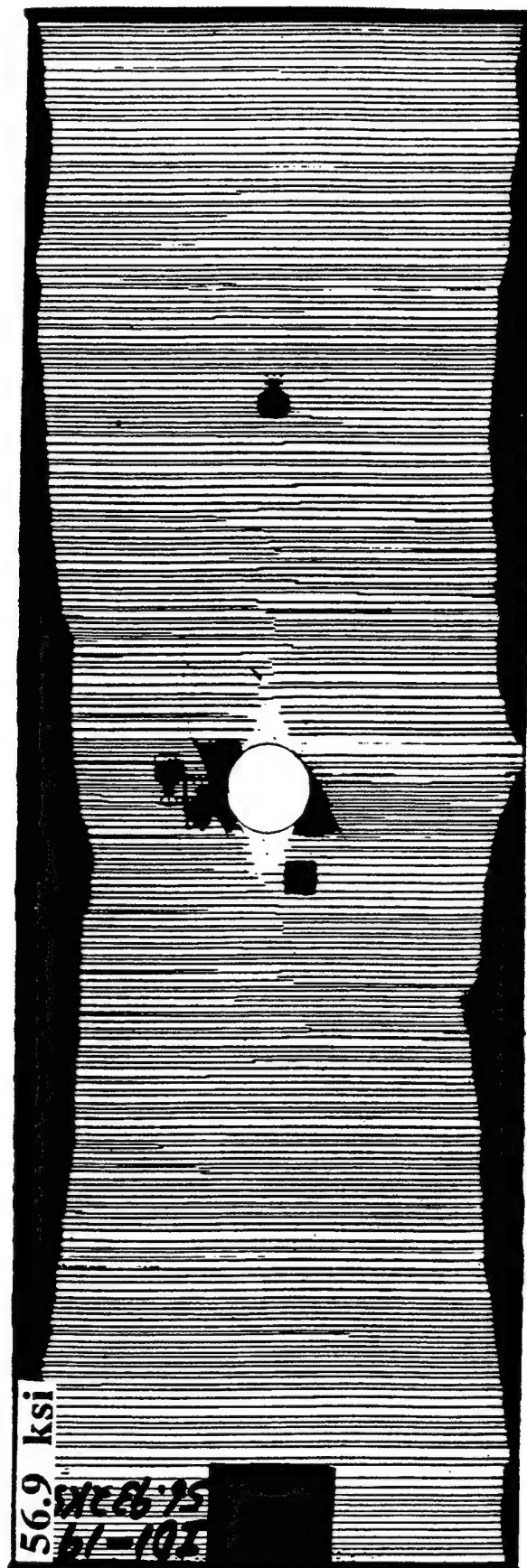
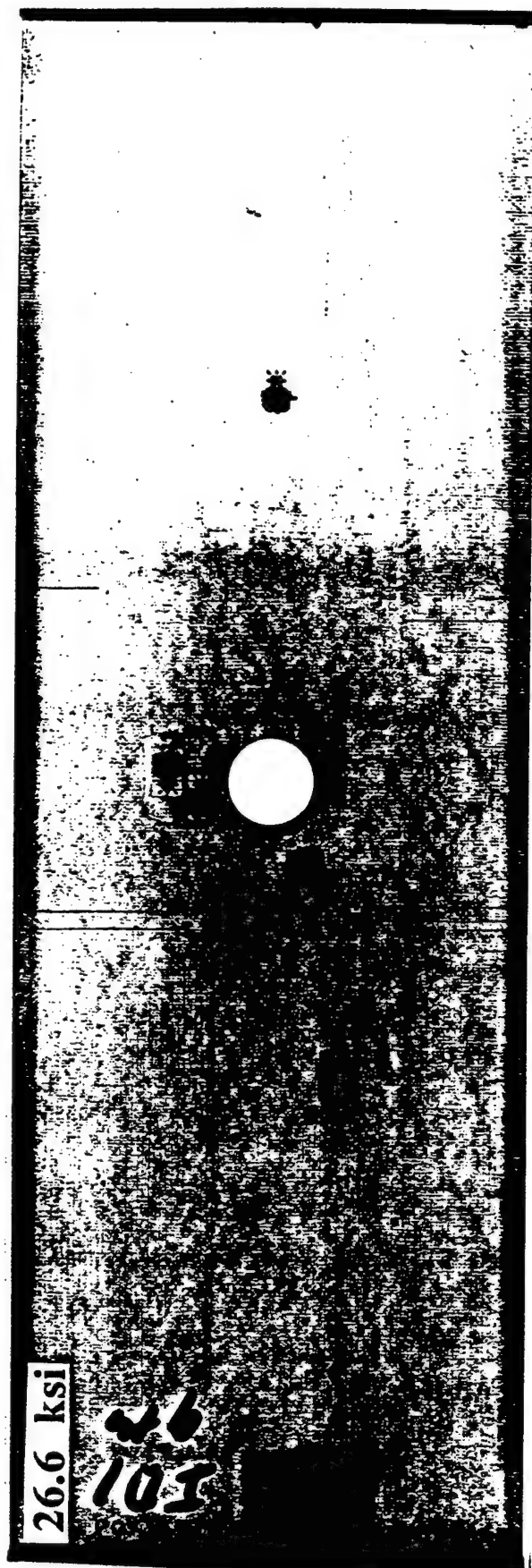


Figure 17. Radiographs of Damage:  $[\pm 30/90]_{2s}$ .



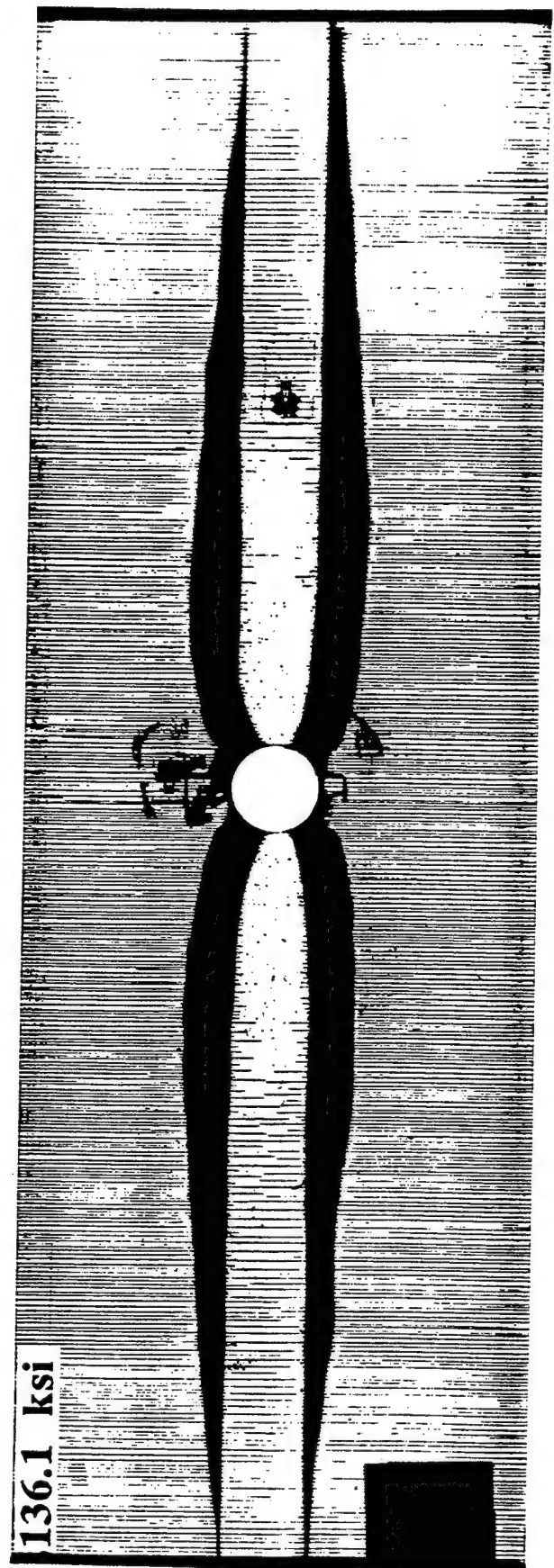
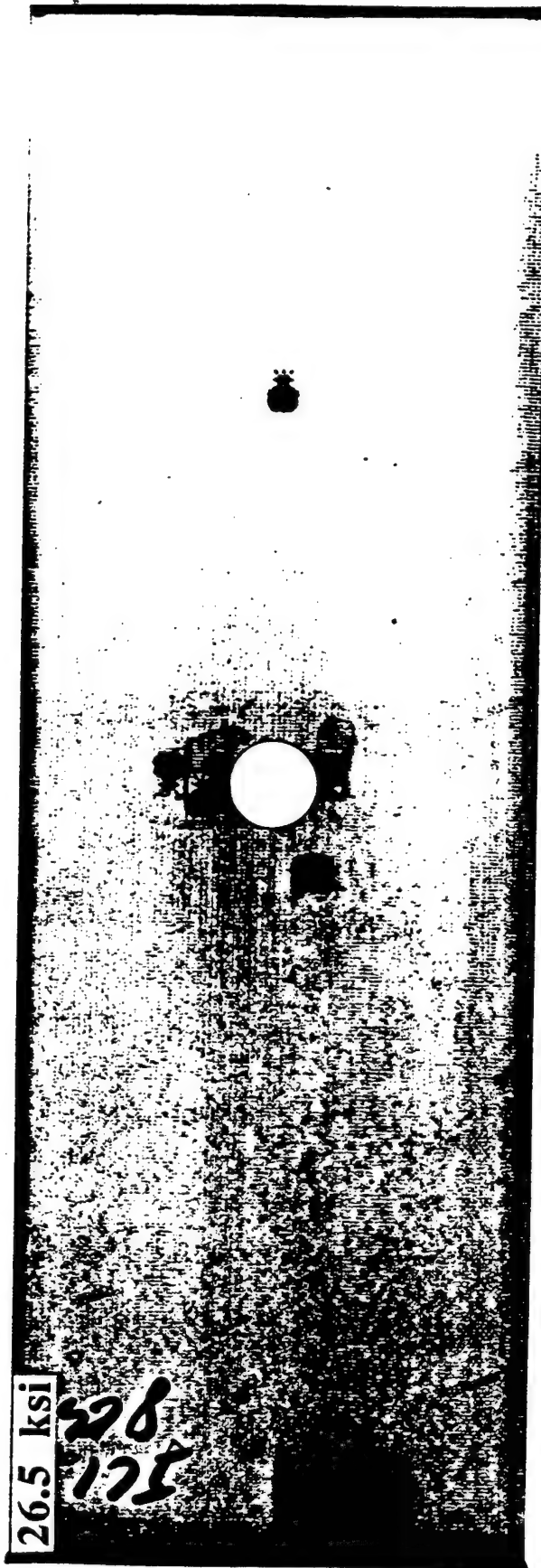


Figure 18. Radiographs of Damage:  $[0_2/90_2]_s$

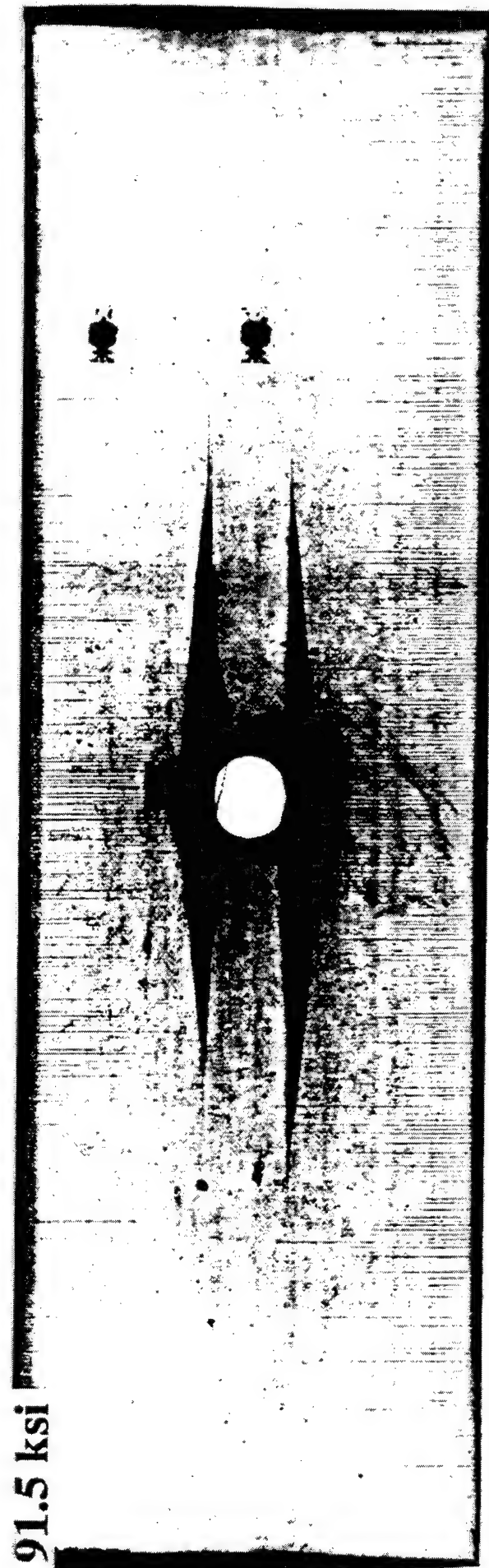


Figure 19. Radiographs of Damage:  $[0/90]_{2S}$



**TABLE 2**  
**Summary of Test Results**

Laminate	Hole Dia. (in.)	Width (in.)	No. of Specimens	Strength* (ksi)	Initial Damage* (ksi)	E, Msi	
						Exper.	Theory
[0] <sub>8T</sub>	0	0.50	4	383.3		23.3	
	0.50	3.00	3	369.9	26.5		
[90] <sub>8T</sub>	0	1.00	4	9.6	-	1.5	
	0.25	1.50	3	7.6	-		
	0.50	3.00	3	6.3	-		
	0.75	3.00	3	6.6	-		
	1.00	3.00	2	6.5	-		
[±45] <sub>2S</sub>	0	1.00	4	31.6	24.5	3.1	2.9
	0.25	1.50	3	28.7	13.6		
	0.50	3.00	3	30.6	12.4		
	0.75	3.00	2	29.1	10.8		
[±30/90] <sub>2S</sub>	0	1.00	4	61.5	33.7	7.7	7.5
	0.25	1.50	1	71.6	17.9		
	0.50	3.00	4	67.4	17.1		
	0.75	3.00	1	73.4	17.6		
[0/90] <sub>2S</sub>	0	1.00	3	220.9	90.4	13.1	12.8
	0.25	1.50	1	154.6	25.1		
	0.50	3.00	1	139.8	28.1		
	0.75	3.00	1	132.9	27.4		
[0 <sub>2</sub> /90 <sub>2</sub> ] <sub>S</sub>	0	1.00	5	209.2	86.3		
	0.50	3.00	3	188.1	25.4		

\*Ligament stress

lay-ups. Strain monitoring along with x-radiography appears to produce useful information on damage development as well as the state of strain around the hole. This work is being continued.

## 2.2 Changes in Laminate CTE Due to Microcracking

Many space structures require not only high stiffness but precision alignment and dimensional stability as well, which makes the low CTE of carbon fiber composites attractive. Composite laminates can be tailored to obtain a near-zero CTE which is essential to maintaining the dimensional stability of composite structures in a space thermal

environment. However, laminate CTE can change in service due to physical damage or material property changes associated with exposure to temperature fluctuations, outgassing, atomic oxygen, radiation, etc. Therefore, optimum selection and application of composites in space structures requires an understanding of how the service environment influences dimensional stability. For this study we have selected to investigate the influence of a common form of physical damage, viz. microcracking in the off-axis plies, on changes in CTE (and hence dimensional stability) of composite laminates. A number of studies have been reported in this area [8-10], but the influence of microcracking on changes in laminate CTE is still not fully understood. The ability to predict changes in a material's properties from the characterization of damage induced by mechanical and thermal loadings constitutes an important step in advancing the reliable use of polymeric composites in aerospace structures.

The main objective of this study, therefore, is to investigate the effect of microcracking on the change in CTEs through mechanical loading as well as thermal loading and applied to evaluate existing analytical models. The CTE variation due to matrix cracks for the AS4/3501-6 under applied mechanical loading has been reported in previous work. It was found to have good agreement between experiment and analysis for  $[0/90]_{2S}$  laminates under applied tensile loading. In this report the current status of our work and some of the results under thermal loading are reported. Transverse ply cracks were introduced in a rectangular specimen of cross-ply laminate by thermal cycling. After each prescribed number of thermal cycles, the specimen's CTE and crack density were measured. These experimental correlations between CTE and crack density will be compared with results from an analytical model.

### 2.2.1 Experiment

Material systems investigated in this project are a conventional aerospace graphite/epoxy (AS4/3501-6) and a high-modulus graphite fiber-reinforced cyanate ester (XN70/RS3). The AS4/3501-6 system exhibits characteristics ideal for a generic study of this nature: it is well-characterized and exhibits consistent properties. The laminates chosen are  $[0]_{8T}$ ,  $[0/90]_{2S}$ , and  $[0/45/90/-45]_S$  for XN70/RS3 and  $[0/90]_{2S}$  for AS4/3501-6. Panels were fabricated according to the manufacturer's recommended cure cycle, and then cut into rectangular specimens, 1"x3", using a diamond-impregnated saw. A total of eight specimens, two specimens for each laminate, were prepared. The free edges of the specimens were grounded and polished to enhance microscopic image for crack detection and count. Composite CTEs for all specimens were measured prior to thermal cycle as baseline data, and after each segment of thermal cycles (25, 50, 100, 300, 600, thereafter to be determined dependent upon the crack density).

Composite CTEs were measured using strain gages in conjunction with a computer-controlled temperature chamber and data acquisition system. Ultra-low-expansion titanium silicate was used as the reference material. WK-series 350 $\Omega$  strain gages from Micro-Measurements, Inc., with a gage length of 0.25 in., were employed. The strain gages were mounted with a high-temperature adhesive, and cured as recommended by the manufacturer. Two longitudinal and two transverse strain gages were mounted on each specimen.

The measurement system employed can accommodate eight channels; one was used for temperature, one for time, and the remaining six for collecting thermal strains. A software program controlled test parameters and continuous acquisition of

temperature and strain data. Data were collected during both heating and cooling cycles. A specimen was cycled between -150°F and 250°F at a rate of 5°F/min. and held for 15 minutes at each increment of 40°F of temperature. Thermal strains recorded at the end of each holding period were utilized for determination of CTE. The resolution of strain and temperature measurement with this experimental setup is better than  $1 \times 10^{-6}$  and 1°F, respectively. The correction for transverse sensitivity of the strain gage was made from the information supplied by the manufacturer.

### 2.2.2 Experimental Results

Figures 20 and 21 show some of the typical thermal strain data recorded for longitudinal and transverse direction of XN70/RS3 laminates, respectively, after 0, 25, 50, 100, and 300 thermal cycles. No ply crack has been observed for the unidirectional laminate. There is no sign of change in CTE for longitudinal and transverse directions. The CTE was obtained from a linear fit to the data over the entire test temperature range. The longitudinal CTE (four locations) ranged from  $-0.56$  to  $-0.65 \times 10^{-6}/^{\circ}\text{F}$ , with an average value of  $-0.6 \times 10^{-6}/^{\circ}\text{F}$ , while the transverse CTE ranged from  $14.7$  to  $15.4 \times 10^{-6}/^{\circ}\text{F}$ , with an average value of  $14.9 \times 10^{-6}/^{\circ}\text{F}$  before thermal cycles. The longitudinal CTE data have a wider scatter than the transverse data. The source of this scatter could be apparent strains from a mismatch in electrical properties of the two strain gages, and material variations within the laminate which arise from local variations in ply thickness, fiber alignment, and fiber volume.

Laminate longitudinal and transverse CTEs are fundamental thermal properties of a composite material and are used to calculate the thermal properties of various laminate orientations. These data will also serve to check the performance of strain gage systems, especially strain gage adhesion after subjection to thermal cycles. The variation of

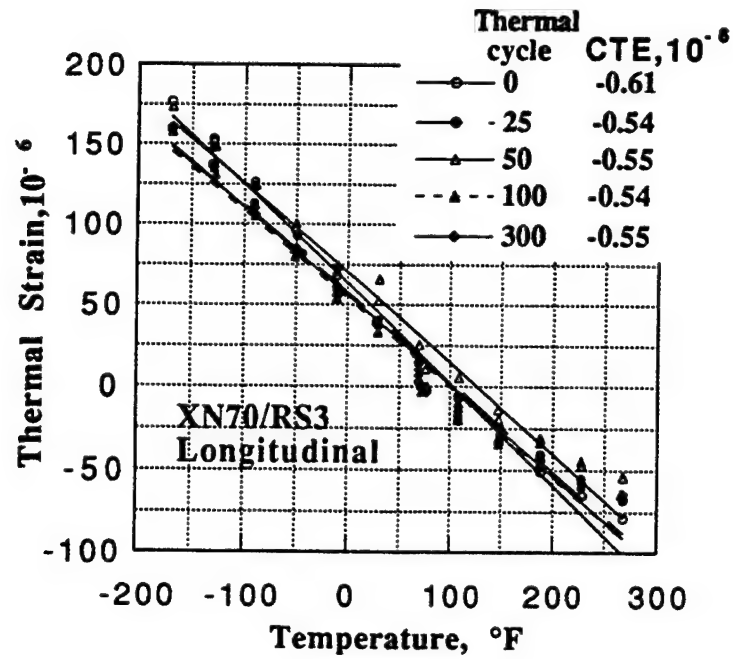


Figure 20. Longitudinal Thermal Strain vs. Temperature for  $[0]_{OT}$  after Subjecting to Thermal Cycles.

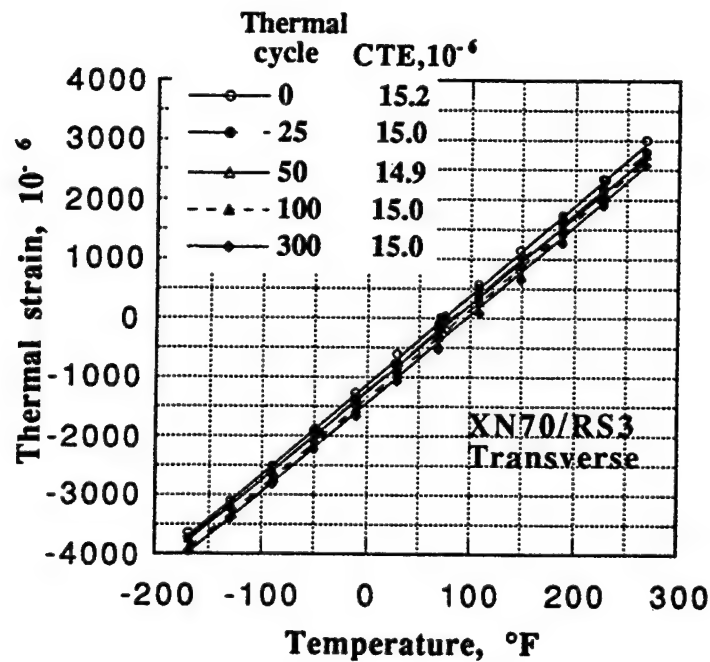


Figure 21. Transverse Thermal Strain vs. Temperature for the  $[0]_{OT}$  Laminate after Subjecting to Thermal Cycles.

longitudinal and transverse CTEs appears to be negligible due to the thermal cycles. No evidence of ply cracking was observed in the unidirectional laminate.

Figure 22 shows typical axial thermal strains as functions of temperature for a  $[0/90]_{2S}$  laminate of XN70/RS3 after thermal cycles. The number of thermal cycles, crack density, and corresponding CTE are also shown in the figures. This test is being continued until the crack density reaches saturation. Transverse cracking in a  $[0/90]_S$  laminate, induced by thermal loading, is reflected in a change in laminate CTE. An effort is being made to develop an analytical model for prediction of CTE due to thermally-induced cracks.

### **2.3 Interfacial Normal Strength Evaluation in Unidirectional Glass/Epoxy Composites**

Failure modes of fiber-reinforced composites are governed by the transfer of stress between the fiber and matrix. This transfer occurs across the interface between the constituents, and the properties of this interface therefore will affect the performance of the composite. The properties of the interface are, in turn, dependent upon the processing conditions employed. The literature on the characterization of interfaces in fiber-reinforced composites generally reveals a heavy emphasis on shear loading of the interface, wherein test methods such as the push-out test, the pull-out test, or the fragmentation test, are widely employed. Although the shear characteristics are important under longitudinal loading, especially in polymer- and ceramic-matrix composites, there are a number of scenarios where the normal tensile strength of the interface can be more important. One of the most important cases is clearly when loading is applied perpendicular to the fiber axis, where a good fiber-matrix bond strength would significantly increase the transverse load-carrying capability of the composite. Further, under axial loading, Pagano [11] has shown that the

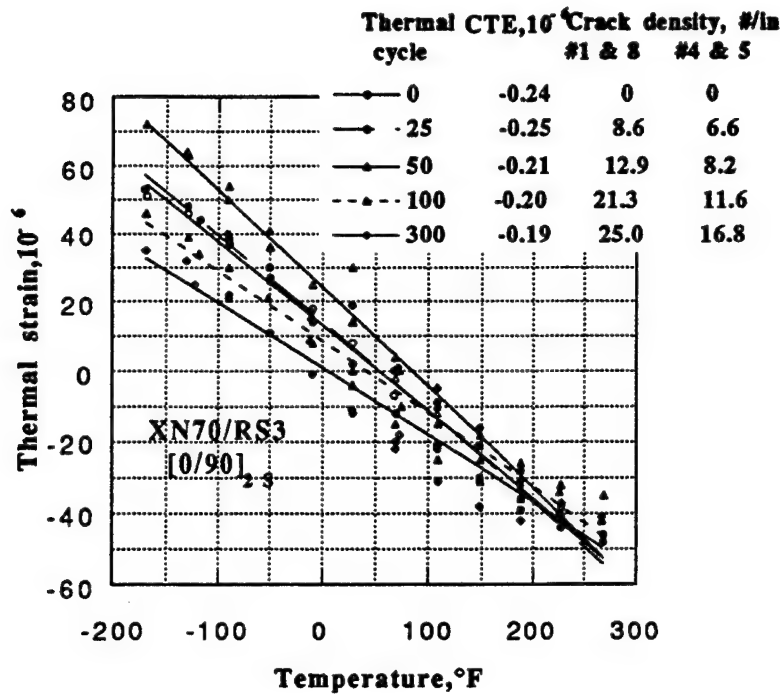
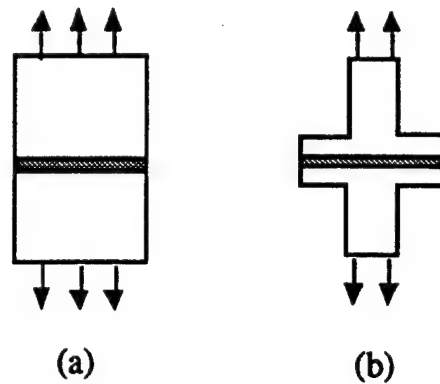


Figure 22. Thermal Strain vs. Temperature for the  $[0/90]_{2s}$  Laminate after Subjecting to Thermal Cycles.

tensile normal stress at the fiber/matrix interface plays a significant role in debonding the interface for a certain class of composites such as ceramic-matrix composites.

Unlike the interfacial shear strength, the measurement of interfacial normal strength has, to our knowledge, received only limited attention. A method that has often been used in the past to determine the interfacial normal strength has been to load a straight-sided specimen, with fiber ends exposed to the free surface (Figure 23a), in a direction transverse to the fiber axis. The basic problem with this specimen design is that an exposed fiber specimen contains a stress singularity at the fiber-matrix interface location where the fiber intersects the free surface. Consequently, in straight-sided specimens, the free surface is a favored site for interface debonding because of stress intensification at this location, and surface observation techniques and strain measurements in uniform-gage specimens may



**Figure 23. Specimen Geometry: (a) Straight-Sided Specimen and (b) Cruciform Specimen.**

therefore underestimate the actual interface debond stress [12]. In order to remove the influence of the free surfaces from the test, cruciform specimen geometry was introduced by Gundel et al. [13]. As shown in Figure 23b, the model composite sample is in the shape of a cross with an extremely large width in the gage section. Under transverse loading the central portion of the fiber/matrix interface is highly stressed, whereas the fiber has negligible loading in the arms/wings. Thus, interface debonding is forced to occur in the central region of the cross, so that the estimated bond strength is then free of edge effects. This is the major advantage of the cruciform geometry, as has been illustrated quite extensively in metal-matrix composites [13] and recently in polymer- [14] and ceramic-matrix [15] composites.

### 2.3.1 Experiment

In this work model composite specimens were cast in a cruciform-shaped silicone rubber mold. The model composite consisted of a single glass fiber reinforcement in epoxy matrix. The optical glass fiber was obtained from Polymicron Technologies Inc. and has an inner core 125  $\mu\text{m}$  in diameter and an outer polyimide layer 5  $\mu\text{m}$  thick. The matrix was an epoxy resin (Epon 828 from Shell Chemical Co.) cured with a polyetheramine



(Jeffamine D-230 from Texaco, Inc.) at ambient temperature. Fibers of predetermined length were positioned in the mold and then epoxy resin cast around them. These specimens were cured for three days at ambient temperature. The entire fiber surface was cleaned with acetone which enabled the epoxy to strongly bond with the reinforcement along the entire fiber length.

The two flat surfaces of specimens were progressively ground to the desired thickness, approximately 0.8 mm, and then polished using successively smaller diameter alumina polishing powder (final size was 0.3 micrometer) in order to enhance the microscopic image for interfacial debond detection. Three or four strain gages (gage length 0.38 mm) were mounted on the surface of certain specimens to monitor strain along the width during loading. Fiberglass/epoxy end tabs were adhesively bonded on the upright portion of the specimen.

A polarized microscope was employed to observe the onset and propagation of microcracks in the form of interfacial debonding, due to applied stress. Uniaxial tensile loading was applied to the specimen using a miniature loading device (hereafter referred to as straining stage) which was designed and built for *in situ* observation of damage in composite laminates. Axial force was generated by the pulling piston using nitrogen gas pressure. The straining stage is designed to be able to be mounted on the microscope stage for observation of microcracking or interfacial debond under loading. The specimen was mounted on the straining stage and loaded to a level which is slightly lower than the first expected debond level. Thereafter the specimen was loaded in increments until final failure. At the end of each load increment, the load was held constant during which the entire interface was microscopically examined for debonding, and the ensuing fringe pattern

captured using a Polaroid instant camera as well as a 35-mm camera. We have not made any effort to quantify the fringe patterns. Rather, the emphasis was to identify the location of stress intensification where failure would initiate.

Certain specimens are loaded to failure in an MTS machine, while strain and acoustic emission activity are continuously monitored.

### 2.3.2 Analytical Background

Under applied transverse tension to the fiber axis, the radial stress at the fiber/matrix interface is the dominant stress component for debond and is a maximum in the loading direction. Figure 24 shows the variation of normal stress across the interface in the loading direction as a function of distance from the specimen center. This normal stress at the interface is normalized with respect to the far-field applied stress, and thus represents a stress concentration factor (SCF), while the distance is normalized with respect to the fiber radius.

The 3-D finite element analysis shows a sharp increase in the SCF as the specimen edge is approached, indicating the existence of a strong stress singularity at the fiber end for both exposed and embedded fibers in straight-sided samples. On the other hand the central portion of the fiber/matrix interface is highly stressed in the cruciform geometry, whereas the fiber has negligible loading in the arms of wings as seen in Figure 24. Elastic properties of constituents required were experimentally measured for this study and listed in Table 3.

In these specimens thermally-induced stresses were not anticipated, since curing was done at room temperature, and therefore were not considered in the analysis. Due to the large number of elements that were anticipated (because of 3-D modeling), meshes

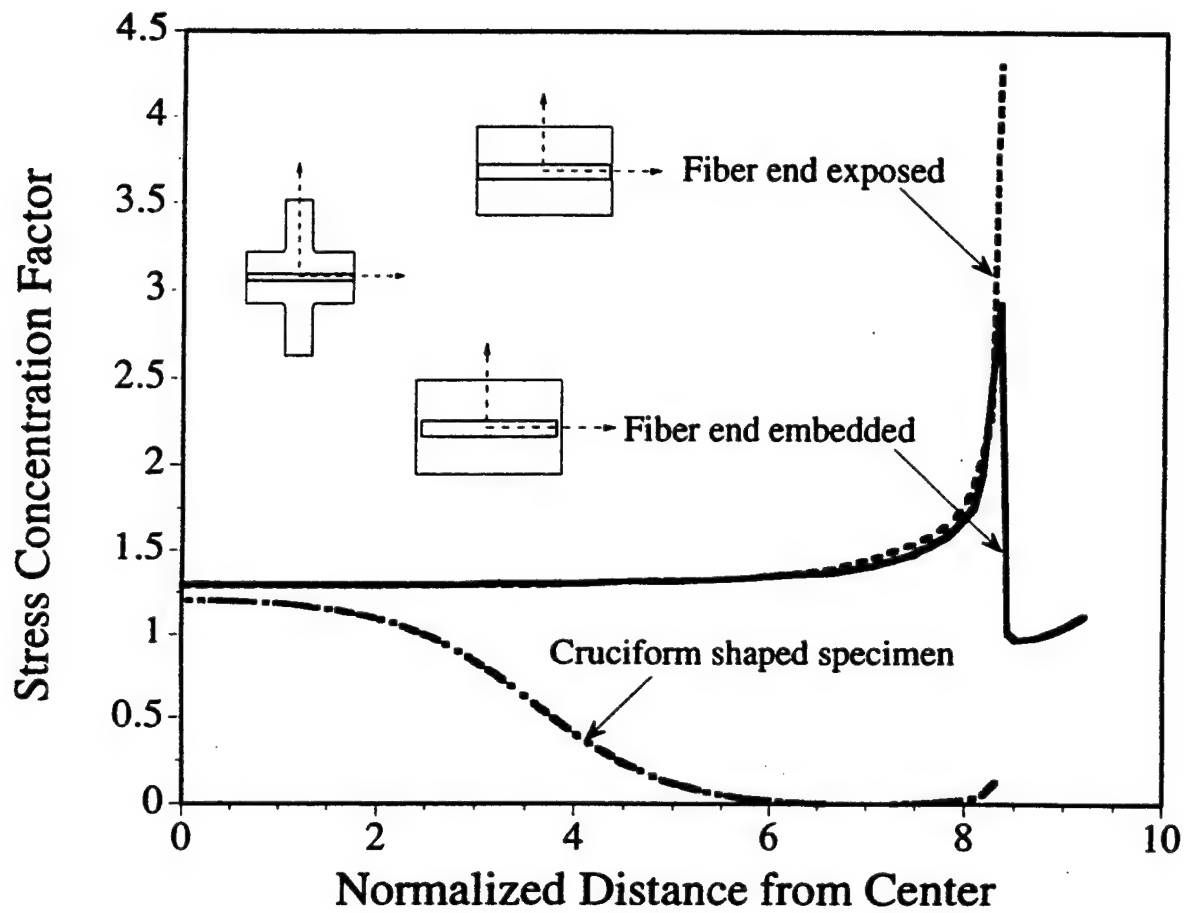


Figure 24. Comparison of Stress Concentration Factor in Model Single Fiber Composites.

TABLE 3  
Elastic Properties of Constituents

Constituents	E, GPa	$\nu$
Fiber	65	0.25
Epoxy	3.8	0.35

were generated such that computational efficiency would be maintained without sacrificing accuracy. Finer subdivisions were employed in the regions where the stress gradient was expected to be high, such as along the fiber-matrix interface.

The FE model was loaded by applying tension perpendicular to the fiber axis by means of constant displacement of the end nodes to simulate clamped-end conditions. Under transverse loading the radial stress at the interface is the dominant stress component and is a maximum in the loading direction. As shown in previous studies [13-15], the stress concentration factor (value of radial stress at the interface normalized by the externally applied stress) remains fairly constant (within 10 percent) over two-thirds of the central loading region. At locations further away from the center of the specimen, it decreases – gradually approaching zero value in the arms before increasing marginally near the free surface. As a result interface debonding is forced to occur in the center, thus avoiding the influence of free-edge or end effects on measured debond strengths. The tensile strength of the interface can then be obtained by multiplying the externally-applied stress at debonding with the stress concentration factor at the interface. Since failure in cruciform specimens initiates in the region free of initial stress singularities, the results produced by testing of these specimens are therefore capable of providing the true transverse response of the fiber-matrix interface.

### 2.3.3 Results and Discussion

Figure 25 shows the stress-strain curves obtained from strain gages mounted on the surface of the cruciform specimen at different distances from the central loading plane along the length of the fiber.

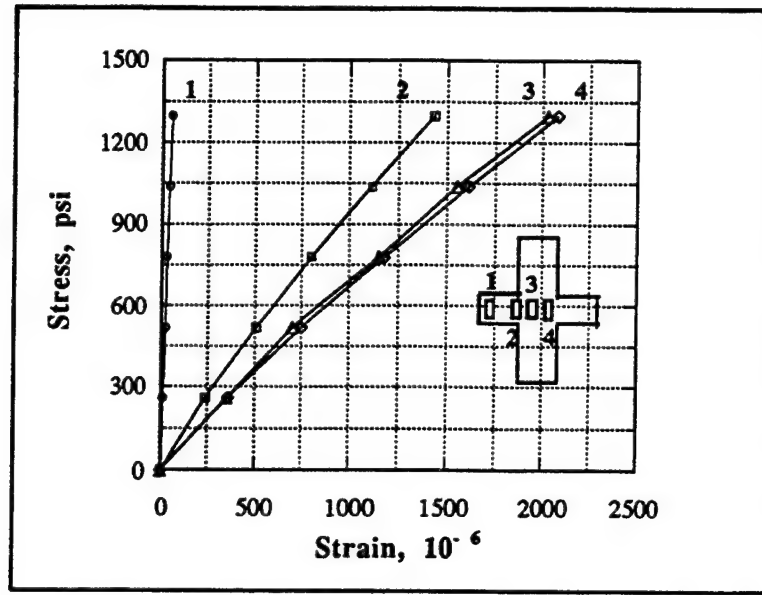


**Figure 25. Stress-Strain Curves at Various Locations along the Fiber Length.**

The strain gage locations are shown in the inset in Figure 25. For the cruciform specimen, the far-field stress is equated to  $P/(w_1 t)$ , where  $P$  is the applied load,  $w_1$  is the width of the loading arm, and  $t$  is the specimen thickness. The measured strain values indicate that the central portion of the fiber/matrix interface is highly stressed under tensile loading, whereas the fiber is nearly unloaded in the arms/wings. This is reflected in the lower strain values recorded by strain gage 1 located near the fiber end as opposed to the remaining gages 2-4. Moreover, the strain values are nearly uniform in the center over two-thirds of the loading region (as indicated by gages 3 and 4) before they decrease with distance measured from the central loading plane. Further, small fillets which were provided at the junctions of the cross help in reducing the stress concentration in the matrix at these locations. This is evidenced by the lower strain measurement at gage 2 compared to gages 3 and 4 which are mounted in the central region.

Figure 26 is a photomicrograph of the fractured halves of two different cruciform specimens clearly indicating that failure occurred mostly in the interface. However, for some specimens without end tabs, failure occurred at the grip in the rectangular section.

In order to identify the failure modes under transverse loading, fracture surface analysis was next conducted using scanning electron microscopy (SEM). Figure 27 shows a typical SEM photomicrograph of the fracture surface in the central region of the specimen. The fracture surface appears to be relatively smooth which is indicative of failure occurring due to radial normal stress alone. On the other hand, a rough (or hackle-like appearance) of the fracture surfaces would have been indicative of mixed-mode failure (i.e. failure due to radial normal stress in conjunction with shear stress).

An attempt was also made to identify the location of stress intensification along the fiber/matrix interface where debonding would initiate. Figure 28 shows the development of photoelastic fringe patterns in the central region of the cruciform specimen at two selected stress levels.

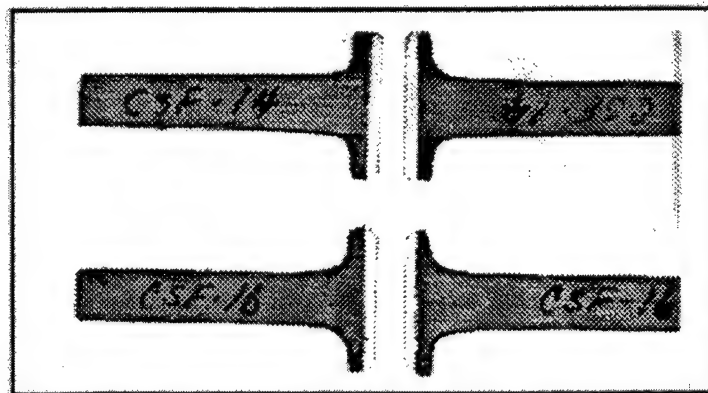


**Figure 26. Photograph Showing Failed Specimens.**

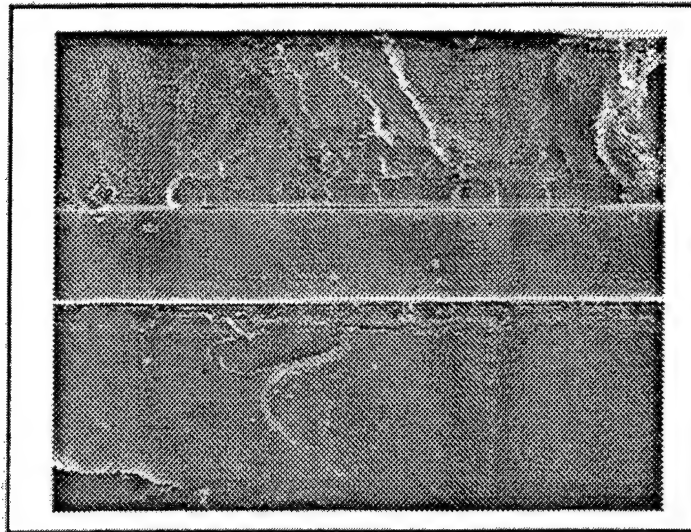


**Figure 27. Photomicrograph Showing the Fracture Surface.**

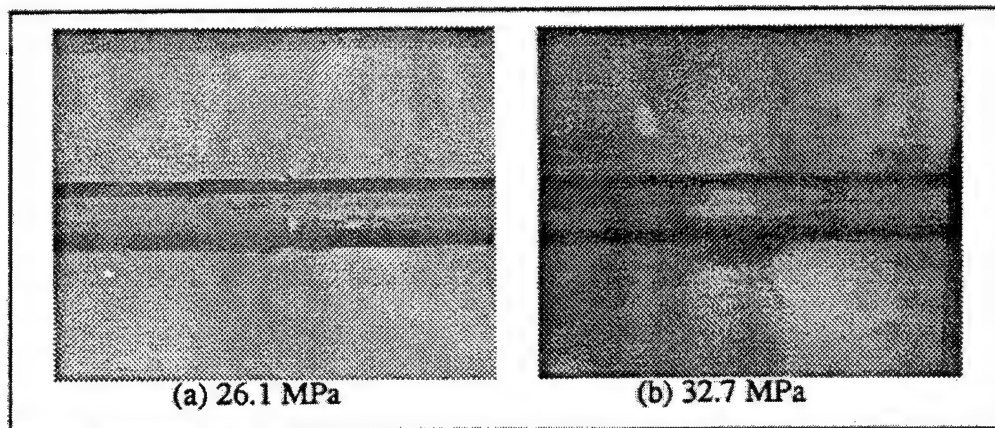


**Figure 28. Photomicrographs Showing Photoelastic Fringes for the Applied Stresses.**

The first appearance of photoelastic fringe occurred at the applied stress of 26.1 MPa as indicated by p in Figure 28a) and was confined to a very small area. This small fringe grew in intensity with increasing load, as shown at a stress level of 32.7 MPa in Figure 28b, until failure which occurred at 36 MPa.

Figure 29 is a photomicrograph of the same specimen taken after failure and clearly shows that the fiber was separated from the matrix. Thus, under transverse loading, interface debonding was the dominant failure mode for single-fiber glass/epoxy cruciform specimens.

It has been shown in this work that the single-fiber cruciform design was successful in eliminating the influence of free-edge stresses which are present in transverse testing of conventional straight-sided specimens. Inspection of photoelastic fringe pattern and stress-strain response indicated that stress intensification took place mainly in the central loading region, while microscopic examination of the failure surface revealed that the radial stress at the interface was mainly responsible for interfacial failure. These experimental observations were also found to be consistent with the numerical predictions using 3-D finite element analysis. The results reported in this study are a part of our continuing effort to employ the cruciform geometry to estimate the tensile normal strength of the fiber-matrix interface in unidirectional composites.

This work continues on the model specimens consisting of SCS-0 fiber and epoxy matrix.

## **2.4 Analysis of Bidirectional Laminates with Transverse Ply Cracks**

### **2.4.1 Effective Moduli**

Ply cracking is usually the first form of damage that develops in a laminated composite subjected to structural loading. These cracks can develop at relatively low load levels compared to ultimate failure. Loss of stiffness (or compliance) is a key indicator of transverse ply cracking. A number of studies have focused on the effect of transverse ply cracking on effective elastic moduli. Typical approaches to this problem are discussed in the next several paragraphs.



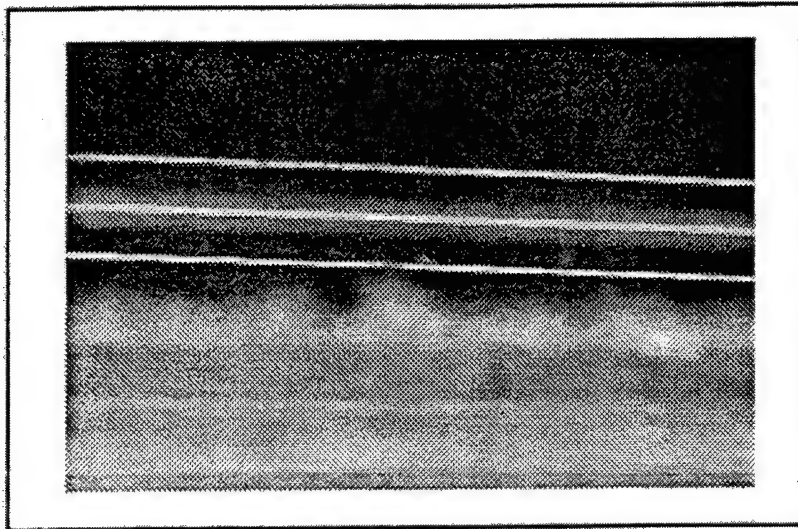


**Figure 29. Photomicrograph Showing the Separation of Fiber from the Matrix after Failure.**

Classical shear lag analysis has been used by a number of investigators to determine modulus reduction perpendicular to the cracked plies. One of the earliest models was developed by Highsmith and Reifsnider [16]. More recently Lee and Daniel [17] developed a closed form shear lag model for modulus reduction of bidirectional laminates. These models assume each ply is in a uniaxial state of in-plane stress. Tsai and Daniel [18] also developed a closed form shear lag type model for the determination of in-plane shear modulus of bidirectional laminates containing  $90^\circ$ -ply cracks. Typically shear lag analysis is based on the assumption of uniform in-plane stress over the ply thickness, and the development of shear stresses in a very thin boundary layer of unknown thickness between the layers.

Hashin [19] developed a variational model for determining reduction of axial and shear moduli due to the presence of  $90^\circ$ -ply cracks in bidirectional laminates. This model assumed that the in-plane stresses were constant through-the-thickness of each layer. Equilibrium considerations lead to a through-the-thickness linear distribution of interlaminar

shear stress and parabolic distribution of interlaminar normal stress. For the axial problem a uniaxial state of stress was assumed in each ply. An approximate elasticity solution based on average in-plane stresses was developed by Nuismer and Tan [20] for determination of in-plane stiffness reduction of balanced, symmetric laminates containing cracked  $90^\circ$  plies at the midplane. Interlaminar shear stresses were assumed to vary linearly through-the-thickness of each ply, while through-the-ply thickness integrated values of the interlaminar normal stress were assumed to vanish.

Tao and Sun [21] used finite elements in conjunction with the same class of laminates considered by Nuismer and Tan to determine axial and shear modulus reduction due to  $90^\circ$ -ply cracking at the laminate midplane. Yuan and Selek [22] used singular finite elements to predict reduction in axial modulus and stress intensity for bidirectional laminates containing  $90^\circ$ -ply cracks.

Schoeppner and Pagano [23] developed a method for modeling the thermoelastic response of flat laminates by utilizing a large radius axisymmetric hollow layered cylinder. Pagano and Schoeppner [24] applied this model to predicting stiffness reduction of bidirectional laminates containing  $90^\circ$ -ply cracks. In addition to obtaining in-plane moduli and Poisson's ratio, they also determined reduction in through-the-thickness modulus and Poisson's ratios. They refined their model by dividing homogeneous plies into a number of sublayers. Such subdivision was done primarily for the purpose of obtaining accurate stresses in the region of the crack front and to improve effective laminate stiffnesses for high crack densities where significant interaction occurs between adjacent cracks. As the cylinder radius increases, the axisymmetric cylinder model reduces to the flat laminate local model developed by Pagano [25].

In this study each of the  $0_m^0$  and  $90_n^0$  ply clusters is modeled as homogeneous, orthotropic material with the layers connected through continuity of displacements and tractions at the ply interfaces. The local model [18] and a modified shear deformation theory (SDT) are considered in the ply analysis. Both of these models are stress based, with the local model considering the effect of both transverse shear and normal stresses, while the modified SDT model considers only transverse shear stresses in addition to the usual in-plane stresses. Unlike previous studies all nine effective elastic constants are considered. The accuracy of a reduced ply stiffness (or ply discount procedure in which the transverse stiffness of the damaged ply is assumed to vanish) for determining reduction of elastic constants in the presence of  $90^\circ$ -ply cracks is also investigated. Numerical results are compared to other approaches such as shear lag analysis and the multilayer axisymmetric cylinder model.

Excellent agreement is obtained between the local and modified SDT models for predicting stiffness reduction due to  $90^\circ$ -ply cracking in bidirectional laminates. In addition the excellent agreement obtained between the local model and the multilayer axisymmetric cylinder model developed by Pagano and Schoeppner [24] suggests that subdivision of ply clusters of the same fiber orientation into sublayers is not required for determining accurate effective elastic constants at the laminate level. Also numerical results indicate that models, such as the shear lag analysis presented by Lee and Daniel, in which the stress through the thickness of each ply is assumed to be constant have merit relative to calculating the in-plane modulus,  $E_x$ , perpendicular to the cracked plies. This approach appears to be less accurate for determination of the in-plane shear modulus  $G_{xy}$ .

Although the modified SDT model requires vanishing of the transverse displacement, an interlaminar normal strain can be determined at the ply level by utilizing plane stress assumptions in conjunction with ply constitutive relations. This allows through-the-thickness elastic constants to be calculated. The modified SDT approach is not effective, however, in determining the transverse shear modulus  $G_{xz}$ .

In addition to being an effective tool for determining all nine elastic constants, the local model also has the advantage of being able to satisfy all free-edge boundary conditions, and each point within the repeating volume element (RVE) is in equilibrium. The axisymmetric cylinder model is not capable of modeling  $G_{xy}$ .

All of the in-plane elastic constants appear to approach the ply discount model as a lower bound with increasing crack density. Some of the crack densities required to reach this bound, however, are unrealistically high.

#### 2.4.2 Effective Thermal Expansion Coefficients

Ply cracking is usually the first form of damage that develops in a laminated composite subjected to structural loading. These cracks can develop at relatively low load levels compared to ultimate failure. Loss of stiffness (or compliance) is a key indicator of transverse ply cracking. A number of studies have focused on the effect of transverse ply cracking on effective elastic moduli.

Schoeppner and Pagano [26] developed a method for modeling the thermoelastic response of flat laminates by utilizing a large radius axisymmetric hollow layered cylinder. Pagano and Schoeppner [27] applied this model to predicting stiffness reduction of bidirectional laminates containing 90°-ply cracks. In addition they gave limited consideration to effective thermal expansion coefficients. They refined their model by

dividing homogeneous plies into a number of sublayers. Such subdivision was done primarily for the purpose of obtaining accurate stresses in the region of the crack front and to improve effective laminate stiffnesses for high crack densities where significant interaction occurs between adjacent cracks. As the cylinder radius increases, the axisymmetric cylinder model reduces to the flat laminate local model developed by Pagano [28].

In this study the local model [28] and a modified SDT are investigated for determining the effect of  $90^\circ$ -ply cracking on the reduction of effective thermal expansion coefficients (including through-the-thickness coefficient of thermal expansion) for  $[0_m/90_n]_s$  laminates. Both of these models are stress based, with the local model considering the effect of both transverse shear and normal stresses, while the modified SDT model considers only transverse shear stresses in addition to the usual in-plane stresses. Numerical results are compared to the multilayer axisymmetric cylinder model. The effect of cracking parallel to the fibers in the middle ply of a  $[\pm 45]_s$  laminate on effective thermal expansion coefficients is also investigated by transforming the effective thermal expansion coefficients of a  $[0/90]_s$  laminate.

Numerical results indicate excellent agreement between the local and modified SDT models. Good agreement also exists between these two models and the axisymmetric results presented by Pagano and Schoeppner [27] for a  $[0/90_3]_s$  graphite/epoxy laminate.

The in-plane thermal expansion coefficients appear to approach the ply discount model as a lower bound with increasing crack density. Some of the crack densities required to reach this bound, however, are unrealistically high.

For the case of a  $[\pm 45]_s$  laminate with center ply cracks parallel to the fibers, a shear coupling thermal expansion coefficient is present and the material becomes anisotropic. Significant values of this shear coupling thermal expansion coefficient are observed for increasing crack density.

## **2.5 Stress Analysis of Alternative Shear Tests**

Because of the weight introduced by the extensive use of mechanical fasteners, there is an increasing interest in adhesive bonding technology for joining structural parts. In the area of composite materials technology, this involves joining composites to other composites and/or composites to metals. In addition to the conventional structural need to join parts, bonding technology has become a key player in the area of composite material repair.

An important issue in adhesive bonding technology is determining the shear strength of a bonded joint. Various configurations for determining shear strength of an adhesive have evolved over the years. Among the various methods developed, those using a tensile type specimen for introducing shear load have become very popular. Of course the most famous of these is the single-lap joint. Because of the bending introduced into the single-lap specimen, many researchers have favored other geometries such as a double-lap configuration in order to reduce shear and peel stress concentrations near the boundary [29]. This specimen has been particularly popular for characterizing shear strength of joints in which composites are bonded to metal.

### **2.5.1 Cylindrical Composite Lap Joints**

An alternate approach to a single-lap joint is the use of a cylindrical lap joint. Such a configuration removes the double free-edge effect associated with any of the

tension-loaded flat coupon type specimens. In particular free boundaries associated with specimen edges are eliminated with the cylindrical configuration. However, free edges at the ends of the bondline still exist. This geometry also minimizes local bending effects characteristic of flat-type single-lap joints.

From a stress analysis standpoint, the free-edge zone near the boundaries of any lap-joint configuration where peak stresses occur causes considerable difficulty. In particular, many approaches (including finite elements) are unable to satisfy the proper free-edge boundary conditions. Finite-element models which approach the correct boundary conditions require more complex, higher-order elements.

In the present study a stress analysis of a cylindrical lap joint is developed in conjunction with a higher-order shell theory in which transverse shear and normal strain are included. In order to physically capture the proper free-edge effects, each component of the joint is considered as a separate homogeneous, orthotropic cylindrical shell with appropriate interface continuity conditions enforced. A sufficient number of boundary conditions are available with this approach to allow free-edge conditions to be satisfied. Thus the model produces classic free-edge behavior (vanishing shear stress and peak normal stress at the boundary). The present stress analysis is confined to the center region (gage section) of the cylindrical joint configuration.

Numerical results indicate, as usually encountered in classic free-edge behavior, the interfacial shear stress peaks a short distance inside the boundary and then dissipates rapidly. Thus, as in the case of all tension-loaded adhesive shear specimens, the shear stress distribution is very nonuniform and relegated to a region close to the boundary.

Solutions also indicate the existence of some local bending in the joint. In particular, symmetric behavior of the interfacial shear stress and antisymmetric response of the interlaminar normal stresses in the bond section of the joint are slightly perturbed.

#### 2.5.2 Analysis of a Composite Notched-Lap Joint Using Higher-Order Plate Theory

Because of the bending introduced into the single-lap specimen, many researchers have favored other geometries such as a notched joint, ASTM D3165. This specimen consists of two composites bonded together with notches cut in the top and bottom. Unlike a single-lap configuration, this geometry allows for an external axial load to be applied along the centerline of the specimen.

From a stress analysis standpoint, the free-edge zone near the boundaries of a notched-lap joint, where peak stresses occur, causes considerable difficulty. In particular, many approaches (including finite elements) are unable to satisfy the proper free-edge boundary conditions. Finite-element models which approach the correct boundary conditions require more complex, higher-order elements.

In the present study a stress analysis of a notched joint is developed in conjunction with a higher-order plate theory in which transverse shear and normal strain are included. In order to physically capture the proper free-edge effects, each component of the joint is considered as a separate plate with appropriate interface continuity conditions enforced. A sufficient number of boundary conditions are available with this approach to allow free-edge conditions to be satisfied.

In the numerical results (graphite/epoxy unidirectional adherend), a comparison is made between the interlaminar shear stress distribution when the adhesive layer is included and the case where the adhesive layer is neglected, i.e. for the double-notch



shear specimen (DNS). Surprisingly the DNS shows a larger peak stress with a shorter dissipation distance from the free edge. This may be an artifact of assuming the same shear traction at the top and bottom of the adhesive layer. It is also noted that the maximum interlaminar shear stress in both cases is very large, being on the order of 1.0 to 1.5 times the axial stress applied to the joint.

## **2.6 Three-Dimensional Mixed Variational Micromechanics Model for Textile Composites**

The fiber preforms used in composites manufacturing, instead of the traditional unidirectional prepregs, have been proven to provide low-cost composite parts. Moreover, complex geometry or contoured parts, which are difficult to make from unidirectional composites, can conveniently be made with fiber preforms. The two-dimensional woven fabric (textile) of fiber tows is known to be one of the most widely used fiber preforms in producing structural composite parts. To achieve the optimum structural properties of these parts, there is a need to develop a basic understanding of deformation/damage mechanics and failure mechanisms of textile composites.

The stiffness of fabric (woven) composites is well studied. However, the failure mechanism of this class of composites is not well understood. The prediction of the stiffness of woven composites is relatively simple compared to the prediction of strength, and has been done extensively in the literature, such as Zhang [30], Naik [31], Hahn [32], Yurgartis [33], and Marrey [34], to cite a few. Chou and Ko [35] provided a broad overview of this class of composites. However, the effect of yarn nesting and the failure mechanisms of woven composites are not well investigated, although some work has been done in this area. Naik [36], Karayaka [37], and others reported studies of the yarn nesting effects on the failure behavior of woven composites based on two-dimensional stress analysis. In the

vicinity of yarn crimping of two-dimensional fabric (woven) architecture, two perpendicular yarns crimp over and under to each other. Due to the perpendicular yarn crimping, even under the application of simple unidirectional load, the stresses in the vicinity of the yarn crimping are three-dimensional (Whitcomb [38]). Hence, two-dimensional stress analysis is not expected to offer a basic understanding of the failure mechanism of this material.

The failure in textile composites in general occurs in the vicinity of two perpendicular yarn crimping over and under to each other (Figure 30). In the vicinity of the yarn crimping, the stress is three-dimensional. To optimize the material properties and improve the performance of textile composites, we need to understand the physics and identify the stress components influencing the failure mechanism. *In situ* experimental observation [39-41] of damage initiation in textile composites reveals that the damage initiates in the form of interface cracks in the vicinity of yarn crimping, which is strongly influenced by the interlaminar stresses at the interface region. Thus an accurate prediction of the interlaminar stresses at the interface region is needed to reliably analyze damage and

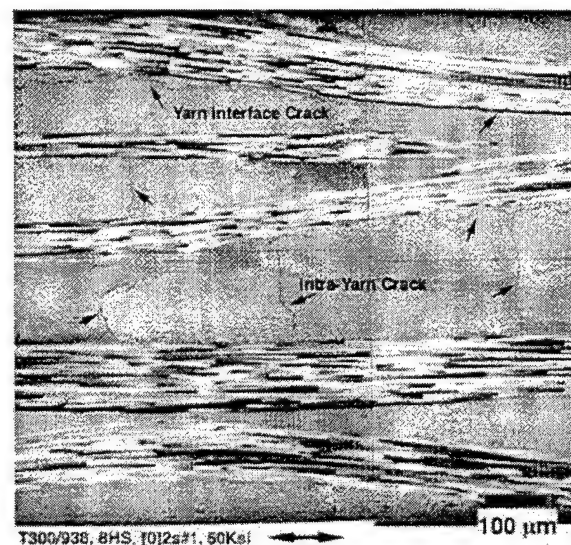


**Figure 30. A Representative Cross-Sectional Micrograph of a 8HS Woven T300/938 (Graphite/Epoxy) Composite after 50% of Failure Load.**

failure in woven composites. Most of the research work in this area, however, is based on two-dimensional stress analysis which does not reliably predict the interlaminar stresses. Further, traditional finite-element analysis only predicts stresses accurate at the Gaussian integration points; thus, even three-dimensional finite-element analysis does not yield accurate interlaminar stresses at the interface.

In order to obtain reliable interlaminar stresses at the yarn interface, a three-dimensional analytical model is developed based on the Reissner variational principle. An accurate prediction of the interlaminar stresses at the yarn interface is obtained by satisfying the interface traction continuity conditions and the equilibrium of stresses pointwise. The representative volume element (RVE) of the model is divided into several subregions; each subregion is occupied by a characteristic fabric yarn (Figure 31). The subregion surfaces of the RVE are shown in Figures 32(a)-32(f). The in-plane stresses within a yarn are assumed to vary linearly in the thickness direction, and the expressions for the interlaminar stresses are obtained by satisfying the three-dimensional equilibrium equations. After performing the thickness integration, the model yields a set of partial differential and algebraic equations which can approximately be solved by using cubic splines. The analytical derivation of the governing equations of the model is described below.

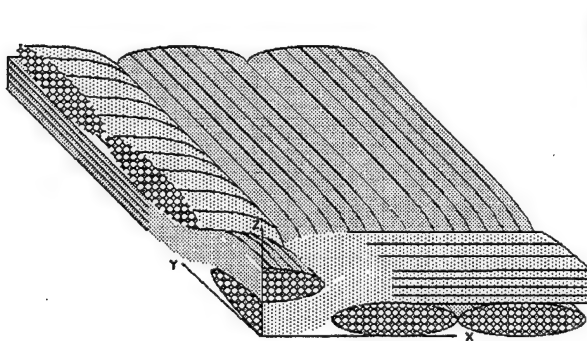


**Figure 31(a). RVE of a 2D Textile Composite.**

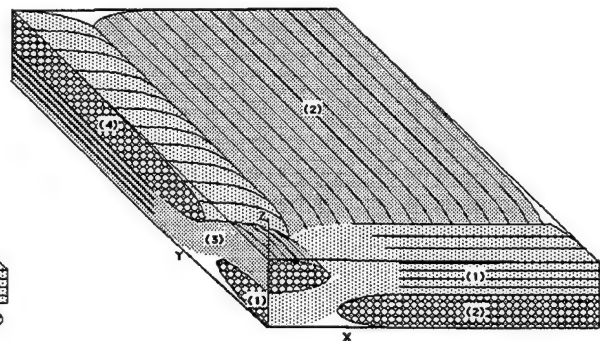
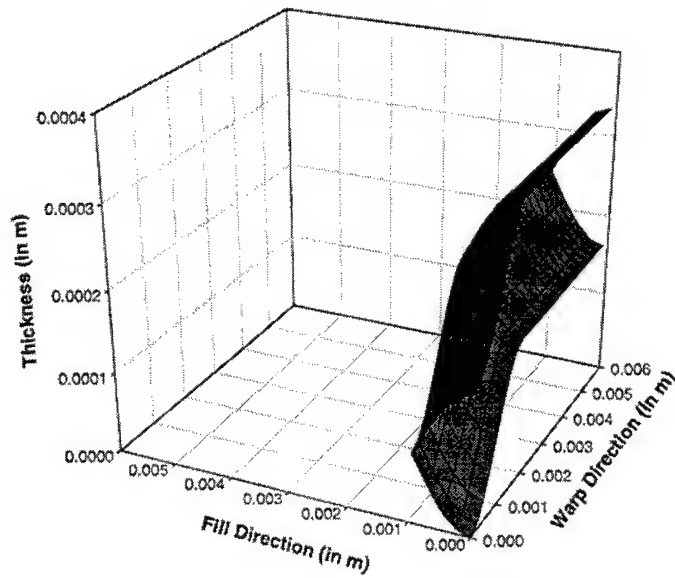


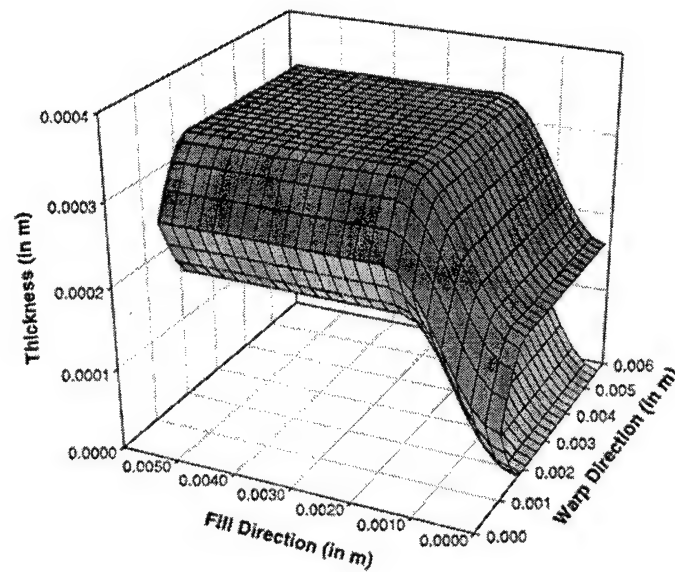
**Figure 31(b). RVE of the Model**

**Yarn Surfaces of 8HS Woven Fabric Composite  
(Yarn 1)**



(a)

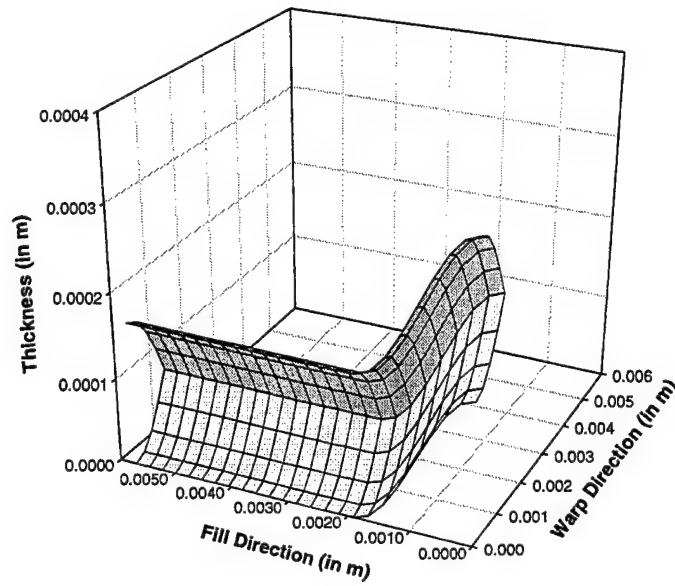
**Yarn Surfaces of 8HS Woven Fabric Composite  
(Yarn 2)**



(b)

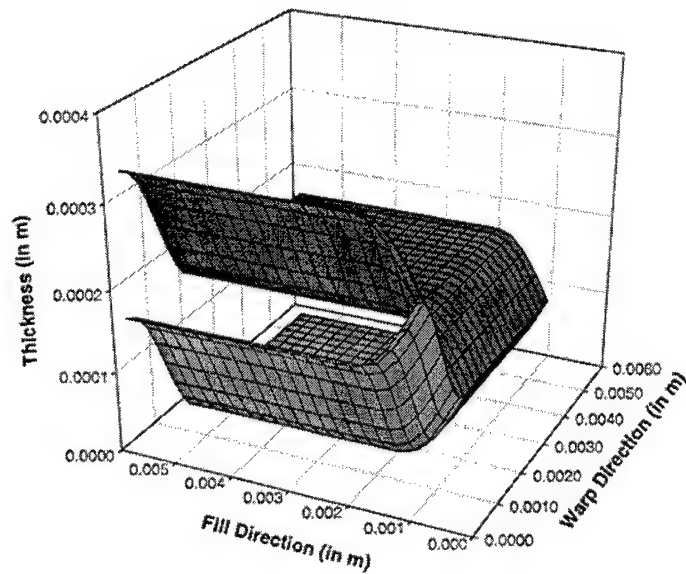
**Figure 32(a-f). Subregion Surfaces of the RVE.**

**Yarn Surfaces of 8HS Woven Fabric Composite  
(Yarn 3)**



(c)

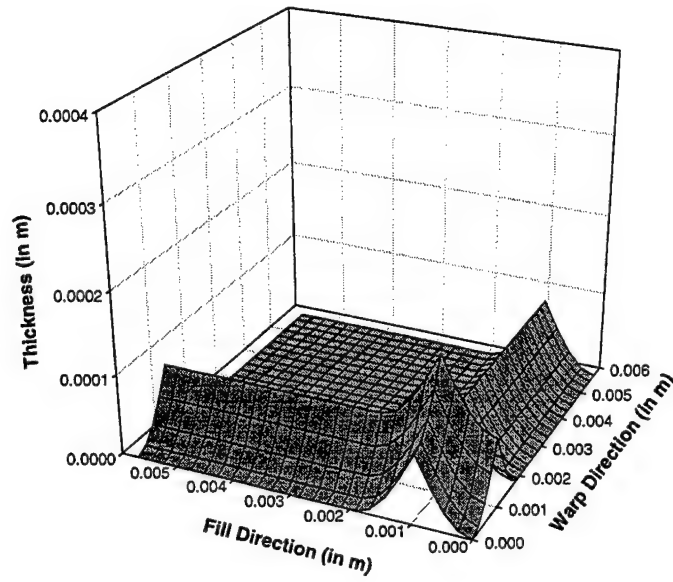
**Yarn Surfaces of 8HS Woven Fabric Composite  
(Yarn 4)**



(d)

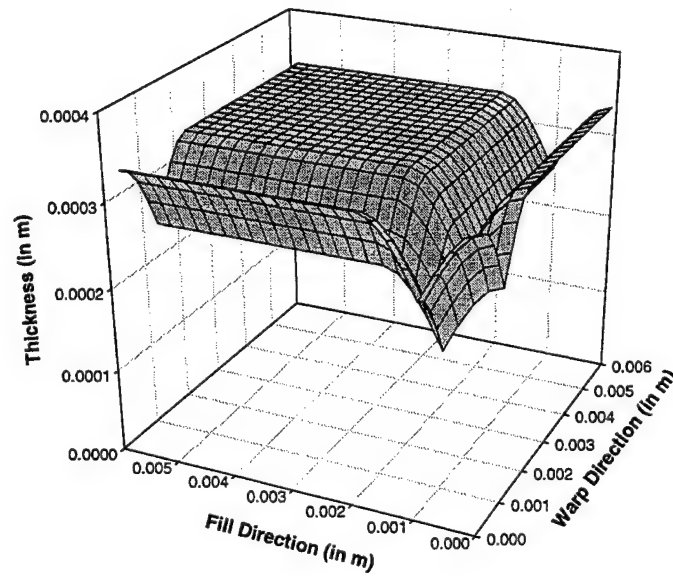
**Figure 32 (continued). Subregion Surfaces of the RVE.**

**Lower Matrix-Yarn Interface of 8HS Woven Fabric Composite**



(e)

**Upper Matrix-Yarn Interface of 8HS Woven Fabric Composite**



(f)

**Figure 32 (concluded). Subregion Surfaces of the RVE.**

The governing equations of elasticity, in terms of the Cartesian coordinates, (x, y, z), can be obtained from the following variational equation, developed by Reissner [42]

$$\delta J = 0 \quad (1)$$

where

$$J = \int_V F dV - \int_{S'} \tilde{\tau}_i u_i dS \quad (2)$$

and

$$F = \frac{1}{2} \sigma_{ij} (u_{i,j} + u_{j,i}) - W(\sigma_i, e_i) \quad (3)$$

In these equations, W is the strain energy density expressed in terms of the stresses  $\sigma_{ij}$ ; V is the volume; S the entire surface;  $\tilde{\tau}_i$  the prescribed tractions;  $u_i$  the displacement components; and S' is the portion of the boundary on which one or more traction components are prescribed. It is understood that both stresses and displacements are subjected to variation in the application of Equation (1), and summation over the range of repeated subscripts (but not superscripts) is implied throughout the work.

As described above, each yarn is modeled as homogeneous and transversely isotropic. The cross-sectional boundary of the yarn is confined by  $h_1$  (lower boundary) and  $h_2$  (upper boundary). Because of yarn waviness and elliptical cross-sectional boundary of the yarns,  $h_1$  and  $h_2$  are functions of both x and y.

Contracted notation is employed in the representation of the stress and strain components, i.e.,

$$\sigma_1 = \sigma_x, \sigma_2 = \sigma_y, \sigma_3 = \sigma_z, \sigma_4 = \sigma_{yz}, \sigma_5 = \sigma_{xz}, \sigma_6 = \sigma_{xy} \quad (4)$$

and analogous relation for the engineering strain components  $e_i$  (i=1-6).

The equilibrium equations are satisfied by assuming the following form for the stress components. The expressions of the stress components are as follows

$$\sigma_i = p_{iK} f_K^{(i)} \quad (i=1-6, K=1-4) \quad (5)$$

where  $p_{iK}$  are functions of  $x$  and  $y$  and  $f_K^{(i)}$  are functions of  $z$  only. The functions  $f_K^{(i)}$  associated with the in-plane stresses, as discussed above, are linear functions of  $z$ , and  $f_K^{(i)}$  associated with the interlaminar stresses are derived by satisfying the linear elasticity equations of equilibrium. The expressions for  $f_K^{(i)}$  are as follows

$$f_1^{(1)} = f_1^{(2)} = f_1^{(3)} = f_1^{(4)} = f_1^{(5)} = f_1^{(6)} = \frac{h_2 - z}{h_2 - h_1} \quad (6)$$

$$f_2^{(1)} = f_2^{(2)} = f_2^{(3)} = f_2^{(4)} = f_2^{(5)} = f_2^{(6)} = \frac{z - h_1}{h_2 - h_1} \quad (7)$$

$$f_3^{(3)} = f_3^{(4)} = f_3^{(5)} = \frac{z^2 - z(h_1 + h_2) + h_1 h_2}{(h_2 - h_1)^2} \quad (8)$$

$$f_4^{(3)} = \frac{2z^3 - 3z^2(z_1 + z_2) + z(h_1^2 + 4h_1 h_2 + h_2^2) - h_1 h_2 (h_1 + h_2)}{(h_2 - h_1)^3} \quad (9)$$

with

$$f_K^{(i)} = 0 \quad (i = 1, 2, 6 \text{ and } K = 3, 4; i = 4, 5 \text{ and } K = 4) \quad (10)$$

The strain energy density of an elastic anisotropic body, including the influence of free expansion, is given by

$$W = \frac{1}{2} S_{ij} \sigma_i \sigma_j + \sigma_i e_i \quad (11)$$

The expressions of the stresses are substituted in Equation (2) and the integration with respect to  $z$  is performed. The integration with respect to  $z$  also gives rise to weighted



average displacements and the displacements on the surfaces  $z = h_1, h_2$ . The definitions of the weighted displacements are ( $q$  may represent either  $u, v$ , or  $w$ )

$$[\bar{q}(x, y), q^*(x, y), \hat{q}(x, y)] = \int_{h_1}^{h_2} [H_1, H_2, H_3] q(x, y, z) dz \quad (12)$$

where

$$H_1 = \frac{h_2 - z}{(h_2 - h_1)^2}, H_2 = \frac{z - h_1}{(h_2 - h_1)^2}, H_3 = \frac{z^2 - z(h_1 + h_2) + h_1 h_2}{(h_2 - h_1)^3}$$

Further, because of the dependence of the subregion surface boundaries ( $h_1$  and  $h_2$ ) on  $x$  and  $y$ , Leibnitz's theorem in the following form must be applied on terms involving derivatives in  $x$  and  $y$ .

$$\int_{h_1(x, y)}^{h_2(x, y)} \frac{\partial}{\partial \xi} G(x, y, z) dz = \frac{d}{d\xi} \int_{h_1(x, y)}^{h_2(x, y)} G(x, y, z) dz - \frac{\partial h_2}{\partial \xi} G(x, y, h_2) + \frac{\partial h_1}{\partial \xi} G(x, y, h_1) \quad (13)$$

where  $\xi$  represents either  $x$  or  $y$ , and  $G$  is a general function of  $x, y$ , and  $z$ .

After substituting Equations (3)-(12) into (2), and using Equation (13) where appropriate, and taking the first variation we obtain

$$\begin{aligned} \delta J = & \iint_{xy} \sum_{k=1}^N [(\mu_{ij} + \chi_{ij})^{(k)} \delta p_{ij}^{(k)} - (F_1 \delta u + F_2 \delta u^* + F_3 \delta v + F_4 \delta v^* + F_5 \delta w + F_6 \delta w^* + F_7 \delta \hat{w})^{(k)}] dx dy \\ & + \iint_{xy} \sum_{k=1}^{N-1} \left[ \left( p_{52}^{(k)} - \frac{\partial h_2^{(k)}}{\partial x} p_{12}^{(k)} - \frac{\partial h_2^{(k)}}{\partial y} p_{62}^{(k)} \right) \delta u_2^{(k)} + \left( \frac{\partial h_2^{(k)}}{\partial x} p_{11}^{(l)} + \frac{\partial h_2^{(k)}}{\partial y} p_{61}^{(l)} - p_{51}^{(l)} \right) \delta u_1^{(l)} \right. \\ & + \left( p_{42}^{(k)} - \frac{\partial h_2^{(k)}}{\partial x} p_{62}^{(k)} - \frac{\partial h_2^{(k)}}{\partial y} p_{22}^{(k)} \right) \delta v_2^{(k)} + \left( \frac{\partial h_2^{(k)}}{\partial x} p_{61}^{(l)} + \frac{\partial h_2^{(k)}}{\partial y} p_{21}^{(l)} - p_{41}^{(l)} \right) \delta v_1^{(l)} \\ & + \left( p_{32}^{(k)} - \frac{\partial h_2^{(k)}}{\partial x} p_{52}^{(k)} - \frac{\partial h_2^{(k)}}{\partial y} p_{42}^{(k)} \right) \delta w_2^{(k)} + \left. \left( \frac{\partial h_2^{(k)}}{\partial x} p_{51}^{(l)} + \frac{\partial h_2^{(k)}}{\partial y} p_{41}^{(l)} - p_{31}^{(l)} \right) \delta w_1^{(l)} \right] dx dy \\ & + \iint_{xy} \left[ \left( p_{52}^{(n)} - \frac{\partial h_2^{(n)}}{\partial x} p_{12}^{(n)} - \frac{\partial h_2^{(n)}}{\partial y} p_{62}^{(n)} \right) \delta u_2^{(n)} + \left( \frac{\partial h_2^{(n)}}{\partial x} p_{11}^{(m)} + \frac{\partial h_2^{(n)}}{\partial y} p_{61}^{(m)} - p_{51}^{(m)} \right) \delta u_1^{(m)} \right. \end{aligned}$$

$$\begin{aligned}
& + \left( p_{42}^{(n)} - \frac{\partial h_2^{(n)}}{\partial x} p_{62}^{(n)} - \frac{\partial h_2^{(n)}}{\partial y} p_{22}^{(n)} \right) \delta v_2^{(n)} + \left( \frac{\partial h_1^{(m)}}{\partial x} p_{61}^{(m)} + \frac{\partial h_1^{(m)}}{\partial y} p_{21}^{(m)} - p_{41}^{(m)} \right) \delta v_1^{(m)} \\
& + \left( p_{32}^{(n)} - \frac{\partial h_2^{(n)}}{\partial x} p_{52}^{(n)} - \frac{\partial h_2^{(n)}}{\partial y} p_{42}^{(n)} \right) \delta w_2^{(n)} + \left( \frac{\partial h_1^{(m)}}{\partial x} p_{51}^{(m)} + \frac{\partial h_1^{(m)}}{\partial y} p_{41}^{(m)} - p_{31}^{(m)} \right) \delta w_1^{(m)} \Big] dx dy \\
& + \int_x \sum_{k=1}^N \left\{ (p_{61} - \tilde{p}_{61})^{(k)} \delta \bar{u}^{(k)} + (p_{62} - \tilde{p}_{62})^{(k)} \delta u^{*(k)} + (p_{21} - \tilde{p}_{21})^{(k)} \delta \bar{v}^{(k)} + (p_{22} - \tilde{p}_{22})^{(k)} \delta v^{*(k)} \right. \\
& + (p_{41} - \tilde{p}_{41})^{(k)} \delta \bar{w}^{(k)} + (p_{42} - \tilde{p}_{42})^{(k)} \delta w^{*(k)} + (p_{43} - \tilde{p}_{43})^{(k)} \delta \hat{w}^{(k)} \Big]_{z_k - z_{k-1}} \Big\}^2 dx \\
& + \int_y \sum_{k=1}^N \left\{ (p_{11} - \tilde{p}_{11})^{(k)} \delta \bar{u}^{(k)} + (p_{12} - \tilde{p}_{12})^{(k)} \delta u^{*(k)} + (p_{61} - \tilde{p}_{61})^{(k)} \delta \bar{v}^{(k)} + (p_{62} - \tilde{p}_{62})^{(k)} \delta v^{*(k)} \right. \\
& + (p_{51} - \tilde{p}_{51})^{(k)} \delta \bar{w}^{(k)} + (p_{52} - \tilde{p}_{52})^{(k)} \delta w^{*(k)} + (p_{53} - \tilde{p}_{53})^{(k)} \delta \hat{w}^{(k)} \Big]_{z_k - z_{k-1}} \Big\}^2 dy \\
& - \iint_{xy} \left[ (\tilde{\tau}_{x2} \delta u_2^{(n)} + \tilde{\tau}_{y2} \delta v_2^{(n)} + \tilde{\tau}_{z2} \delta w_2^{(n)}) \sec \alpha_n \sec \beta_n \right. \\
& \left. - (\tilde{\tau}_{x1} \delta u_1^{(m)} + \tilde{\tau}_{y1} \delta v_1^{(m)} + \tilde{\tau}_{z1} \delta w_1^{(m)}) \sec \alpha_m \sec \beta_m \right] dx dy = 0 \tag{14}
\end{aligned}$$

where  $\mu_{ij}$  and  $\chi_{ij}$  are defined below. The subscripts or superscripts  $m$  and  $n$  are associated with the bottom and top surfaces of the RVE, respectively, and  $\alpha$  and  $\beta$  are the angle of the slope of the surface of the subregion along the  $x$  and  $y$  directions, respectively.

All terms in Equation (14) are not independent. However, there are  $23N$  unknown variables ( $N$  being the total number of subregions) to be determined. After imposing the interface traction continuity conditions, we obtain the following governing equations representing the equilibrium, compatibility, and boundary conditions for the RVE.

(a) *Equilibrium equations*, for  $k=1, 2, \dots, N$  ( $7N$  equations)

$$F_1^{(k)} = F_2^{(k)} = F_3^{(k)} = F_4^{(k)} = F_5^{(k)} = F_6^{(k)} = F_7^{(k)} = 0 \quad \text{for } k=1, 2, \dots, N \tag{15}$$

(b) *Subregion compatibility equations*, for  $k=1, 2, \dots, N$ : (4N equations),

$$\chi_{33}^{(k)} = \chi_{34}^{(k)} = \chi_{43}^{(k)} = \chi_{53}^{(k)} = 0 \quad (16)$$

where

$$\chi_{ij}^{(k)} = \eta_{ij}^{(k)} - E_{ij}^{(k)} - \hat{S}_{ijkl}^{(k)} p_{kl}^{(k)} ;$$

$$\hat{S}_{ijkl}^{(k)} = \iint S_{ij}^{(k)} f_k^{(k)} f_l^{(k)} dx dy \quad (17)$$

(c) *Interface compatibility equations*, for  $k=1, 2, \dots, N-1$ : (12N-12 equations),

Consider a perfectly bonded interface between the  $k$ -th and  $l$ -th subregions (yarns). Here the  $l$ -th yarn is considered on top the of the  $k$ -th yarn (i.e.,  $l$ -th yarn is at a higher  $z$ -value than that of the  $k$ -th yarn).

$$\chi_{i1}^{(l)} + \chi_{i2}^{(k)} = 0 \quad \text{for } i = 1, 2, \dots, 6 \quad (18)$$

$$\chi_{12}^{(k)} + \frac{\partial h_k}{\partial x} \chi_{52}^{(k)} + \left( \frac{\partial h_k}{\partial x} \right)^2 \chi_{32}^{(k)} = 0 \quad (19)$$

$$\chi_{22}^{(k)} + \frac{\partial h_k}{\partial y} \chi_{42}^{(k)} + \left( \frac{\partial h_k}{\partial y} \right)^2 \chi_{32}^{(k)} = 0 \quad (20)$$

$$\chi_{62}^{(k)} + \frac{\partial h_k}{\partial x} \chi_{42}^{(k)} + \frac{\partial h_k}{\partial y} \chi_{52}^{(k)} + 2 \frac{\partial h_k}{\partial x} \frac{\partial h_k}{\partial y} \chi_{32}^{(k)} = 0 \quad (21)$$

$$p_{52}^{(l)} - \frac{\partial h_l}{\partial x} p_{12}^{(l)} - \frac{\partial h_l}{\partial y} p_{62}^{(l)} - p_{51}^{(k)} + \frac{\partial h_l}{\partial x} p_{11}^{(k)} + \frac{\partial h_l}{\partial y} p_{61}^{(k)} = 0 \quad (22)$$

$$p_{42}^{(l)} - \frac{\partial h_l}{\partial x} p_{62}^{(l)} - \frac{\partial h_l}{\partial y} p_{22}^{(l)} - p_{41}^{(k)} + \frac{\partial h_l}{\partial x} p_{61}^{(k)} + \frac{\partial h_l}{\partial y} p_{21}^{(k)} = 0 \quad (23)$$

$$p_{32}^{(l)} - \frac{\partial h_l}{\partial x} p_{52}^{(l)} - \frac{\partial h_l}{\partial y} p_{42}^{(l)} - p_{31}^{(k)} + \frac{\partial h_l}{\partial x} p_{51}^{(k)} + \frac{\partial h_l}{\partial y} p_{41}^{(k)} = 0 \quad (24)$$

(d) *Boundary conditions* (12 equations)

1. Top surface of the RVE (6 equations)

$$\chi_{12}^{(n)} + \frac{\partial h_2^{(n)}}{\partial x} \chi_{52}^{(n)} + \left( \frac{\partial h_2^{(n)}}{\partial x} \right)^2 \chi_{32}^{(n)} = 0 \quad (25)$$

$$\chi_{22}^{(n)} + \frac{\partial h_2^{(n)}}{\partial y} \chi_{42}^{(n)} + \left( \frac{\partial h_2^{(n)}}{\partial y} \right)^2 \chi_{32}^{(n)} = 0 \quad (26)$$

$$\chi_{62}^{(n)} + \frac{\partial h_2^{(n)}}{\partial x} \chi_{42}^{(n)} + \frac{\partial h_2^{(n)}}{\partial y} \chi_{52}^{(n)} + 2 \frac{\partial h_2^{(n)}}{\partial x} \frac{\partial h_2^{(n)}}{\partial y} \chi_{32}^{(n)} = 0 \quad (27)$$

$$\chi_{52}^{(n)} + \frac{\partial h_2^{(n)}}{\partial x} \chi_{32}^{(n)} + \tilde{u}_2^{(n)} = 0 \quad (28.1)$$

or

$$\cos \alpha_n \cos \beta_n p_{52}^{(n)} - \sin \alpha_n \cos \beta_n p_{12}^{(n)} - \cos \alpha_n \sin \beta_n p_{62}^{(n)} = \tilde{\tau}_{x2}^{(n)} \quad (28.2)$$

$$\chi_{42}^{(n)} + \frac{\partial h_2^{(n)}}{\partial y} \chi_{32}^{(n)} + \tilde{v}_2^{(n)} = 0 \quad (29.1)$$

or

$$\cos \alpha_n \cos \beta_n p_{42}^{(n)} - \sin \alpha_n \cos \beta_n p_{62}^{(n)} - \cos \alpha_n \sin \beta_n p_{22}^{(n)} = \tilde{\tau}_{y2}^{(n)} \quad (29.2)$$

$$\chi_{32}^{(n)} + \tilde{w}_2^{(n)} = 0 \quad (30.1)$$

or

$$\cos \alpha_n \cos \beta_n p_{32}^{(n)} - \sin \alpha_n \cos \beta_n p_{52}^{(n)} - \cos \alpha_n \sin \beta_n p_{42}^{(n)} = \tilde{\tau}_{z2}^{(n)} \quad (30.2)$$

2. Bottom surface of the RVE (6 equations)

$$\chi_{11}^{(m)} + \frac{\partial h_1^{(m)}}{\partial x} \chi_{51}^{(m)} + \left( \frac{\partial h_1^{(m)}}{\partial x} \right)^2 \chi_{31}^{(m)} = 0 \quad (31)$$

$$\chi_{21}^{(m)} + \frac{\partial h_1^{(m)}}{\partial y} \chi_{41}^{(m)} + \left( \frac{\partial h_1^{(m)}}{\partial y} \right)^2 \chi_{31}^{(m)} = 0 \quad (32)$$

$$\chi_{61}^{(m)} + \frac{\partial h_1^{(m)}}{\partial x} \chi_{41}^{(m)} + \frac{\partial h_1^{(m)}}{\partial y} \chi_{51}^{(m)} + 2 \frac{\partial h_1^{(m)}}{\partial x} \frac{\partial h_1^{(m)}}{\partial y} \chi_{31}^{(m)} = 0 \quad (33)$$

$$\chi_{51}^{(m)} + \frac{\partial h_1^{(m)}}{\partial x} \chi_{31}^{(m)} - \tilde{u}_1^{(m)} = 0 \quad (34.1)$$

or

$$\cos \alpha_m \cos \beta_m p_{51}^{(m)} - \sin \alpha_m \cos \beta_m p_{11}^{(m)} - \cos \alpha_m \sin \beta_m p_{61}^{(m)} = \tilde{\tau}_{x1}^{(m)} \quad (34.2)$$

$$\chi_{41}^{(m)} + \frac{\partial h_1^{(m)}}{\partial y} \chi_{31}^{(m)} - \tilde{v}_1^{(m)} = 0 \quad (35.1)$$

or

$$\cos \alpha_m \cos \beta_m p_{41}^{(m)} - \sin \alpha_m \cos \beta_m p_{61}^{(m)} - \cos \alpha_m \sin \beta_m p_{21}^{(m)} = \tilde{\tau}_{y1}^{(m)} \quad (35.2)$$

$$\chi_{31}^{(m)} - \tilde{w}_1^{(m)} = 0 \quad (36.1)$$

or

$$\cos \alpha_m \cos \beta_m p_{31}^{(m)} - \sin \alpha_m \cos \beta_m p_{51}^{(m)} - \cos \alpha_m \sin \beta_m p_{41}^{(m)} = \tilde{\tau}_{z1}^{(m)} \quad (36.2)$$

### 3. PROCESSING SCIENCE OF COMPOSITES

#### 3.1 Processing for Dimensional Control

Composite processing involves the cure and/or solidification of a matrix at an elevated temperature, with accompanying shrinkage, that imposes compressive stresses on the reinforcing fibers. As the temperature is lowered to ambient, differential thermal expansion between the fibers and the matrix result in the buildup of additional internal stresses in the composite. On a macro level, anisotropy in the ply coefficient of thermal expansion (CTE), arising from the anisotropy in fiber stiffness and CTE, manifests itself in ply residual stresses in multidirectional laminates. These stresses exert a marked influence on the onset of damage in fiber-reinforced composites under applied load and may even be large enough to induce microcracking in the part on cool-down from the processing temperature. In addition residual stresses can distort the dimensions or shape of the

processed part, necessitating expensive compensation through the use of shims when it is assembled in a structure. Residual processing stresses are inevitable; understanding how they build up can facilitate their reduction through appropriate process control and part design, while estimates of their magnitude can be used to accommodate their influence in appropriate tool design, allowing the fabrication of a part of net shape and dimensions. Various techniques have been employed to estimate total residual stresses in a composite, including a ply-peel method for cross-ply laminates [43] and determination of the stress-free temperature of the material system from measurements of the deflection of an unsymmetric composite strip as a function of temperature [44]. What these techniques have in common is that measurements are conducted on the cured composite which does not allow separation of thermal and cure shrinkage stresses.

Embedded strain gages were employed to determine, *in situ*, the buildup of residual strains in carbon fiber-reinforced polymer composites *during* cure. This technique was first introduced by Daniel and coworkers [45] about 25 years ago as a means of comparing surface and subsurface strains in boron/epoxy laminates subjected to axial tensile loading. It was later applied to the measurement of *thermal* residual strains in boron/epoxy and glass/epoxy laminates [46] and hybrid graphite/Kevlar/epoxy and graphite/glass/epoxy laminates [47] during cool-down from the cure temperature after resin solidification was complete. White and Hahn [48] bonded strain gages to the outermost ply of a graphite/BMI laminate and monitored changes in strain during cure, to correlate changes in thermal strain with degree of cure of laminates cured to different extents. In these studies the focus of the work was on quantification of residual strains, arising from differential thermal expansions and anisotropy of the constituents, during cool-down, after resin solidification was complete.

In our study the use of embedded strain gages was revisited and adapted for composite cure in an autoclave to explore, in real time, residual strains arising from chemical shrinkage of the thermosetting matrix *during* cure.

### 3.1.1 Experimental Details

The composite systems investigated, in unidirectional and cross-ply lay-ups, were AS4/3501-6, a standard graphite/epoxy; IM7/977-3, a toughened graphite/epoxy; and IM7/5250-4, a toughened graphite/bismaleimide. The buildup of residual strains during composite cure was measured with WK-00-250BG-350 strain gages from Micro-Measurements, Inc.

Composites measuring 6"x6" were laid up in the prescribed configurations and strain gages bonded to the surface plies and/or embedded at selected ply interfaces in the 0° or 90° directions. In all cases the gage element was located at least 0.5" from a free edge. While the strain gage itself is encapsulated, the gage leads were insulated from the conductive reinforcing carbon fibers with Kapton (polyimide) tape. The stack of prepreg was then vacuum-bagged and the composite initially cured, under vacuum, in a forced-convection oven. Subsequent cures were conducted in an autoclave, using the setup described in the sketch in Figure 33, in accordance with the manufacturers' recommended cure cycles. By using a gage from the same production lot, bonded to an ultralow-CTE titanium silicate block, as part of the Wheatstone half-bridge, the output of the active gage was compensated for temperature and pressure variations in the autoclave to yield the strain arising solely from composite cure. After completion of cure the same embedded gages were employed to monitor strain of the freestanding IM7/5250-4 panel during the manufacturer's recommended postcure cycle. The CTEs of the cured panels were then measured for

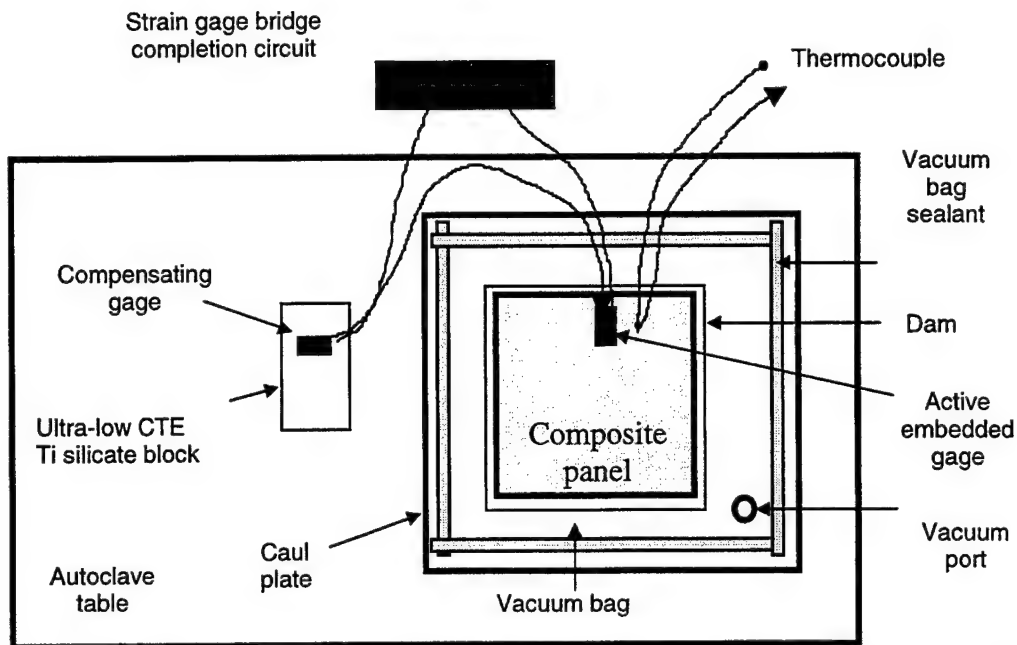


**Figure 33. Sketch of the Experimental Setup to Measure the Buildup of Residual Strains during Composite Cure in an Autoclave.**

comparison with the thermal strains generated during cool-down from the initial cure.

Sections were then cut from the composites and fiber volumes determined by acid digestion, or image analysis of polished cross sections. Table 4 provides a summary of the experiments conducted.

**TABLE 4**  
**Composite Panels Cured with Embedded Strain Gages**

Cure	Material	Laminate	$V_f$ (%)	# Gages	Gage Location/Orientation*			
					1	2	3	4
Oven ...	AS4/3501-6	$[0]_{16T}$	50	4	SA	SA	ST	ST
				2	ST	MT		
		$[0_2/90_2]_S$	50	2	SA	ST		
Autoclave	AS4/3501-6			4	SA	MA	ST	MT
		$[0]_{16T}$	69	3	SA	ST	MT	
		$[0]_{16T}$		3	ST	MT	MT	
	IM7/977-3	$[0/90]_{3,48T}$	55	3	ST	IT	MT	
		$[0]_{16T}$	70	2	MA	MT		
		$[0]_{16T}$	64	2	MA	MT		

\*S – surface, I – interior, M – midplane; A – axial, T – transverse to fibers



### 3.1.2 Cure of AS4/3501-6

The technique of measuring strain from embedded gages during composite cure in a vacuum bag was developed and refined with the cure of AS4/3501-6 composite panels in an oven. The cure is similar to that of panels processed in the autoclave, with the exception that the low vacuum pressure (compared to the 100 psi applied during the autoclave cure) generates a lower fiber volume. Figure 34 shows the variation in axial and transverse strain of a  $[0]_{16T}$  AS4/3501-6 composite during vacuum-bag cure in an oven. Strain increases linearly with free expansion of the gage between A and B, remains constant during the first isothermal hold (B-C) and increases again during the ramp to 350°F (C-D) while the resin is fluid. Gelation begins at 350°F with attendant cure shrinkage; changes in axial and transverse strains during this isothermal hold (D-E) imply the formation of a bond between resin and strain gage, necessary to transfer to the gage the (observed) strain resulting from the resin shrinkage. It is reasonable to assume that the bond (for stress transfer)

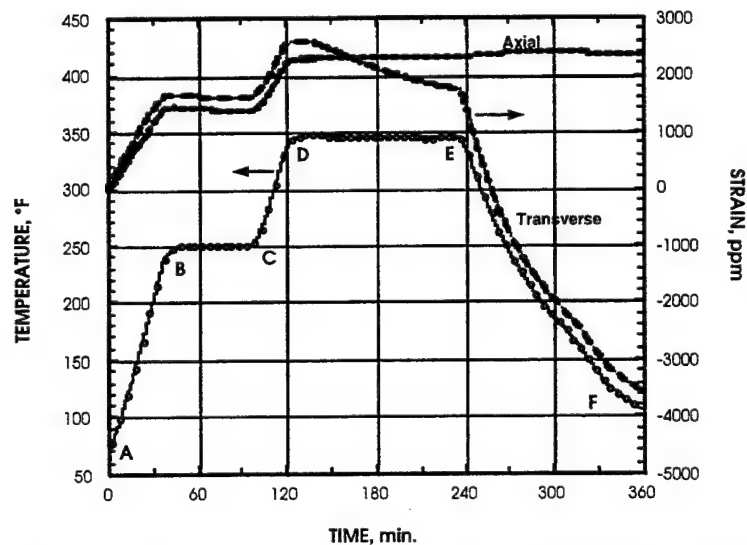
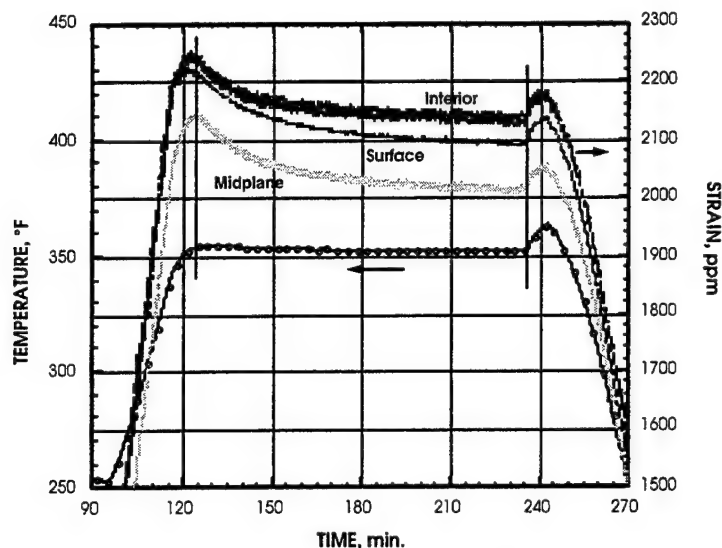


Figure 34. Plots of Strain Generated in a  $[0]_{16}$  Composite of AS4/3501-6, Measured with Embedded Strain Gages, During Vacuum-Bag Cure in an Oven.

between cured resin and reinforcing fiber is established at the same time as that between resin and strain gage. Therefore, residual stresses in the laminate can be assumed to initiate at the instant a measurable decrease in strain is recorded by the transverse strain gage. From Figure 34 this appears to occur very shortly after the start of the second isothermal hold at 350°F. If residual stress buildup had initiated during the ramp C-D, the axial and transverse strains would have deviated and not continued to change at the same rate with temperature.

From an expanded view of the plot, the axial strain is seen to increase slightly during the cool-down to ambient conditions, reflecting the negative axial CTE of the carbon fibers; the high transverse CTE of the ply, on the other hand, results in a significant decrease in transverse strain. Transverse thermal strains were measured again in the cured laminate, using the same embedded gages, and the results compare well with the thermal strains generated during cool-down. To determine if chemical shrinkage was complete with this cure cycle, a similar panel was cured with an extended hold at 350°F; from the data it was evident that in the standard cure cycle chemical shrinkage is incomplete in the two-hour hold at 350°F. From an analysis of strain measurements during cure, it appears that with the conventional cure cycle, approximately 10-15 percent of the total residual strain that arises during processing is due to resin chemical shrinkage.

A  $[90_6/0_2/90_6/0_2/90_3/0_2/90_3]_S$  cross-ply panel was vacuum bagged and cured in the autoclave using the conventional cure cycle and 90°-ply strains measured, *in situ*, at the surface, between the 12th and 13th ply, and at the midplane (between the 24th and 25th ply). Temperatures measured at these same interfaces were identical during the cure. The three strains are plotted in Figure 35 over the section of the cure profile corresponding to the second hold at 350°F. Shrinkage strains in all three cases are similar, ranging from 100



**Figure 35. Section of a Plot of Strains Generated in a  $[0/90]_{3,48T}$  Laminate of AS4/3501-6, at Different Ply Interfaces, During Cure in an Autoclave.**

to 130 microstrain. The CTE determined from the thermal strains, measured during cool-down, agree well with subsequent measurements on the cured panel and analytical predictions based on unidirectional ply data.

### 3.1.3 Cure of IM7/977-3

IM7/977-3 is a toughened epoxy developed for application in primary and secondary aerospace structures where impact resistance and excellent hot/wet performance are crucial. The toughener is expected to alter the shrinkage characteristics of this material system, as is evidenced from the plot in Figure 36 of axial and transverse strains developed during the cure of a  $[0]_{16T}$  composite in the autoclave. From this figure it is apparent that residual strains start to build up after approximately 30 minutes into the six-hour hold at 350°F. Two competing effects determine the net strain measured in this region: cure shrinkage, which increases the residual strain, and viscoelastic relaxation which reduces the residual strain built up. The net transverse residual strain resulting from resin cure

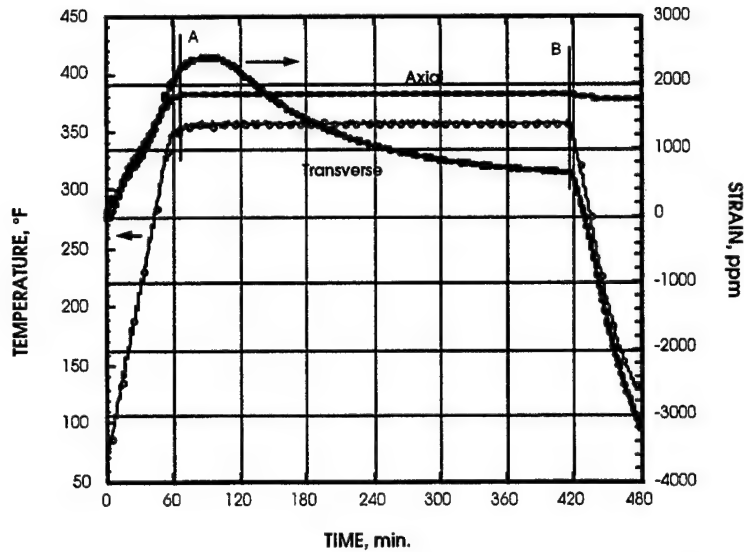


**Figure 36. Plots of Strain Generated in a  $[0]_{16}$  Composite of IM7/977-3, Measured with Embedded Strain Gages, During Cure in the Autoclave.**

shrinkage is greater in this material system than in unidirectional AS4/3501-6 (approximately 1720 vs. 960 microstrain, respectively) and also comprises a larger fraction of the total strain (29 percent vs. 14 percent, respectively). Consequently, there is greater incentive to alter the process cycle of IM7/977-3 in order to reduce the strains arising from matrix cure shrinkage.

#### 3.1.4 Cure of IM7/5250-4

This material is a toughened bismaleimide composite designed for structural applications with service temperatures greater than can be accommodated by epoxy composites. The material is cured at 375°F with a postcure designed to give the desired compromise between toughness and high T<sub>g</sub>. For most aerospace structures the composite is postcured for 6 h at 440°F. Residual strain buildup during cure and postcure of a  $[0]_{16T}$  composite is shown in Figure 37. In spite of the addition of a toughener, the strain generated by chemical shrinkage during cure (900 ppm) is on par with that generated in the untoughened AS4/3501-6 (960 ppm). However, further cure shrinkage occurs during the postcure with an additional 450 ppm of shrinkage strain; as a result the thermoelastic strain

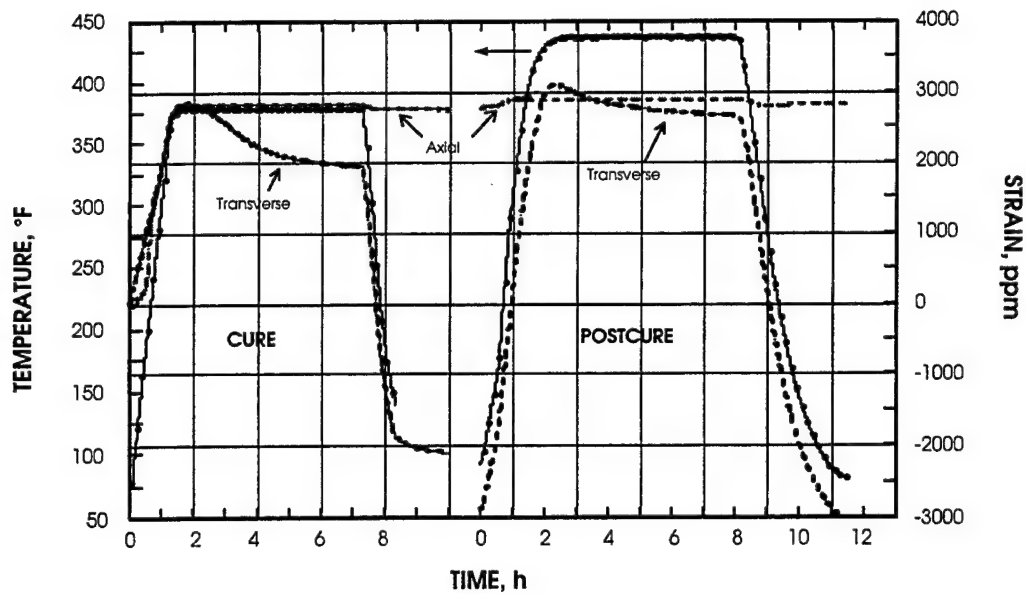


**Figure 37. Plots of Strain Generated in a  $[0]_{16}$  Composite of IM7/5250-4, Measured with Embedded Strain Gages, During Cure and Postcure in the Autoclave.**

developed in the composite increases from 4930 ppm, after cure, to 5660 ppm, after postcure. The net shrinkage strain for the combined cure and postcure comprise approximately 19 percent of the total residual strain in this composite under ambient conditions.

Embedded strain gages appear to be a promising route to monitoring, in real time, residual strains developed in a laminate as it is processed, and can provide quantitative distinction between thermoelastic and shrinkage strains, as summarized in Table 5 for the three composite systems studied. Consequently, they may potentially serve as sensors for feedback control of the process parameters to minimize these stresses.

### **3.2 Integration of Sensors for Intelligent Composites Processing**

Software for data acquisition and control of the resin infusion system has been completed and tested. The program is generalized to handle several different analog input/output boards (Data Translation and MetraByte) with proportional-integral-derivative

**TABLE 5**  
**Summary of Transverse Residual Strains in Unidirectional Composites,**  
**Measured during Cure with Embedded Strain Gages**

<b>Composite</b>	<b>Fiber Vol. (%)</b>	<b>Strain due to Cure Shrinkage (ppm)</b>	<b>Thermal Strain @ 75°F (ppm)</b>	<b>Total Residual Strain @ 75°F (ppm)</b>	<b>Shrinkage/ Total Strain Ratio</b>
AS4/3501-6 (oven)	50	915	6020	6935	0.13
AS4/3501-6 (autoclave)	69	960	5750	6710	0.14
IM7/977-3	70	1720	4130	5850	0.29
IM7/5250-4	64	900, 450*	4930, 5660*	7010	0.19

\*Strains resulting from cure and postcure, respectively.

(PID) controller support. The program is written to allow for easy modification to accommodate a variety of sensors and control elements.

For the current setup of the resin infusion system, this program monitors resin temperature throughout the resin transport line. Two banks of heaters, one at the inlet and one in the midsection of the transport line, are controlled by proportional-integral action. Four heating pads are similarly controlled for heating the preform while it is being infused and for heating to the final cure temperature. The resin is transported by a systolic pump with open-loop control. The resin state and preform wet-out are also monitored by the dc-resistance of the resin.

It should be pointed out that although the temperature controller is implemented with PI action, it is only on-off action at the heating element level. As there is no active cooling capability, finer control with a proportional relay, at about \$180 per channel, was deemed unnecessary. With the current implementation, temperatures at all stations can be maintained to within about 3°C of the set point.

The program can run in manual mode with open- or closed-loop control. It can run in automatic mode with preset cycles for the controlled elements. The program is also set up to allow for on-line adjustment of the controller parameters.

Some effort has been directed toward porting the software to Visual Basic under Windows95 environment. New device drivers and low-level routine for the data translation boards need to be purchased in order to implement the software under version 5 Visual Basic.

### 3.2.1 Modeling Reaction Kinetics of Resin Systems with a Crystalline Phase

A general approach to dealing with the dissolution/melting of the crystalline phase in resins systems such as PR500 is being studied. Modeling the kinetics of these resin systems is difficult because of the overlapping endotherm and exotherm; the former is due to the dissolution and melting of the crystalline phase and the latter, chemical reaction. The crystalline phase can go into solution and react at temperatures below its melting point. At this stage the overall process can be either reaction controlled or dissolution-rate controlled, depending on the temperature. At around the melting point, the crystalline phase may dissolve faster, but the reaction rate may be limited. On the other hand, if the reaction is fast, then the process may be diffusion controlled. From constant temperature rate DSC scans, it is possible to deconvolute the endotherm and the exotherm. The reaction portion can then be modeled either by Arrhenius type model or by neural network. The endotherm can be modeled by neural network but may work only for similar constant temperature rate scans. Resin reaction rate and advancement under prolonged isothermal conditions below the melting point of the crystalline phase, which is what the resin system will typically experience, may not be predicted accurately.

### **3.3 Composite Manufacturing Concepts for Reduced Cost**

#### **3.3.1 Material Characterizations**

A new technique of fiber preform permeability measurement for aerospace applications has been developed. A 3D experimental system for fiber preform permeability measurement has been set up in-house. This gives MLBC the necessary implement in process developments and composite quality and cost control.

Generally speaking, a composite consists of two materials – resin and fiber. The process of resin wetting or infiltrating a fiber preform plays a key role in improving composite quality and reducing manufacturing costs for liquid composite molding, pultrusion, filament winding and autoclave. This process depends mainly on two parameters: resin viscosity and fiber tow or preform permeability. Experimental methods are the only way to determine the two parameters. Resin viscosity can be easily measured. However, only a few laboratories have the capability of measuring fiber preform permeability. In addition, current techniques of permeability measurement will result in large errors for aerospace applications. In aerospace applications for polymer composites, there are two major differences from other fields in composite applications: (1) fiber preforms are often made with anisotropic continuous high modulus carbon fiber, and (2) high fiber content. These will result in high capillary pressure and racetracking during permeability measurement with current techniques. A new technique has been developed for permeability measurement of fiber preforms in aerospace applications. Compared with the current technique, the new technique has the following advantages for fiber preform permeability measurement: better accuracy, easy operation, and ability to measure gas permeability in carbon foams or ceramic matrix composites (CMC). The permeability of



fiber preform is the parameter necessary in process analysis and evaluation and composite quality and manufacturing cost controls. Several fiber mats, which are often used in aerospace applications, were measured. The permeabilities of P4 chopped-glass fiber preforms and P4A chopped-carbon fiber preforms were also measured. The permeability data were used in mold and process design for the P4A program.

### 3.3.2 Modeling Manufacturing Composite Processes

A 3D flow model system has been set up to simulate and analyze the manufacturing composite processes such as resin transfer molding (RTM), structural reaction injection molding (SRIM), vacuum bag molding, SCRIMP and injection/compression molding. Using these models, resin pressure, velocity, temperature, cure degree distributions and flow front locations can be predicted during mold filling and curing. This greatly reduces manufacturing costs and improves composite quality.

The autoclave process can be used to make high-quality composites. However, the manufacturing cost is high because of the high tool cost. On the other hand, spray up and hand lay-up can be used to make low-cost composites. However, the composite quality is also low. Liquid composite molding (LCM) such as RTM, SRIM, vacuum bag molding, SCRIMP and injection/compression molding can be used to make high-quality composites at medium costs. To develop LCM, the first step is to set up an efficient flow modeling system for mold and process designs, process analysis and evaluation.

In LCM, mold and processes designs are the key issues in successfully fabricating composites, controlling composite quality and cost. The LCM process is quite complex because it combines mass and momentum balance, heat transfer and chemical reaction. Engineers have, however, traditionally worked with trial and error methods. They

carry out the mold and process design according to their past experiences, and then test the designs by physically casting a mold. If defects occur in composites such as dry spots, high void content, low degree of cure, etc. the engineers would modify the designs and repeat the test. When the shape of a composite is simple, only a few tests are needed to reach an acceptable design. When the shape of the composite parts becomes complex and the size becomes larger, however, the test must be repeated many times. Considerable test expenses and time increase manufacturing costs and obstruct the widespread use of composites. Computer-aided design and computer-aided manufacturing (CAD/CAM), with its ability to simulate mold filling and curing, would be the best way to solve this problem. A 3D flow model system has been set up to simulate and analyze the manufacturing composite processes such as RTM, SRIM, vacuum bag molding, SCRIMP and injection/compression molding. This system has been used to simulate a CAI part and to add the mold design of a part for P4A.

### 3.3.3 Low-Cost Resin Infusion Processing

Historically, the vast majority of aerospace composite parts have been fabricated through hand lay-ups of prepregs followed by autoclave consolidation and cure. Recent efforts to reduce the cost of composite parts have led to a number of research initiatives. One initiative is the use of braided, woven, or sprayed dry preforms which utilize machines rather than humans to achieve the proper fiber orientations. This approach reduces both touch labor and raw material costs. A variety of techniques have been developed to infiltrate this dry preform with resin to make the final part. Among these are RTM, SCRIMP, and RFI.

Our desire is to develop a low-cost process which can be used to manufacture quality, high fiber volume parts ranging from production units of one to several thousand. The process should ideally require only low-cost or *in situ* tooling (foam core), minimize raw material waste, touch labor, and consolidation pressures (outside autoclave) and be highly reliable (large integrated preforms will represent substantial investment because of their size). The SCRIMP process seems best suited to meeting these goals; however it must be adapted for conventional aerospace preforms and resins. The unique approach UDRI has chosen to develop, for dry preform resin infusion, has been termed pressure-assisted vacuum bag resin infusion (PAVBRI).

Hardware development for the PAVBRI control system has been completed. The system can accommodate 20 thermocouples, 30 dc-resistance sensors, 10 auxiliary sensors, 12 heater zones, 12 gate valves, and one peristaltic pump. The current software is configured to control based on manual set-points but will be modified for semiautonomous control in the future. Low-cost, tool-mounted dc-resistance sensors have been shown to work as long as the resin's ionic viscosity is not too high or if a conductive preform such as carbon fiber is used.

Of critical importance to the success of vacuum bag processing is the ability to obtain high fiber volumes in excess of 55 percent. Work reported last year [49] on the compressibility of various fabric constructions showed that none of the 10 fabric styles commonly used within MLBC could be compressed to a suitable fiber volume using vacuum pressure (14.7 psi) alone. In fact even when the fabric is compressed under the vacuum bag, it was shown to "spring back" when the preform was infused with resin. For this and other reasons, an effort was spent to investigate the use of binders to preconsolidate preforms.

While many binders exist in solid-powder form, an effort was made to find a very low viscosity binder which could be used to penetrate throughout a preform and cure with sufficient mechanical strength to hold the preform to its net shape. Ciba-Geigy offers a line of water soluble epoxy resins which can be diluted to very low concentrations, thus offering low viscosity and precise control of binder content. The binder selected was Araldite ECN 1400/HZ340, which is an epoxy cresol novolac resin. Numerous experimental trials showed that the best process for applying binder and compacting the fabric preforms was to saturate the preform with a 10 percent solution of the water/binder mixture then boil-off the water while compacting the preform to the desired thickness. This process typically took 10-20 minutes in a preheated press.

Following successful consolidation of fabric preforms, the PAVBRI process was utilized to conduct infusion studies. Initially trials were conducted with a model resin system, corn syrup, to refine the process. The model resin was chosen because it provides: low cost, easy cleanup, visual inspection of flow front, low ionic viscosity, and low viscosity at room temperature. After several modifications to plumbing and bagging techniques, infusions were conducted with 3M's PR500 epoxy resin. This resin must be infused at 177°C, therefore the PAVBRI heater controllers were evaluated in addition to the dc-resistance-based flow sensors. C-scans taken of cured PR500 composites showed that it is possible to fabricate aerospace-quality composites using sophisticated vacuum-bagged infusion methods.

Future work in this area will concentrate on the integration and validation of Ken Han's three-dimensional flow model into the process controller.

## 4. CARBON-CARBON AND CARBONACEOUS MATERIALS

### 4.1 Economical Carbon-Carbon

#### 4.1.1 New Precursors for C-C

##### 4.1.1.1 *Carbonization/Graphitization of Pitch and Other C-C Precursors*

Twenty-two carbonization runs were made during the past year.

The materials include pitch powders, pitch foams, various pitch fibers, pitch powder with encapsulated oxidant, and various phenolic composites. Twenty graphitization runs were made to various temperatures above 1200°C. The materials include pitch foams, pitch fibers, and various pitch powders and plaques.

##### 4.1.1.2 *Characterization of University of Akron Carbon Fibers*

Pitch-based carbon fibers were obtained from the University of Akron, oxygen stabilized, and carbonized. Some of these fibers were graphitized. The mechanical testing of these fibers proved to be difficult because of their entanglements and small diameters.

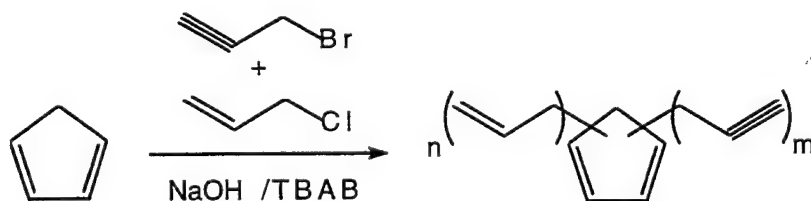
##### 4.1.1.3 *Evaluation of a Class of New High Char Yield Resins*

Attempts were made to make composites using a series of resins based on allyl- and propargyl-substituted cyclopentadiene (APcP). The four resins that were synthesized and examined in this study contained substitutions of 100 percent allyl-, 3:1 allyl- and propargyl-, 1:1 allyl- and propargyl-, and 100 percent propargyl groups. Prepregs of the APcP resins with fibers was only partially successful due to their very low viscosity and lack of tack. The low viscosity and tack, which were originally believed to be a result of using the polymer precursors, were found instead to be due to unreacted starting materials

and solvent impurities. Removal of these materials was not a trivial problem and resulted in a resin system too viscous to prepreg. Oxygen sensitivity, especially at elevated temperatures, is another problem to prepregging with these resin systems.

The class of polymers examined here is based on propargyl-substituted cyclopentadiene. This resin is composed of up to 95 percent carbon by weight and has the potential of producing a very high-char yield composite. TGA measurements showed up to 95 percent char yield in the composites and over 80 percent in neat resin samples [50]. This earlier study used hand laid-up composites which suffered from a large amount of voids in the as-cured state. The increase in carbonized matrix density and charring inevitably resulted in an increase in the original void content. The highest char yields and lowest increase in void content occur in the more highly propargyl-substituted resins.

Mixed allyl-/propargyl-cyclopentadiene polymers form the family of high-char yield resins examined as potential matrices for carbon-carbon composites. The resins are synthesized using a five-membered unsaturated ring base, an unsaturated organic halide, and a phase change catalyst (tetrabutylammonia bromide in a basic environment (50 percent NaOH) [49,51,52]:



where  $n + m = 2$  to  $6$  of the allyl and propargyl groups add to the ring. The unsaturated additions thermally decompose to form free radicals that can add to other triple or double bonds producing a crosslinked polymer network. Some polymerization begins during the

original synthesis, but if kept free of oxygen, the resin remains as a low-viscosity fluid for an extended time at room temperature.

The preregs prepared from the synthesized resins had very little tack and were very difficult to handle. The amount of tack in the preregs decreased as the fraction of propargyl groups increased. In the 1:1 and 100 percent propargyl resins, the tack was insufficient to hold the preregs together. This plus the unexpected loss of volatiles during prepregging was the first indication of difficulty in these resins. The loss of volatiles was also seen as a potential health problem with these resin systems. The synthesis and prepreg problems were discussed in a previous annual report [49]; the current work was the subject of a SAMPE paper and presentation [53].

Differential scanning calorimetry (DSC) on the resin was used to determine the heat of reaction of the system and the temperatures at which the reactions take place (see Figure 38). This test was quite successful. Thermal gravimetric analysis (TGA) was performed to determine the amount of weight loss as the sample is subjected to a thermal cycle. This will indicate any loss during cure as well as the loss during the subsequent carbonization. The results of the TGA were the next indication of problems. The samples continued to lose weight until there was no material left (see Figure 39). Likewise the Rheometrics test was unsuccessful because the resin drained out or evaporated from between the plates before any cure could take place.

With no good cure data, and preregs that could not be handled, the original plan to fabricate and test composite panels was abandoned. Attempts were made to remove remaining volatile materials from the preregs by heating to 100°C under vacuum. Only slight improvements in tack and handling were observed. The complete

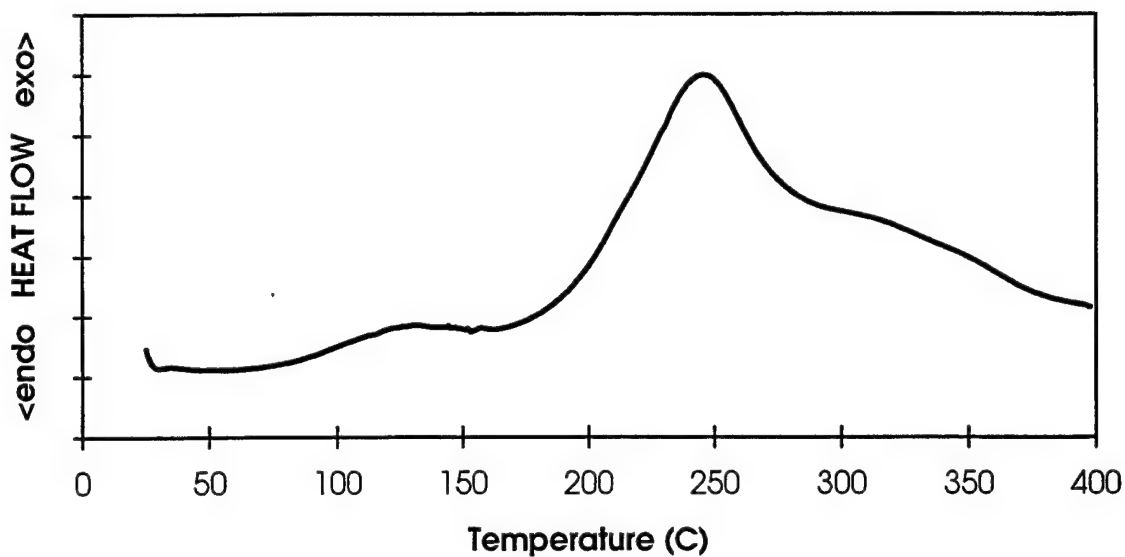


Figure 38. DSC Curve for 3:1 APcP Resin.

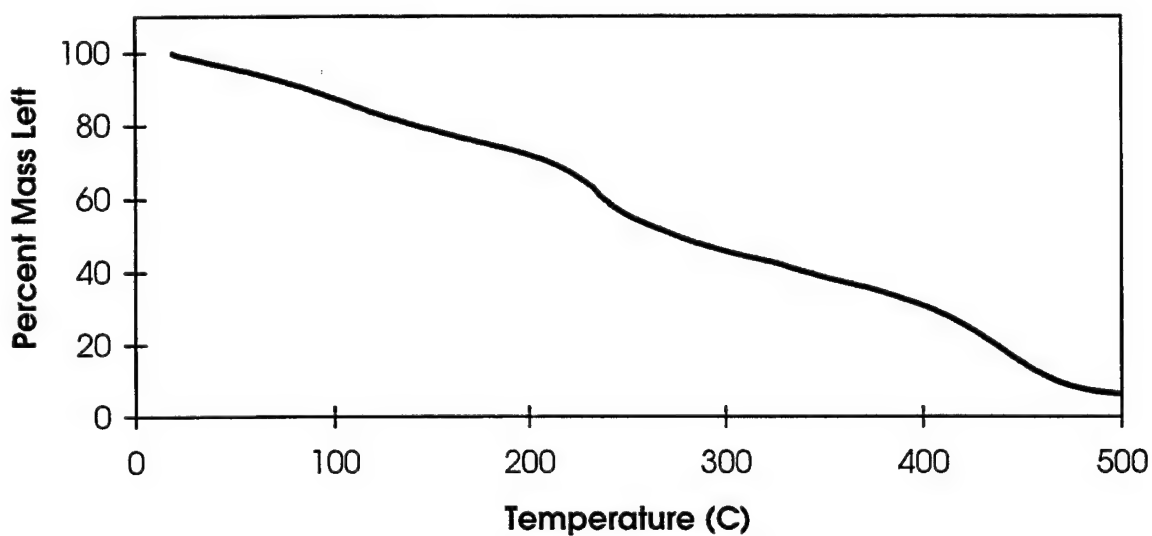


Figure 39. Typical TGA Curve for APcP Resins.

loss of resin during TGA was again confirmed. The remaining resin was then analyzed by FTIR to determine its composition.

The results of the FTIR confirmed the presence of both unreacted organic halides in all the resins and toluene in the batches with propargyl groups.



The propargyl bromide is sold with a small amount of toluene diluent to stabilize it. The problems of tack and handleability were then taken as a symptom of these low molecular weight contaminants.

FTIR scans of allyl-chloride and propargyl-bromide are shown in Figure 40. Table 6 lists the annotated bands in the figures and their chemical source. These bands were used to monitor the resins in subsequent purification steps. The purification consisted of several vacuum distillations.

Figure 41 shows part of the FTIR scans of AcP resin before and after purification. The distinctive C-Cl band at  $750\text{--}730\text{ cm}^{-1}$  completely disappears indicating the loss of this species. The C=C band at  $3070\text{ cm}^{-1}$  remains relatively unchanged. As a result of this distillation purification, the AcP resin became very thick, almost pastelike.

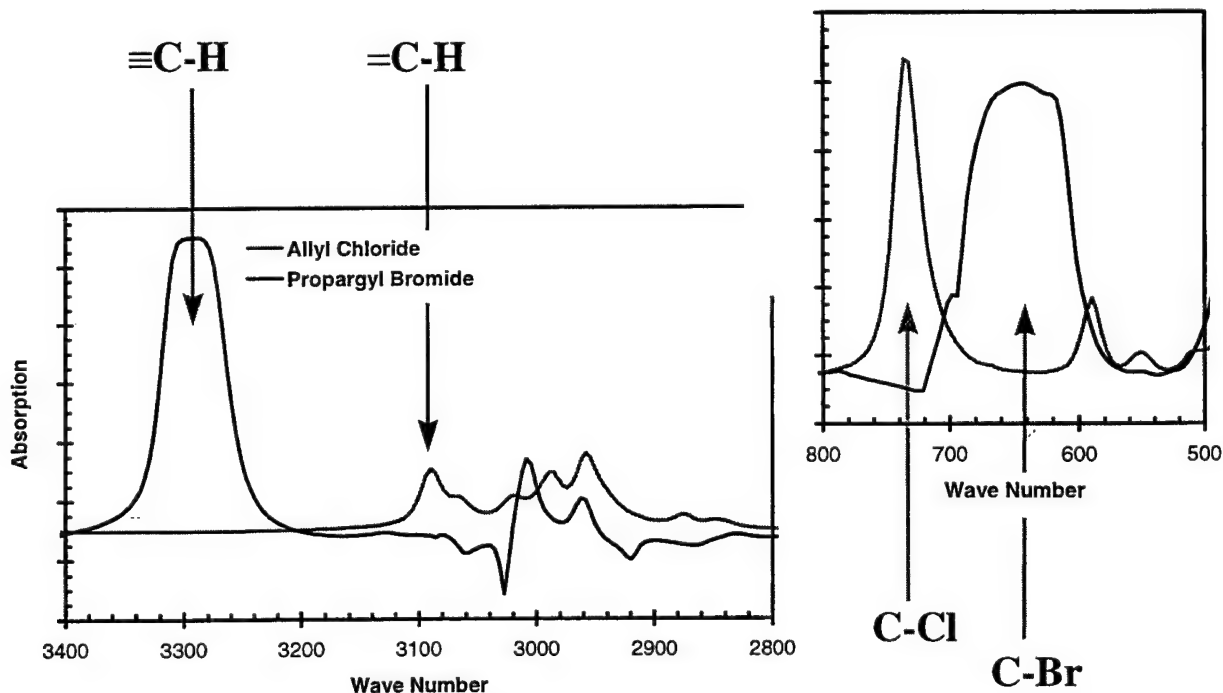
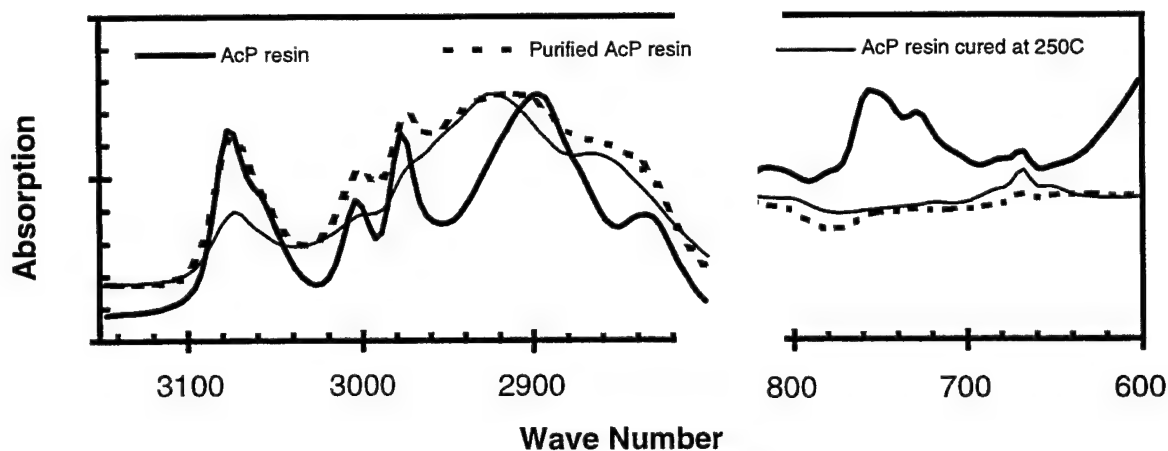


Figure 40. FTIR of Allyl-Chloride and Propargyl-Bromide.

**TABLE 6**  
**FTIR Bands of Allyl-Chloride and Propargyl-Bromide**

Allyl-Chloride		Propargyl-Bromide	
location (cm <sup>-1</sup> )	chemical species	location (cm <sup>-1</sup> )	chemical species
3070	C-H stretch on C=C	3300	C-H stretch on C≡C
1640	C=C	2110	C≡C
730-750	C-Cl	600-650	C-Br



**Figure 41. FTIR Scans of AcP Resin Before and After Distillation and After Partial Cure.**

Also shown in this figure is partially cured AcP resin which shows a decrease of the 3070 cm<sup>-1</sup> band. When cured to 350°C this band completely disappears, as the double bonds in the resin thermally open up to crosslink the material.

The resins containing propargyl groups all showed some residual C-Br band at 600-650 cm<sup>-1</sup> after vacuum distillation. This band did not completely disappear until the resins were cured at 250°C. It apparently takes this elevated temperature to completely drive off this unreacted starting material. Figure 42 shows part of the FTIR scans of PcP resins as a function of cure. The propargyl C-H band at 3300 cm<sup>-1</sup> is clearly

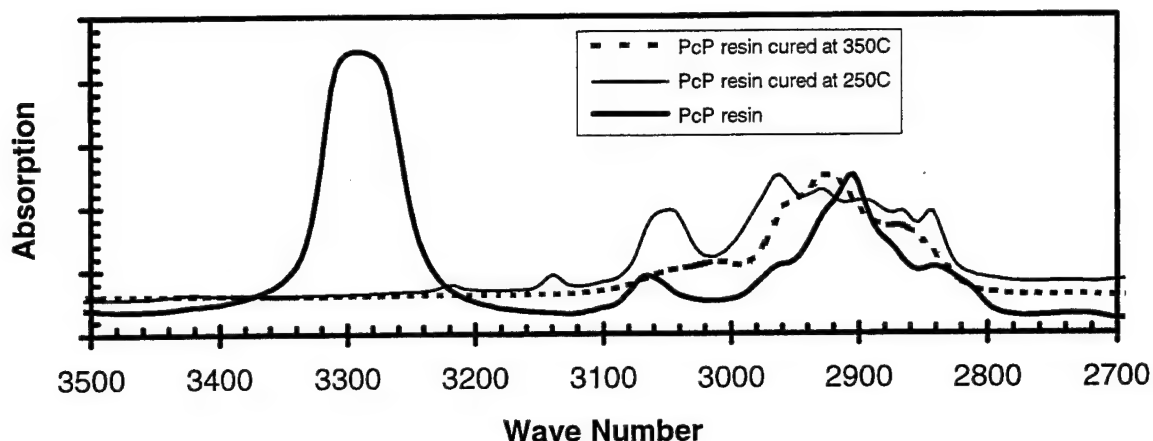


**Figure 42. FTIR Scans of PcP Resins as a Function of Cure State.**

visible in the resin. The propargyl triple bond opens up on heating to form the polymer and leaving a double bond. Subsequent heating will open up the double bond to completely crosslink the polymer. This can be seen in Figure 42 as the C-H from C=C at 3050-3070  $\text{cm}^{-1}$  increases from the resin to the partially cured resin before completely disappearing in the fully cured system.

The resins cured in Figure 42 were handled carefully to exclude oxygen during the heating process. Other resin samples were cured without the same care and showed signs of severe exotherms. The exotherm problem was also observed when the PcP resin was cured without the distillation purification process.

Vacuum distillation can be used to remove most but not all of the starting materials, particularly in the more highly propargyl-substituted resins. The resin must also be kept from exposure to oxygen before curing. Then the possible extreme exotherms observed several times in our laboratories can be avoided. FTIR was shown to be a useful evaluator to follow the removal of unreacted starting materials. FTIR can also be used to qualitatively follow resin cure as well. The class of resins made from allyl- and

propargyl-substituted cyclopentadiene is not the simple, low-viscosity, easy-to-cure material which was originally believed.

#### 4.1.2 New Processes for C-C

##### 4.1.2.1 *Intelligent Processing of Carbon-Carbon*

The primary purpose of this effort is to understand the steps involved in pitch processing. During processing, gases are produced that need to be monitored to determine what types of materials are produced and if they are consistent from cycle to cycle. Also the process parameters could be controlled to prevent certain materials from being released or encourage unwanted materials to leave so as to improve the final product. The initial approach is to use controlled experiments in the Cahn TGA coupled with a Hewlett-Packard GC/MS. Considerable effort has been expended to develop a high-temperature transfer line to connect the two pieces of equipment. The transfer line has been completed and initial testing has been performed. During initial testing the mass spectrometer vacuum system failed and is being repaired. The Cahn TGA has had numerous controller and power problems during the period. Most of the initial problems have been repaired, and testing should begin in the near future.

##### 4.1.2.2 *Stabilization of Pitch*

Several samples of the CONOCO pitch were stabilized in an air oven at 160°C. These included the "soft" and "hard" bicomponent pitches obtained by Heather Anderson, a 285°C softening point (SP) pitch from Kristen Kearns, and a 285°C softening point pitch from Oak Ridge National Laboratories (ORNL). The mass losses and gains over time were recorded; examples of the extremes in mass change, bicomponent pitch obtained from ORNL and the softest pitch (SP = 241°C) are shown in Figures 43 and 44.

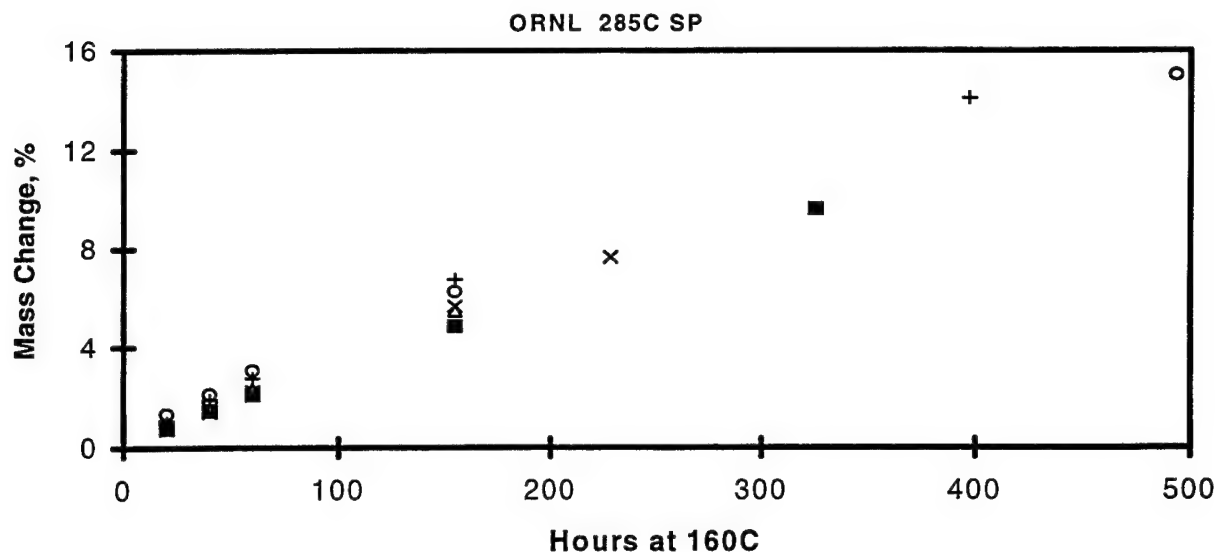


Figure 43. Mass Change versus Time for a High Melting (285°C) Bicomponent Pitch.

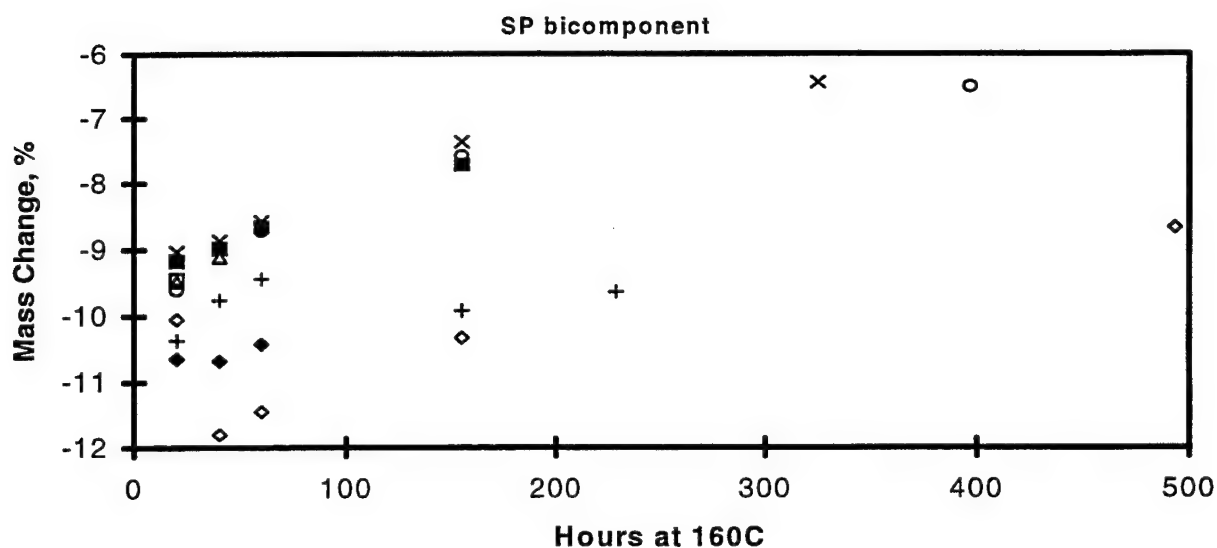


Figure 44. Mass Change versus Time for a Low Melting (241°C) Bicomponent Pitch.

The mass loss of the higher SP pitches was less than the lower SP pitches; in fact the highest SP pitch only gained mass.

The oxidized pitch samples were pressed into pellets and carbonized. In the lower melting pitch, very little stabilization time was required (20 hours) to eliminate bloating, even though only weight losses (9-12 percent) were observed. The

higher softening point materials only gained weight but required 3-7 days stabilization to significantly reduce bloating.

Straight-line fitting of the mass change with time produced fits that were as good as fits against the square root of time (Fickian diffusion). This would indicate that simple diffusion is not the governing factor in these systems. In the softest materials, the loss of volatiles apparently governs the materials ability to resist bloating during carbonization. In the higher melting materials, the pitch follows a more conventional route to oxygen stabilization.

#### 4.1.2.3 *Carbon-Carbon Heat Exchangers*

Assistance was required to characterize materials from a contractual effort to make carbon-carbon heat exchangers (HXR) for aircraft applications. Sparta is the main contractor for the heat exchangers, with BFGoodrich the main maker of the carbon-carbon. The HXR design consists of carbon-carbon panels or parting sheets and fins attached to each other which are then assembled into a multilayer design of many parting sheets and fins. The fins are made of single-layer woven carbon-carbon sheets which are folded back and forth. The ends of the folds are attached to the flat parting sheets of two-ply carbon-carbon. A schematic of this arrangement is shown in Figure 45.

There are two basic designs: conventional, where the fins and parting sheets are made separately and then brazed together; and integral, where the fins and parting sheets are assembled and carbonized as a single unit. The conventional design is built up into the final configuration by successively brazing fins to parting sheets and stacking the layers to the desired number of layers and orientations. The integral design takes the layers

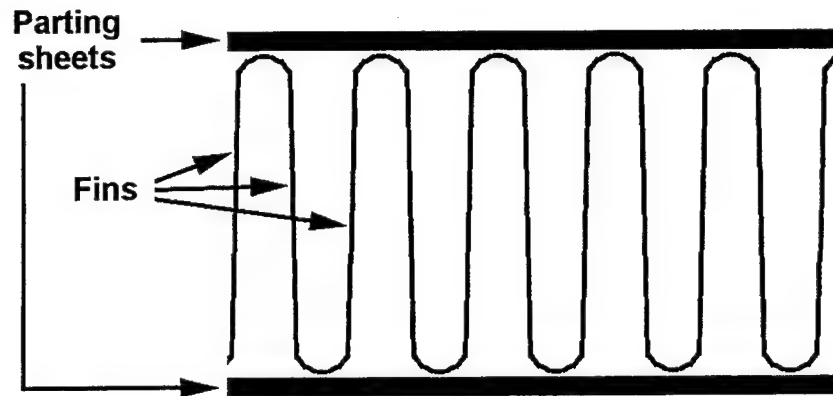


**Figure 45. Schematic of the Carbon-Carbon Heat Exchanger Design.**

of fins and parting sheets and brazes the parting sheet of one layer to the next layer's parting sheet.

The initial problem examined was in the conventional design which was found to have many broken brazed joints of the fins to the parting sheets. This occurred in samples with just one parting sheet and two fin layers and in samples of one fin layer and two parting sheets. The problem was found to have two probable causes: (1) the fin heights were not consistent and (2) the CVI/CVD carbon layer was too thick.

The first cause was visually apparent but confirmed by measuring the distance from fin peak to fin valley of several assemblies. The heights were found to vary by up to six percent. This represents a distance of over 0.5 mm for the fins of 8.6 mm. Since the highest fins will be the ones in contact with the parting sheets and the braze thickness was less than 0.1 mm, many of the fins will not attach to the parting sheets. Production was reportedly adjusted to correct this problem.

The second cause was identified using polarized light microscopy. When crossed polarized light is used to observe samples, the contrast or brightness variations are caused by several mechanisms. The general reflectivity of the

material will produce lighter areas, and material with anisotropic indices of refraction or birefringence will also appear lighter in certain orientations. By combining ordinary crossed polarized light (CP) and CP with a wave plate (or red plate) and by rotating the samples, much information can be extracted. Much of this information requires color images which cannot be reproduced in this report. The information obtained is annotated in Figure 46 but could not have been discerned from this gray-scale image.

The braze material was found to be of higher reflectivity than the carbon as expected. In CP light this appeared lighter than most of the surrounding materials and was quite bright with a wave plate. The anisotropic regions are bright in CP except when the direction of one of the indices of refraction is parallel to one of the polarizer directions. With a wave plate, the anisotropic material appears red when the direction of one of the indices of refraction is parallel to one of the polarizer directions, yellow when the highest index of refraction direction is parallel to the highest index of refraction direction of the wave plate (slow directions said to be adding), and blue when the highest index of

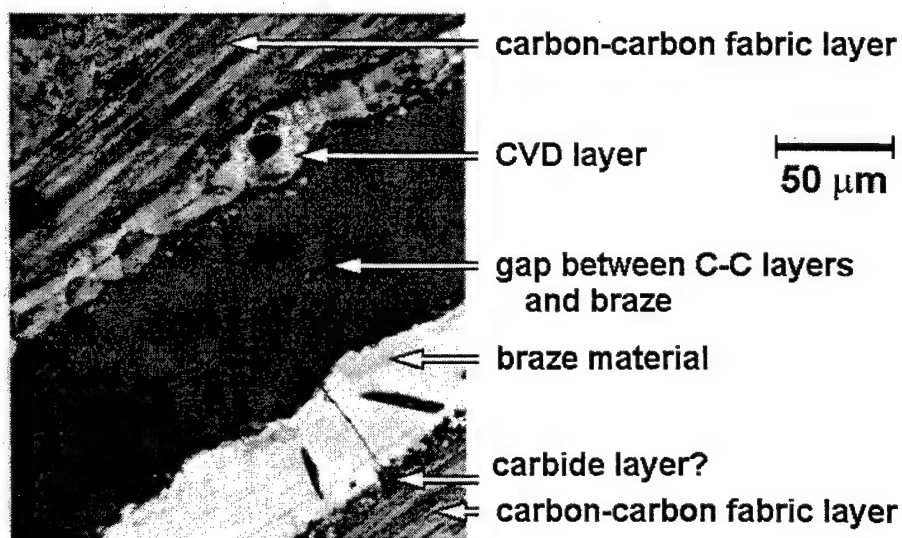


**Figure 46. Optical Micrograph (Crossed Polarized Light with a Wave Plate Converted to a Gray-Scale Image) of the Conventional C-C Parting Sheet/Fin Heat Exchanger.**



refraction direction is perpendicular to the highest index of refraction direction of the wave plate (slow directions said to be subtracting). By rotating the sample under CP with a wave plate, the anisotropic regions change in color from red to yellow to red to blue.

In this way the regions in Figure 46 were identified. The fibers in the carbon-carbon are well known to be anisotropic and can be observed both when lying in or perpendicular to the observation plane. A thicker layer on the outside of the C-C was also anisotropic which is typical of a CVD layer. The gap between materials was dark in the original samples, typical of potting resin (subsequent samples potted in-house were green from the fluorescent dye). The bright region which did not change from its pale pink color on rotation was the braze material. There was also a dark region between the braze and C-C; this is probably a carbide region where the metal has reacted with the carbon.

The CVD layer was found to either not react with the metal or to form a thick carbide layer. Both of these are bad for good adhesion between the C-C and braze. Because the graphene layers of the CVD lay flat on its surface and are difficult to react in that orientation, there is no adhesion until the reaction is forced. Once the reaction occurs there is generally too much reaction which results in a brittle carbide region too thick to accommodate thermal stresses between the materials.

Later assemblies had their CVD layers sanded off or partially removed before brazing. This resulted in thinner carbide layers but did not affect the fin height problem.

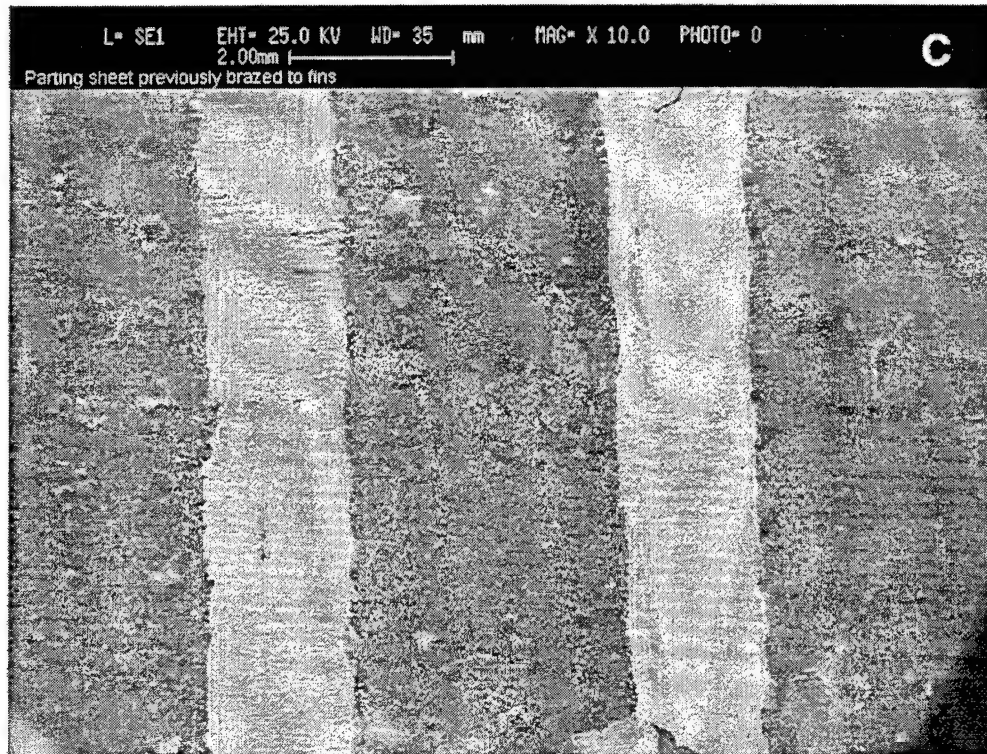
The next problem examined was the separation of the fins and parting sheets at the braze joint. The question was whether the braze parted or if cohesive

failure in the C-C composite occurred. This was examined by SEM. "Normal" SEM images are formed from secondary electrons scattering after the main electron beam rasters across the sample. Brightness is dependent on material conductivity, etc., and shadows can result when the detector is shielded from the electrons by part of the sample. "Backscatter" images show the average atomic number of regions: lighter regions have a higher average atomic number than darker regions. Figure 47 shows typical images from the separated parting sheet.

What can be seen from the normal and backscatter images in Figure 47 is that the braze material tends to concentrate near the fin bond areas and in the weave interlace areas. At higher magnifications (Figure 48), one can see that there is some fiber breakage between the fin and parting sheet regions, although much of the failure is in the braze itself. The region of the parting sheet exactly corresponds to the same region as the fin area; this was confirmed by locating a specific feature on one surface and then finding the corresponding feature on the other. Backscatter images demonstrated that the rough areas of Figure 48 are braze material with imprints of the fiber composite visible at certain magnifications.

The next question was how good of a braze joint is formed between parting sheets. This was examined with two integral construction fin/parting sheet structures. A backscatter image of this combination is shown in Figure 49.

The braze material did not bond across the entire parting sheet. Apparently only when the high points of the parting sheets were in contact did the parting sheets braze together. The SEM and optical images were used to estimate 5-10 percent of the parting sheets' surfaces were brazed together. The braze material did not infiltrate the pores



(above) SEM image  
(below) Backscatter image  
(light areas contain brazing metal)

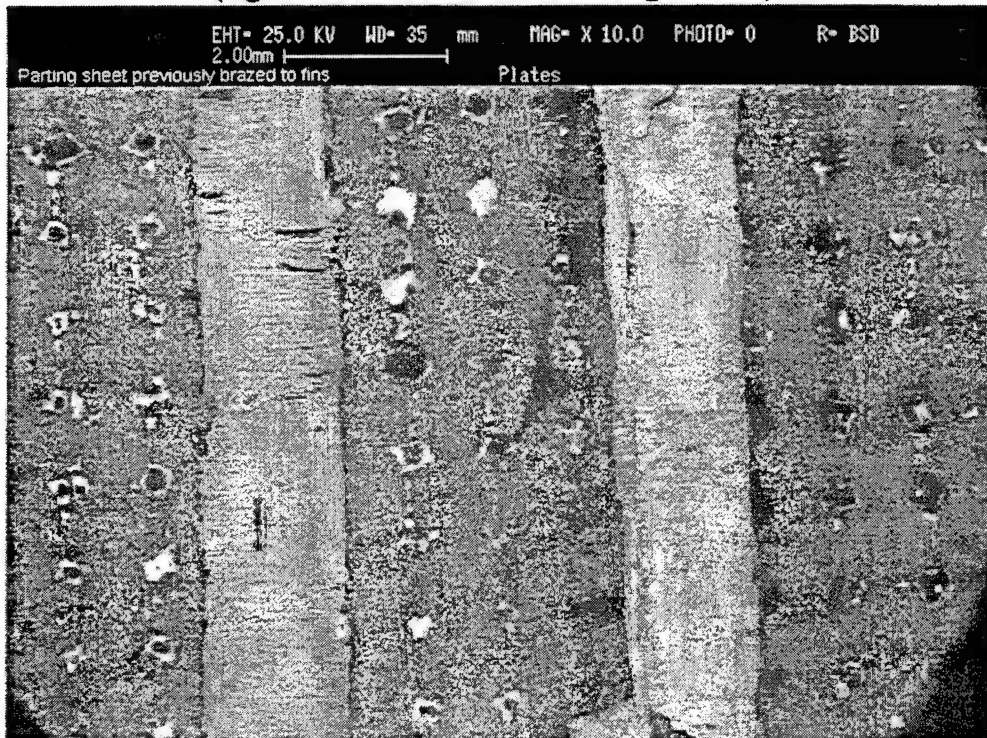
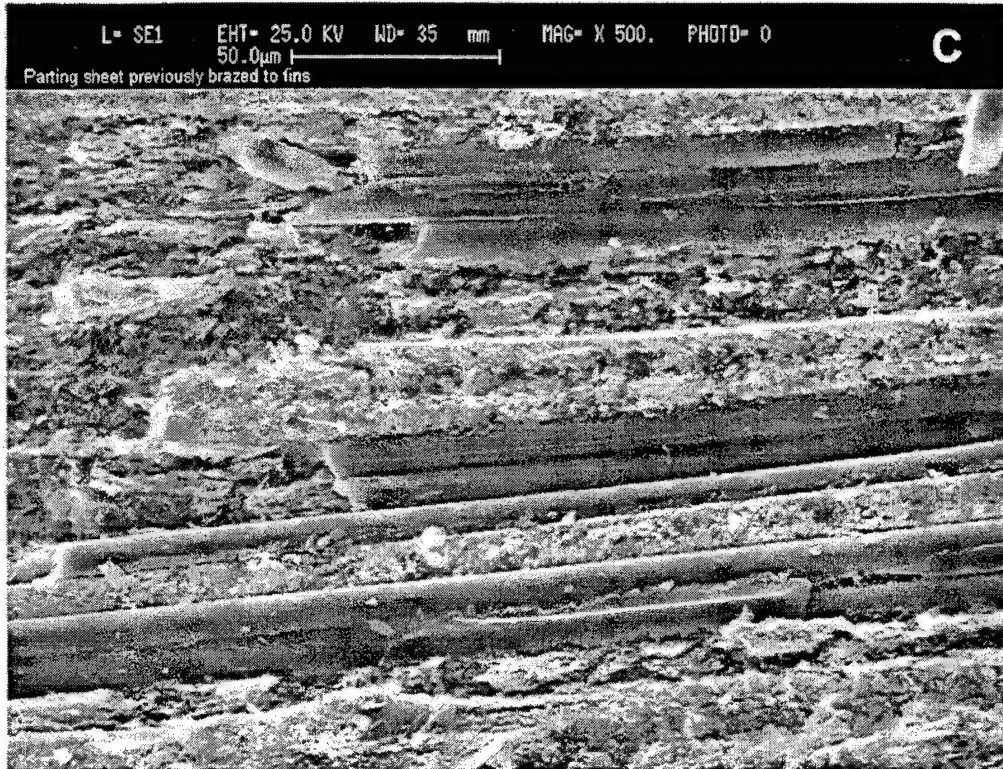
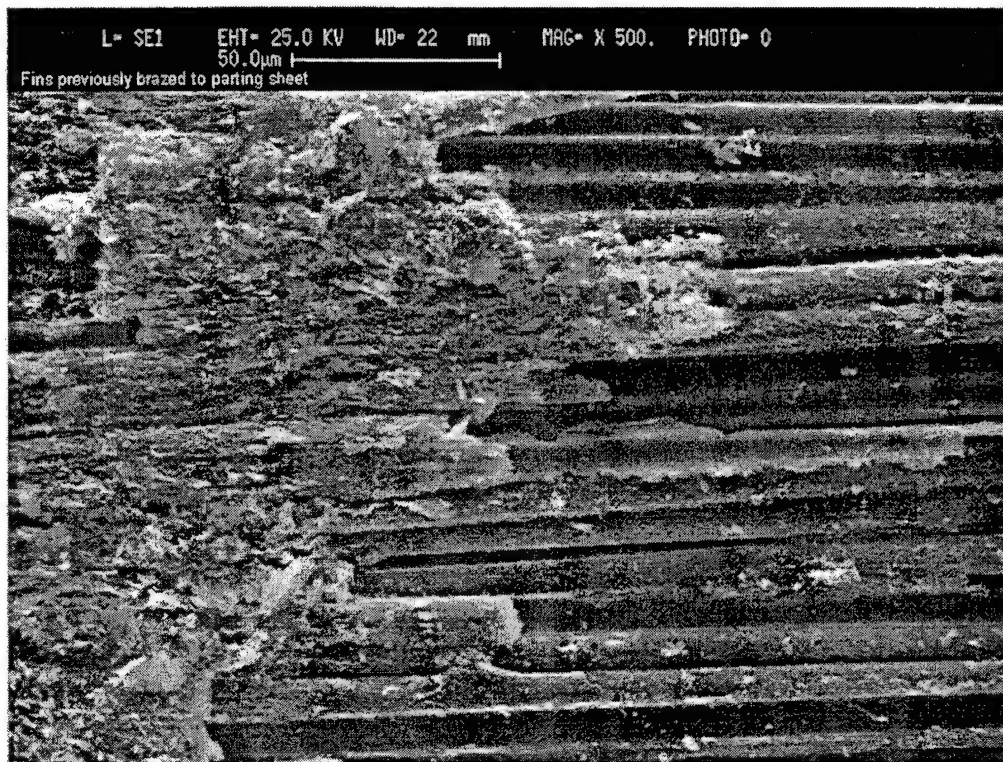


Figure 47. Typical SEM and Backscatter Image of the C-C Parting Sheet Separated from the Brazed Fins.



**Parting sheet above and corresponding  
Fin region below**



**Figure 48. SEM of Separated Parting Sheet and Fin.**



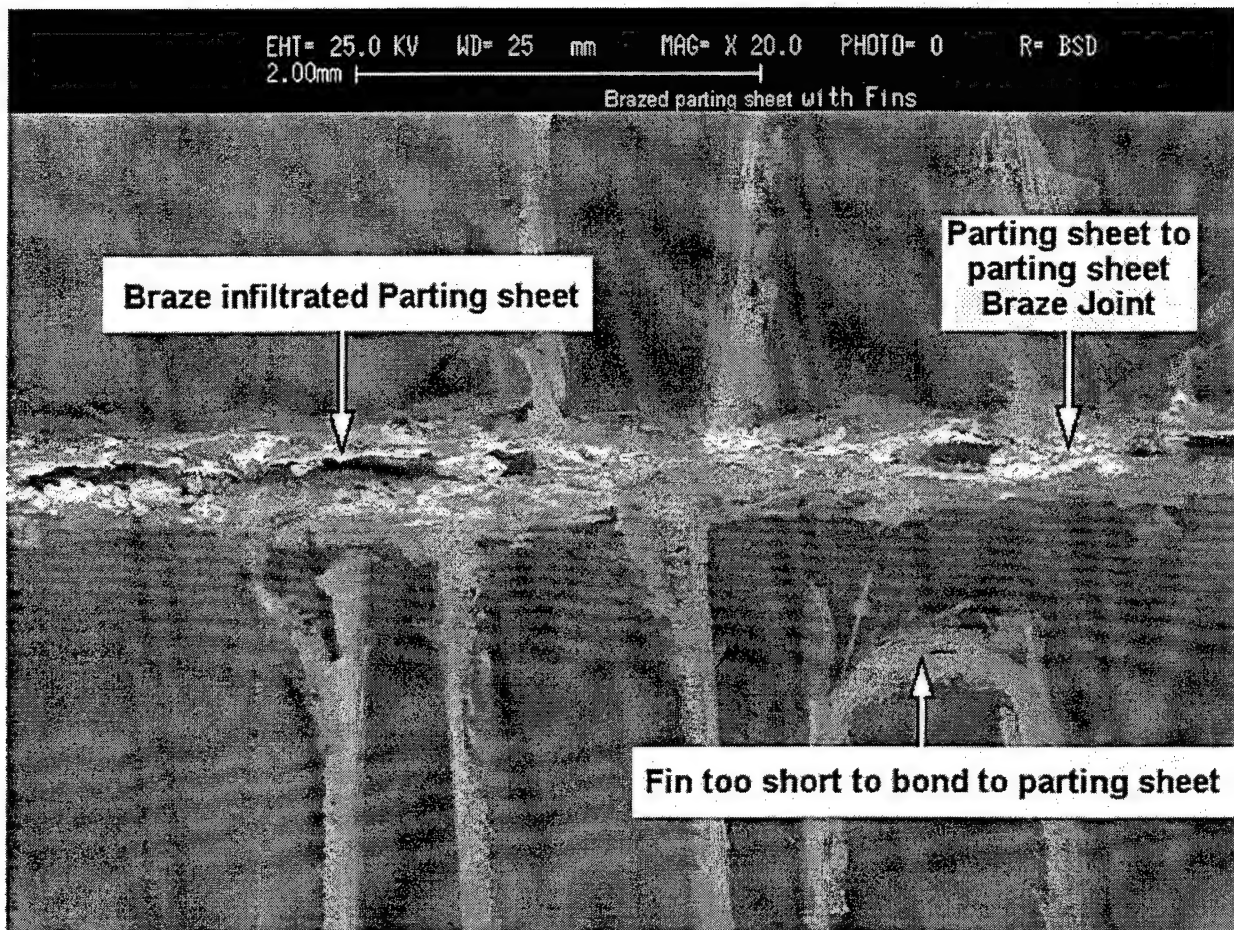


**Figure 49. Backscatter SEM Image of Two Integral Construction Parting Sheet and Fins Brazed Together by their Parting Sheets.**

of the parting sheets, which means that a good mechanical bond was formed. Also visible in this figure is the fin height problem.

The last question addressed in this study to date was how much if any phase separation occurs in the braze itself. Figure 50 shows two parting sheets brazed together with a significant amount of braze material visible.

Various regions in the braze material were visible by differences in reflectivity in the optical microscope. Electron dispersive x-ray spectroscopy (EDS) was used to measure the elemental content of these regions in the SEM. EDS

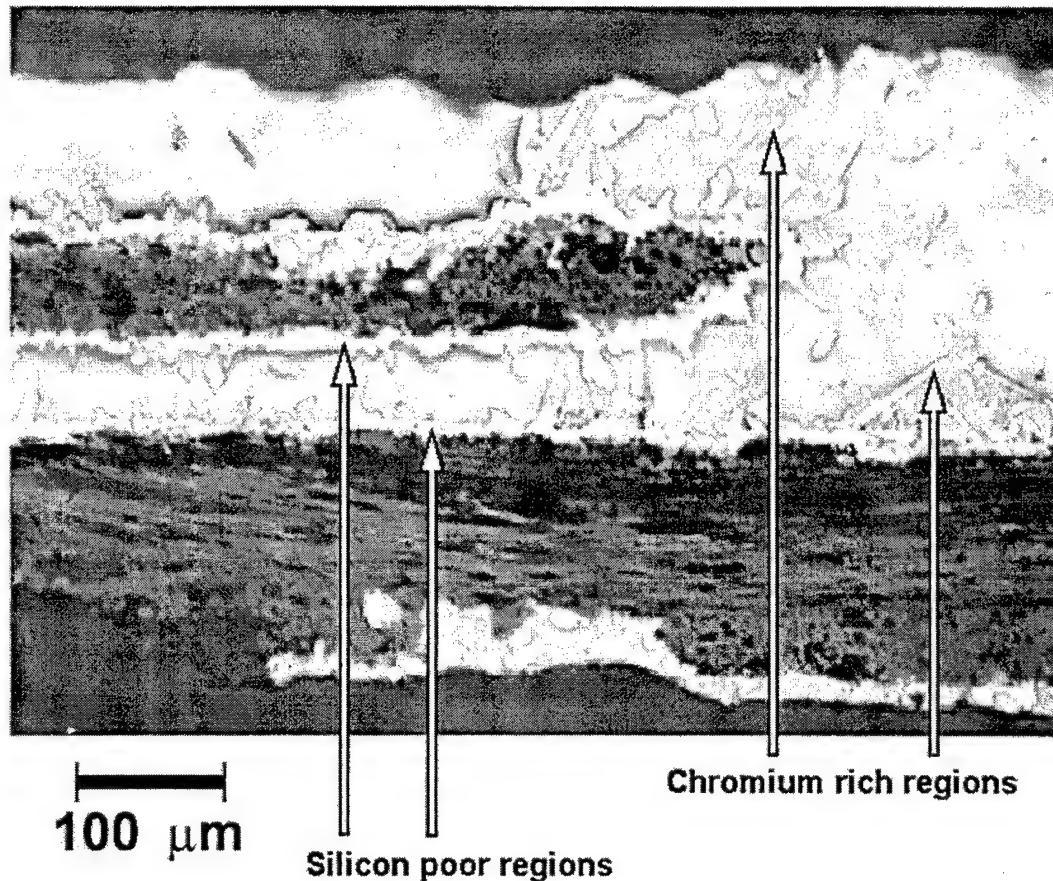


**Figure 50. Optical Micrograph of C-C Parting Sheets Brazed Together.**

measures x-ray energies generated by the electrons hitting atoms; energies characteristic of each element compared to measured values to indicate what elements are present. The regions near free surfaces and the carbon composite were found to be silicon-poor relative to the bulk braze. There were also regions containing mostly chromium. This phase separation was expected by surface energy considerations and was not considered a problem.

Computer tomography (CT) scans of the C-C parting sheets and fins were compared to the micrographs taken of these materials. The resolution was not as great as with microscopy [either optical or scanning electron microscopy (SEM)], but this technique has the great advantage of being nondestructive. The fin height and parting sheet bonding problems were clearly visible. Figure 51 shows the cross section. The original CT

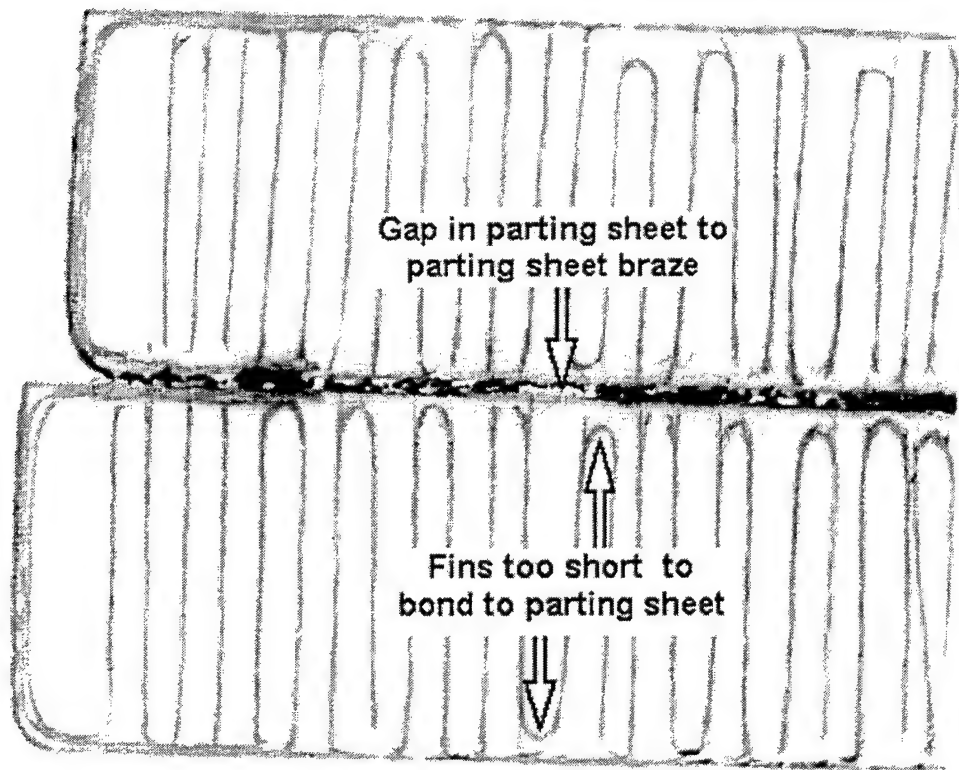


**Figure 51. CT Cross Section of C-C Heat-Exchanger (Color Removed and Contrast Inverted).**

scan was dark where only air is present (white in Figure 51) going to red on the C-C composite (gray in the figure), and bright yellow for braze material (black areas in Figure 51). It is still not clear if small defects will be visible in the CT or if those defects would present any real problems.

#### 4.1.2.4 *Water-Based Suspension Prepregging of Pitch Powder*

The production of unidirectional carbon-carbon composites from oxidized pitch powder prepregs continued from last year. Great difficulty was encountered in achieving uniform distribution of powder within the fiber tows during the water-based suspension prepreg process. Many variations on the vertical die arrangement were attempted, but finally a horizontal bath was shown to perform much better, utilizing

lower viscosity suspensions and resulting in good distributions of powder within the fiber tows.

#### 4.1.2.4.1 Jet-milling

A Model 4 micro-jet jet mill from Fluid Energy Aljet was used to crush the bulk pitch into a fine powder. The size distribution was measured by optical image analysis and shown to be in agreement with the manufacturer's measurements which were made by laser diffraction analysis. A uniform distribution from one to three microns was confirmed with an average size of approximately 1.5 microns.

#### 4.1.2.4.2 Oxidation of powders

Oxidation of the pitch powders was performed in 9"x12" aluminum pans which were filled with 100 g each of pitch powder, giving a bed depth of less than 1 mm. The pans were placed in a 160°C oven and their positions rotated every 24 hours, until a weight gain of approximately six percent was achieved. Table 7 gives the weight gains and oxidation times for a number of powder specimens used in later production of composites.

**TABLE 7**  
**Oxidation Weight Gains**

<b>Sample</b>	<b>% Weight Gain</b>	<b>Oxidation Time (h)</b>
160-1	5.10	120
155-0	5.52	118
155-1	5.96	136
160-2	6.13	125
160-4	6.25	117
160-5	6.93	118



#### 4.1.2.4.3 Preparation of suspension mixtures

The initial formulation for the powder suspension was taken from previous in-house work with powder-based poly(ether-ether ketone) (PEEK) and APC-2 thermoplastic composites. The specification included Carbopol 972 and Triton X-100 as suspension aid and dispersant, respectively. Prior to the purchase of Carbopol compound from BFG Chemical, poly(acrylic acid) was used as a suspension aid. This additive proved marginally effective in thickening of the suspension but was used in most of the early prepregging work. The composition of all prepreg mixtures is included in Table 8. The relative water-to-powder ratio was varied in order to evaluate its effect on prepregging and on the distribution of powder inside the fiber tows. The suspensions were mixed using a three- blade propeller-type laboratory mixer. The powder was added last and mixed for at least five minutes to obtain uniform mixtures. No effect of powder content on prepregging was observed in the vertical die work.

#### 4.1.2.4.4 Prepreg vertical die and spreader bar position

The physical arrangement of the vertical prepregging apparatus is shown in Figure 52. The fiber is guided into the bath of suspension, around a number of stationary spreader bars, and through a round die.

The path of the fiber through the spreader bars and the position of the spreader bars were varied as listed in Table 9 under fiber spreading mechanism. Figure 53 shows the arrangement of each bar position and fiber path used in the study. The die size was also varied, as shown in Table 9, with exit diameters ranging from 1.5 to 2.7 mm. The large variation is due to the use of 2K, 10K, and 12K fiber tow sizes. Winding and traverse speeds were varied for some conditions and are also listed in Table 9.

**TABLE 8**  
**Composition of Pitch Powder Suspensions used in Prepregging**

Date	Pitch Content (g)	Water Content (g)	Glycerin (g)	Triton (g)	PAA (25%) (g)	Carbopol (g)
10/15/97	472	306	18	0.53	9	
10/20/97	60	89	2	0.07	1	
10/20/97	75	59	2.89	0.09	1.5	
11/4/97	202	120	36	0.58	9.2	
11/5/97	59	63.5	10.5	0.16	2.7	
11/10/97	200	180	36	0.5	9	
11/10/97	66.7	60	12	0.16	3	
11/12/97	56.4	62.8	10	0.14	2.5	
12/2/97	200	200	18	0.5	9	
12/2/97	200	200	18	0.5	9	
1/6/98	200	200	18	0.5	9	
1/6/98	200	200	18	0.5	9	
1/8/98	150	200	18	0.5	9	
1/26/98	38	97	1.4	0.04		0.36
2/3/98	161.5	300	6	0.15		1.5
2/5/98	161.5	300	6	0.15		1.5
2/5/98	161.5	300	6	0.15		1.5
2/9/98	129	300	6	0.15		1.5
2/12/98	100	300	6	0.15		1.5
2/20/98	161.5	477	6	0.15		1.5
2/20/98	161.5	477	6	0.15		1.5
2/26/98	161.5	477	6	0.15		1.5
4/28/98	120	477	6	0.15		1.5
5/1/98	80	234	3	0.07		0.4
5/5/98	80	233	3	0.08		0.15

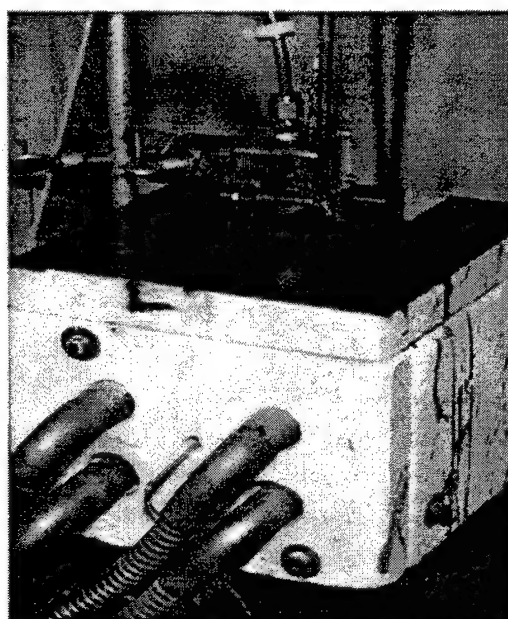


**Figure 52. Vertical Infiltration Bath with Die.**

**TABLE 9**  
**Conditions for Pitch Powder Prepregging**

D a t e	Fiber	Tow Size	Pitch Oxidation (%)	% Pitch	Die Size	Fiber Spreading Mechanism	Winding Speed	Drum Speed
10/15/97	K137	10K	5.40	59	2.4	no bars	282	45
10/20/97	K137	10K	5.40	39	2.4	no bars	282	45
10/20/97	K137	10K	5.40	54	2.4	no bars	282	45
11/4/97	K137	10K	6	55	2.4	no bars	250	45
11/5/97	K137	10K	6	43	2.4	1/2 bars	500	90
11/10/97	K137	10K	6.10	47	2.4	1/2 bars	250	50
11/10/97	K137	10K	6.10	47	2.4	1/2 bars	250	50
11/12/97	K137	10K	6.10	43	2.4	1/2 bars	250	50
12/2/97	K137	10K	6.10	47	2.4	1/2 bars	250	45
12/2/97	K137	10K	6.10	47	2.4	1/2 bars	250	60
1/6/98	P-30X	2K	5.10	47	1.7	1/2 bars	250	45
1/6/98	P-30X	2K	5.10	47	slit die	1/2 bars	250	45
1/8/98	P-30X	2K	5.10	40	1.7	1/2 bars	250	45
1/26/98	K137	10K	0	28	2.4	standard bars	100	21
2/3/98	K137	10K	0	35	2.4	standard bars	100	30
2/5/98	K137	10K	0	35	2.7	standard bars	100	30
2/5/98	K137	10K	0	35	2.2	standard bars	100	30
2/9/98	K137	10K	0	30	2.4	standard bars	100	30
2/12/98	K137	10K	0	25	2.4	standard bars	100	30
2/20/98	K137	10K	0	25	2.4	standard bars	100	30
2/20/98	K137	10K	0	25	2.7	standard bars	100	30
2/26/98	P-30X	2K	0	25	1.5	standard bars	100	30
4/28/98	AS-4	12K	0	20	2.4	air spreader	100	30
5/1/98	AS-4	12K	0	25	2.4	air spreader	100	65
5/5/98	AS-4	12K	0	25	2.4	air spreader	100	65

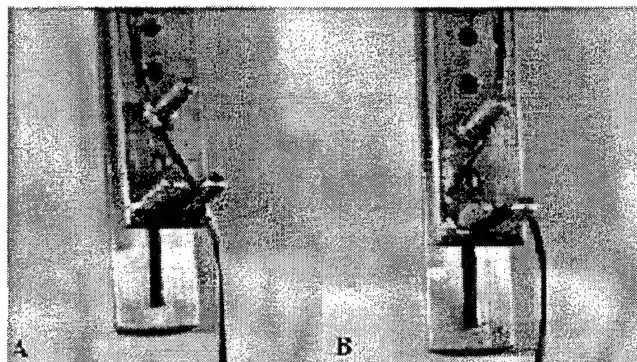


**Figure 53. Spreader Bar Positions and Fiber Paths: (A) 1/2 Bars, (B) Standard Bars.**

Table 8 lists the total content of the suspension mixtures used in the prepregging operations of Table 9.

#### 4.1.2.4.5 Air-comb fiber spreader

It was believed that improved infiltration could be achieved if the fiber tows were spread prior to entering the suspension bath. An air-comb fiber spreader was designed and fabricated to spread the fiber tows efficiently without causing damage. Figure 54 shows the spreader and its dimensions. The spreader worked well with unsized fiber, but required a high airflow to spread the epoxy sized K321-10 and P30X fiber being used in the prepregging. Approximately 50 psi of air pressure from a compressed air cylinder is required to spread the 2K P-30X, and it occasionally requires manual spreading to maintain the condition. This pressure was required at the lowest fiber tension available using the current equipment. Use of the fiber spreader with the vertical die did not improve infiltration of fiber tows, but it did work when used with the horizontal bath.

#### 4.1.2.4.6 Results using vertical die

The vertical die arrangement resulted in poor distribution of powder inside the fiber tows for all conditions attempted in Table 9. Figure 55 shows the lack of powder within the fiber tow for a typical prepreg produced using this arrangement.

The prepreg was cut from the drum in six-inch sections, giving 12 plies for each two-inch-wide prepreg. Six plies per panel were laid up in a 2"x6" mold, being sure to alternate top and bottom surfaces symmetrically about the center of the laminate. Hot pressing was performed at 275 to 350°C and 5 or 10 ksi with most

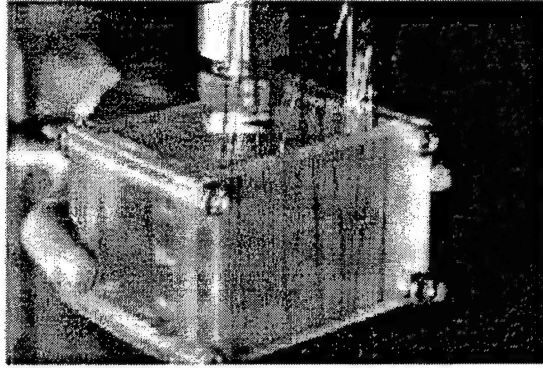


**Figure 54. Air-Comb Fiber Spreader.**

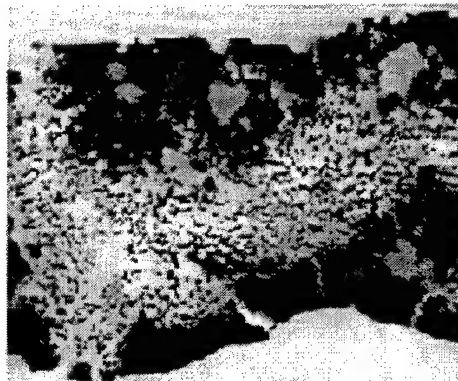


**Figure 55. Fluorescence Illuminated Fiber Tow Cross Section showing Lack of Powder Infiltration.**

heat-up times of 45 minutes and pressing times of 60 minutes. Conditions for each panel are listed in Table 10. All panels were carbonized at 2°C per minute to 900°C.

Large voids and pores were observed after carbonization. Resin-rich areas with voids and shrinkage cracks were observed between the fiber tows as seen in Figure 56. Mechanical testing in flexure of five bars cut from specimen S6P1 resulted in a very low average strength of 5 ksi. This is due to the lack of penetration of powder into the fiber tows and possibly low fiber-matrix interface strength. The infiltration of powder into the fiber tows was thought to be affected mainly by the viscosity of the suspension, which is controlled by the thickener content. As the thickener was reduced and

**TABLE 10**  
**Pressing Conditions for Vertically Prepregged Composites**

Panel	Prepreg	Press Temperature	Pressure	Heat-up Time	Pressing Time
S1P1	S1	350	10000	50	40
S1P2	S1	300	5000	45	45
S3P1	S3	300	5000	45	30
S3P2	S3	275	5000	45	45
S4P1	S4	300	5000	45	75
S5P1	S5	300	10000	50	45
S6P1	S6	300	5000	45	60
S6P2	S6	275	10000	60	75
S7P1	S7	300	10000	45	60
S7P2	S7	275	10000	45	60
S8P1	S8	300	10000	50	65
S9P1	S9	300	500	45	60
S9P2	S9	275	10000	45	60
T1	S10	275	5000	65	60
T12	S10	200	10000	60	60



**Figure 56. Polarized Light Image of Transverse Section showing Shrinkage Cracks between Tows.**

the viscosity dropped, the flow of suspension out of the die increased to the point where it flowed rapidly out of the bath. This led to the use of a bath without a die and with the fiber passing horizontally through the mixture.

#### 4.1.2.4.7 Horizontal prepregging bath

Figure 57 shows the horizontal bath with the fiber passing through the fiber spreader and then into the bath, under two 1" Teflon rollers, then out of the bath at an angle near vertical and over another roller before being wound on the drum.

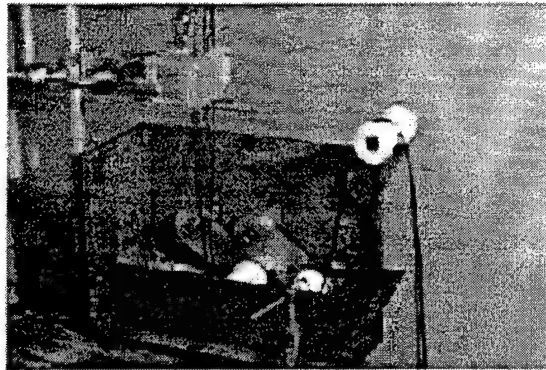


**Figure 57. Arrangement of Horizontal Infiltration Bath.**

The bath hardware was assembled from a previous setup for solution prepregging. Teflon rollers 1.5" wide were manufactured to guide the spread fiber tows through the suspension bath. Two submerged rollers, 1" in diameter and 2" apart, guide the fiber through the bath and act to infiltrate the tows. A third roller positioned above the bath controls the angle which the tow exits the bath; setting a large angle allowed excess resin to drip back into the bath. The previously-developed air-comb fiber spreader was arranged vertically above the infiltration bath, and a shield was fitted to prevent the airflow from splashing liquid from the bath. A magnetic stirring bar rotating in the bottom of the bath keeps the suspension stirred.

The change in infiltration hardware required a re-evaluation of the suspension mixture, including the type and concentration of additives as well as pitch powder. Variables affecting infiltration are mainly viscosity, surface tension, and particle size distribution of the suspension. The purpose of including the additives is to suspend the particles and help attach the particles to the fiber during processing. In the vertical process a polyacrylic acid polymer called Carbopol 674 was used as a thickener, but as the concentration was lowered, the binding of powder to fiber was reduced and resulted in poor prepregs. In order for the powder to bind to the fibers during the process, a higher concentration of binder was required without a large increase in viscosity. Alternative binders were considered, and polyvinyl alcohol and Carbopol 672 were subjected to foaming and binding tests at several concentrations.

Polyvinyl alcohol was evaluated as a potential binder by preparing solutions of 1, 1.5, and 2 percent with 0.2 percent borax added after dissolution by heating. Fiber tows were dipped in the cooled solutions and allowed to dry. The degree to which the fibers stuck together was observed as a measure of binding ability. Pitch powder was added to the solutions to determine wetting and foaming properties. The polyvinyl alcohol solutions wet the pitch powder very poorly, resulting in a large mass of foam floating on top of the liquid. This condition was improved when the surfactant Triton X-100 was added, but even then large powder agglomerates were visible, and clumping was apparent on fiber tows dipped in the suspensions.

Carbopol 672 was also evaluated as a suspension aid and binder for the process. It had been included with the samples of Carbopol 674 but was not previously utilized due to its very short flow rheology being inappropriate for the



vertical process. The viscosity of a one-percent solution of 672 was shown to be much lower than that of 674 and displayed much less foaming. Suspension mixtures of 0.25, 0.5, and 1 percent Carbopol 672 were prepared by stirring. Pitch powder was added to a level of 12.5 percent by weight, and the suspensions were evaluated for foaming or floating of dry powder on top of the liquid. Both the 0.25 and 0.5 percent suspensions resulted in powder floating on top of the liquid, while the one-percent suspension was completely wet-out. Dipping of fiber tows in the suspensions and allowing those to dry revealed good binding for all three concentrations, with higher concentration yielding slightly stiffer tows after drying. The addition of one-percent glycerin and trace amounts of Triton X-100 were used in the prepreg formulation to improve drape and tack and reduce aggregate size, respectively.

A standard batch suspension mixture was established as a starting point in the development of the aqueous suspension infiltration process. To 600 ml of distilled water were added 6g Carbopol 672, 6 g glycerin, eight drops of one-percent Triton X-100 and 75 g of pitch powder. This suspension mixture was held constant while prepregs were prepared at increasing winding speeds. After winding, fiber tows were removed and evaluated for infiltration of powder into the tows. A significant improvement over the vertical process was observed with approximately 80 percent of the fibers individually surrounded by powder.

#### 4.1.2.4.8 Panel fabrication

Prepregs were laid up in a 2"x6" mold for pressing. Six-ply unidirectional composites were fabricated by hand. Prepregs less than two inches wide were assembled into 2"-wide plies. The plies were placed face up and face down symmetrically, with a smooth side resulting from the surface of the porous Teflon onto which

the prepreg was wound. Resin distribution was observed to be uneven on the outer surface of the prepreg after drying, with fiber being clearly visible on approximately 50 percent of the surface.

Pressing of composites was performed at 300°C and 5000 or 10,000 psi for 60 minutes. Compacts were consolidated successfully, but the outer faces of the matrix stuck to the mold surface and peeled off layers of fiber. Kapton release film was found to prevent sticking to the mold when used on the top and bottom surfaces of the composite. Observation of the 300°C compacted composites revealed large interlaminar cracks and voids which may have formed as a result of releasing pressure while the mold was still hot. Pressing at 400 and 500°C resulted in much better microstructures, displaying only small interlaminar cracks, when the pressure was held constant during cool down. Many of the interlaminar cracks may have formed during the cutting of specimens. The matrix is very weak before carbonization, and the forces induced by cutting may have caused the cracks to open up; however, after carbonization the matrix should have much higher strength, and there should be less cracking induced by cutting.

#### 4.1.2.5 *Encapsulated Oxidants for Mesophase Pitch Stabilization*

The production of carbon-carbon composites with controlled thermal properties in the matrix has been achieved through the use of mesophase pitch matrices. Flow of the anisotropic mesophase during processing often aligns portions of the graphitic planes with the fiber axes. This alignment is maintained during subsequent pyrolysis if a thermal oxidation is performed on the composite preform. The oxidation prevents flow and bloating of the pitch by forming linkages between pitch molecules. One limitation of this process is that the depth of penetration of the oxidation is less than 50  $\mu\text{m}$ ,

therefore thick parts cannot be produced this way. By incorporating an oxidizing agent into the matrix prior to processing, it may be possible to produce thicker parts without flow occurring after the initial compression molding. In order to combine the oxidant with the pitch and not have it affect the molding process above the softening point of the pitch, encapsulation is necessary. As an initial feasibility study, ammonium nitrate was encapsulated in Ultem polyetherimide by Southwest Research Institute, and the resulting microcapsules were mixed with pitch powders and processed. It was shown by Ciminelli that bloating could be reduced with increasing amounts of oxidant in the initial powder mixture. Further reduction in bloating during carbonization was reported after heat treatments of 300°C and 350°C were performed on the composites. Bloating was measured as a volume expansion factor of carbonized volume divided by initial volume. Untreated AR pitch expands around 84 times due to bloating during carbonization. In the study up to 50 percent by weight of microcapsules were added to the pitch powder which resulted in the smallest expansion factor of 1.1 after being heat treated to 350°C.

#### 4.1.2.5.1 Evaluation of composite specimen

Ciminelli also fabricated composites with microcapsules by adding vapor grown carbon fibers (VGCF) to the powder mixture and by hand lay-up using T-300 plain- weave fabric, distributing powder between the fabric layers. While the VGCF improved bloating behavior somewhat, the fabric composite held together without bloating and was deemed a successful demonstration of the concept. On further inspection this fabric composite had an extremely porous microstructure, as seen in Figure 58, which shows why the panel had very low density and strength.

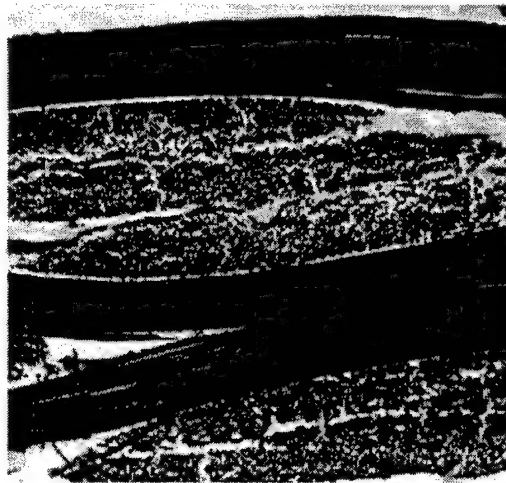


**Figure 58. Fluorescence Image of Composite Fabricated with Encapsulated Oxidants.**

While this image shows the voids, bright-field optical microscopy reveals matrix material surrounding the separated fibers well inside the fiber tow. Polarized light images confirm that the matrix is anisotropic and has a flow texture within the tows and a small region of powder texture between the tows. No evidence of the large (120  $\mu\text{m}$ ) microcapsules could be observed, and it is not clear what effect the Ultem has on the matrix quality.

#### **4.1.2.5.2 Moisture pickup of microcapsules**

The microcapsules contain 40 percent ammonium nitrate and 60 percent Ultem as a shell. Observation of the microcapsules in the SEM (Figure 59) shows that the spheres have collapsed which may have been due to drying at 100°C in vacuum for several hours or the result of the manufacturing process. The microcapsules were dried after problems were encountered during room temperature pressing of one-inch chips at 5000 psi. Drops of water were ejected from the die during pressing, and hairs of material grew out of the compacts immediately after pressing. The water drops evaporated to leave



**Figure 59. SEM Image of Microcapsules after Drying.**

ammonium nitrate crystals, and the hairs were identified by FTIR to be mainly Ultem with some ammonium nitrate. Drying and storage of the microcapsules in a desiccant has eliminated the problems, but the problem with moisture may eliminate the use of water-based suspension prepregging with encapsulated ammonium nitrate.

#### 4.1.2.5.3 Evaluation of heat-treatment process

In order to obtain more data on the heat treatment process performed by Ciminelli, a series of experiments was performed. Pure powdered ammonium nitrate was compared to encapsulated ammonium nitrate by mixing 10, 20, and 30 percent of the pure and 30, 40, and 50 percent of the microcapsules with jet-milled pitch powder in a shaker mill for 30 seconds. The mixed powders were then pressed into 1"-diameter chips at room temperature and 5000 psi. Pressed chips were heat treated to 250, 300, and 350°C for one hour after heating at 0.5, 1, and 2°C per minute. Expansions were measured as percent change in thickness. The microcapsules resulted in a more uniform expansion, with the center expanding more than the edges, leaving large cracks on the top and bottom as well as the sides, while the pure ammonium nitrate resulted in a bubbly surface with few cracks on the top and bottom but many cracks on the sides, which expanded as

much as the center. Lower heating rates and final temperatures gave lower expansion and lower weight loss for each concentration of oxidant as can be read from Table 11. Higher concentrations of oxidant gave higher weight loss for both the pure ammonium nitrate and the microcapsules, but expansion varied for both cases, with the middle concentration generally resulting in more expansion than the low and high values.

**TABLE 11**  
**Heat Treatment of Pitch and Oxidant Mixtures**

Sample	Ramp	Temp.	% Pitch	% AN	% Ultem	% Wt. Loss	% Thick. Chg.	% Dia. Chg.
MC301	2°C/min	350	70	12	18			
MC401	2°C/min	350	60	16	24	-8	397	-1
MC501	2°C/min	350	50	20	30	-12	491	-35
AM101	2°C/min	350	90	10	0	-12	216	1
AM201	2°C/min	350	80	20	0	-20	286	7
AM301	2°C/min	350	70	30	0	-31	234	8
MC302	1°C/min	300	70	12	18	-6	391	4
MC402	1°C/min	300	60	16	24	-8	370	4
MC502	1°C/min	300	50	20	30	-11	305	2
AM102	1°C/min	300	90	10	0	-7	219	2
AM202	1°C/min	300	80	20	0	-16	265	9
AM302	1°C/min	300	70	30	0	-26	184	12
MC303	0.5°C/min	250	70	12	18	-5	336	-1
MC403	0.5°C/min	250	60	16	24	-7	354	1
MC503	0.5°C/min	250	50	20	30	-11	242	-2
AM103	0.5°C/min	250	90	10	0	-5	142	2
AM203	0.5°C/min	250	80	20	0	-12	99	1
AM303	0.5°C/min	250	70	30	0	-21	119	1

In the actual processing of composites, the expansion will be constrained during the heat-treatment step but not during carbonization. The composite panels of prepregged pitch and oxidant powders will be held under pressure while being heat treated. Evolved gases will escape from the mold, while the pitch will be retained within the dimensions of the composite. Any bloating of pitch that occurs during heat treatment reduces the amount of bloating that later occurs during carbonization, so this act of heat treatment will reduce the overall bloating of the composites.

Chemical analysis of the process was performed with FTIR by observing the spectra before and after heat treatment. Oxidation of pitch could be identified by the formation of carbonyl bonds, and the breakdown of ammonium nitrate was complete as there were no remaining N-H or N-O absorptions after heat treatment.

The relative amounts of oxidant required to reduce bloating are significant, and their breakdown reduces the overall char yield of the system. This is detrimental to the desired elimination of densification steps in the processing and, coupled with the fact that the evolved gasses form voids and expand the composite, results in the conclusion that adding oxidants does not increase the density of the carbonized composite as compared to traditional methods. The microstructure resulting from pitch run-out and bloating in a conventional process will be different from the microstructure resulting from using internal oxidants, but how that will affect mechanical behavior is not known. Potentially, alternative sources of oxygen may perform better.

## **4.2 Graphitic Foams**

Graphitic foams have the potential for use as core replacements between composite sheets or used directly as composite reinforcements. Model graphitic foams were predicted [54] to have a compression modulus of approximately 2 GPa with a density of about 0.1 Mg/m<sup>3</sup>. Not many other foams or core materials have a density and compression modulus near these values. Structural composites are based on disconnected carbon fibers integrated into some type of matrix. The strength and stiffness of commercial carbon fibers are due to the graphitic morphology that originates from the melt spinning of the precursor pitch. If an interconnected network of struts could be produced which possessed a similar morphology to the carbon fiber, a new generation of composite reinforcement could emerge.

Foams are an example of such materials. An open-cell structure is the desired architecture for resin infiltration as a composite preform and drainage as a core material.

Microcellular, open-cell foams can be produced from anisotropic pitch with graphitic planes aligned along the struts [55]. The process sequence includes blowing, stabilizing, carbonizing, and then graphitizing the foam, similar to the process for manufacturing pitch-based carbon fibers.

#### 4.2.1 Cellular Structure of Net-Shaped Pitch-Based Microcellular Carbon-Foams

This study was a successful initial attempt to demonstrate that such a foam could be blown into a net-shape as a composite preform or core replacement material. This work was undertaken to determine what processing changes were needed to produce a net shape in the final foams and the effects of those processes on the foam structure. Quantification of bubble sizes, uniformity and porosity was performed using optical microscopy and image analysis. These foam structural parameters were measured as a function of location within the foams for each of the shaping methods. Porosity did not vary significantly among the processing variables or location. The bubble sizes and uniformity did vary in the foams, particularly with each foam having some large bubbles on its bottom surface. Density and porosity were also measured using water displacement with similar results. Free expansion of a shaped preform produced the most variability, and foaming into a mold produced the least variability and best net-shape. This work was done in part by the Wright-Connection teachers program. The results were reported in a SAMPE paper and presentation [56].



Three methods were attempted to produce a foam of net shape. The methods are described below. The first method, called "extruded," used a discotic preform that was blown into a foam, and the still hot soft foam was pressed (or extruded) into a mold of rectangular shape. The second method consisted of cutting the preform into a rectangular cross section that just fit into a metal mold of the same shape where it was blown into a foam: this method is called "molding." The third, or "free expansion," method started with preforms cut into a rectangular shape; these preforms were allowed to expand freely during the blowing operation.

The foams were cut into multiple sections to be examined primarily by optical microscopy but also SEM. The sections of the samples for optical microscopy were cut according to Figure 60 to allow observation of several different locations and specimen orientations for each of the foamed samples. After vacuum-infiltrating the samples with a fluorescently-dyed epoxy potting resin and polishing, the plugs were examined in both bright-field and fluorescent illumination. Images were obtained using a CCD digital camera, and these images were used to measure the bubble sizes and porosity in the foams as described in the Delivery Order No. 0006 Annual Report.

Density measurements were made on carbon foam specimens using the Archimedes displacement method with water (ASTM C 373-72 for porous ceramics). Samples were cut from each processing specimen to obtain measurements from top, bottom, inside, and outside. The very outer skin of each sample was removed before measurement.

Photographs of the four samples (duplicate of "free expansion") after foaming and carbonization are shown in Figure 61. It is immediately obvious that the two freely-expanded samples did not retain their rectangular cross sections but instead expanded

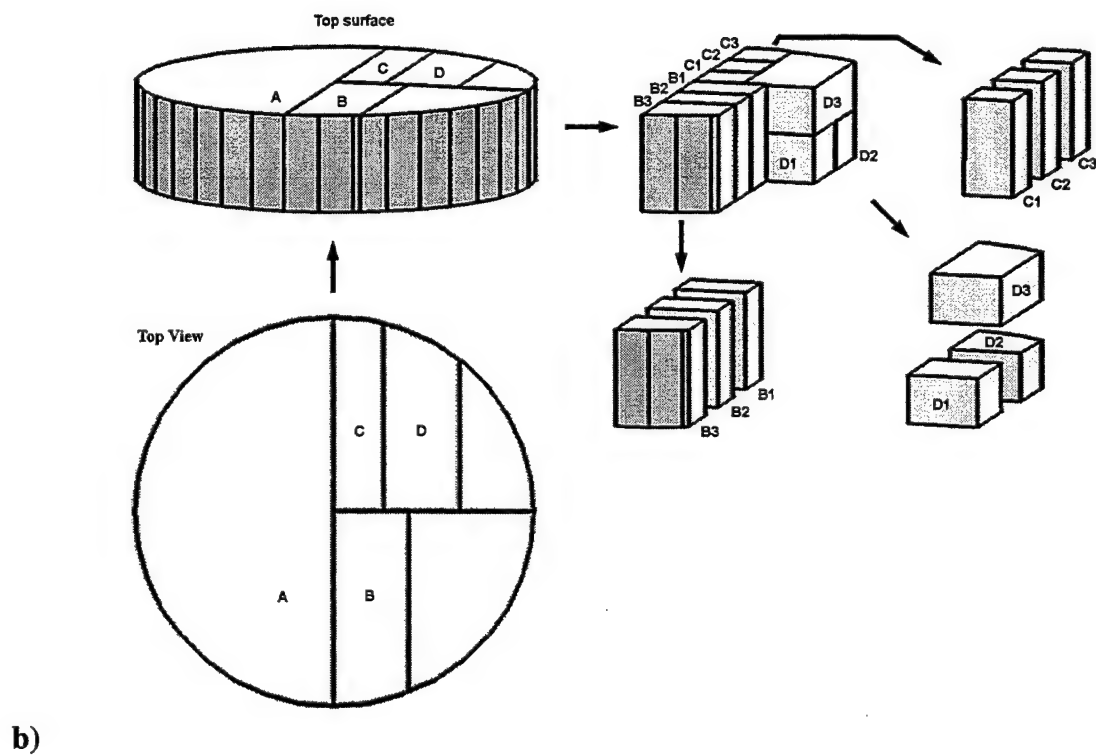
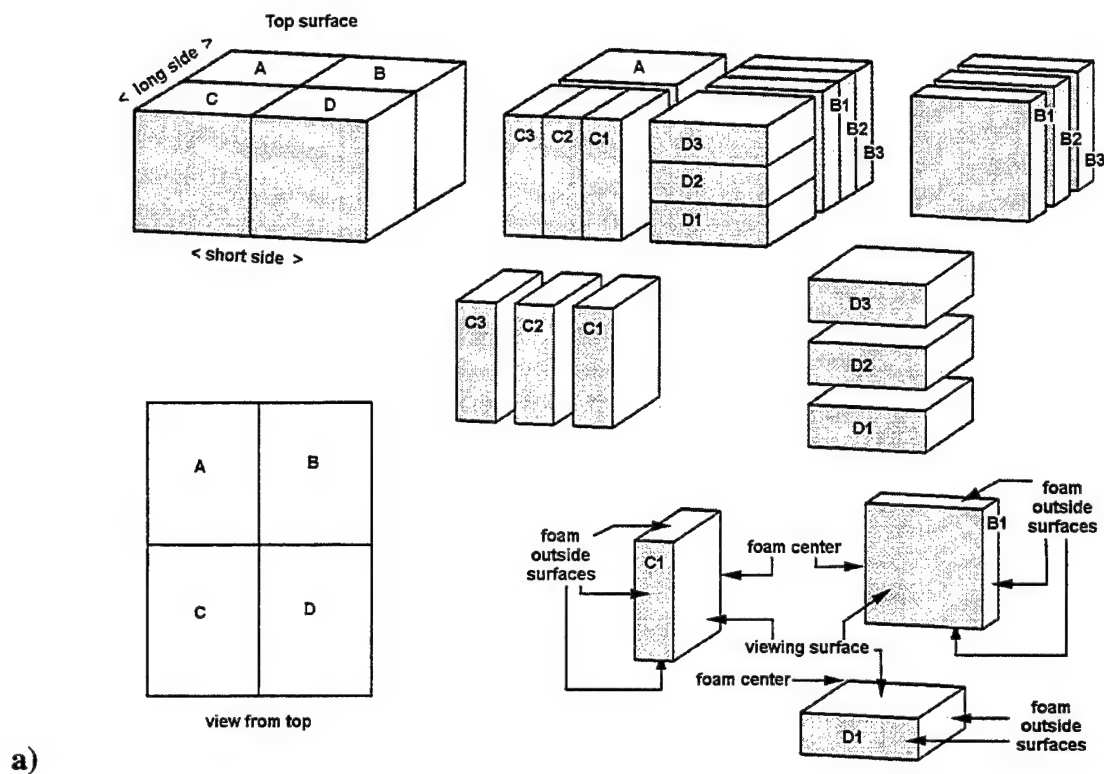


Figure 60. Cutting Diagram for the Foam Samples: a) for Rectangular Blocks and b) for the Cylindrical Pieces.

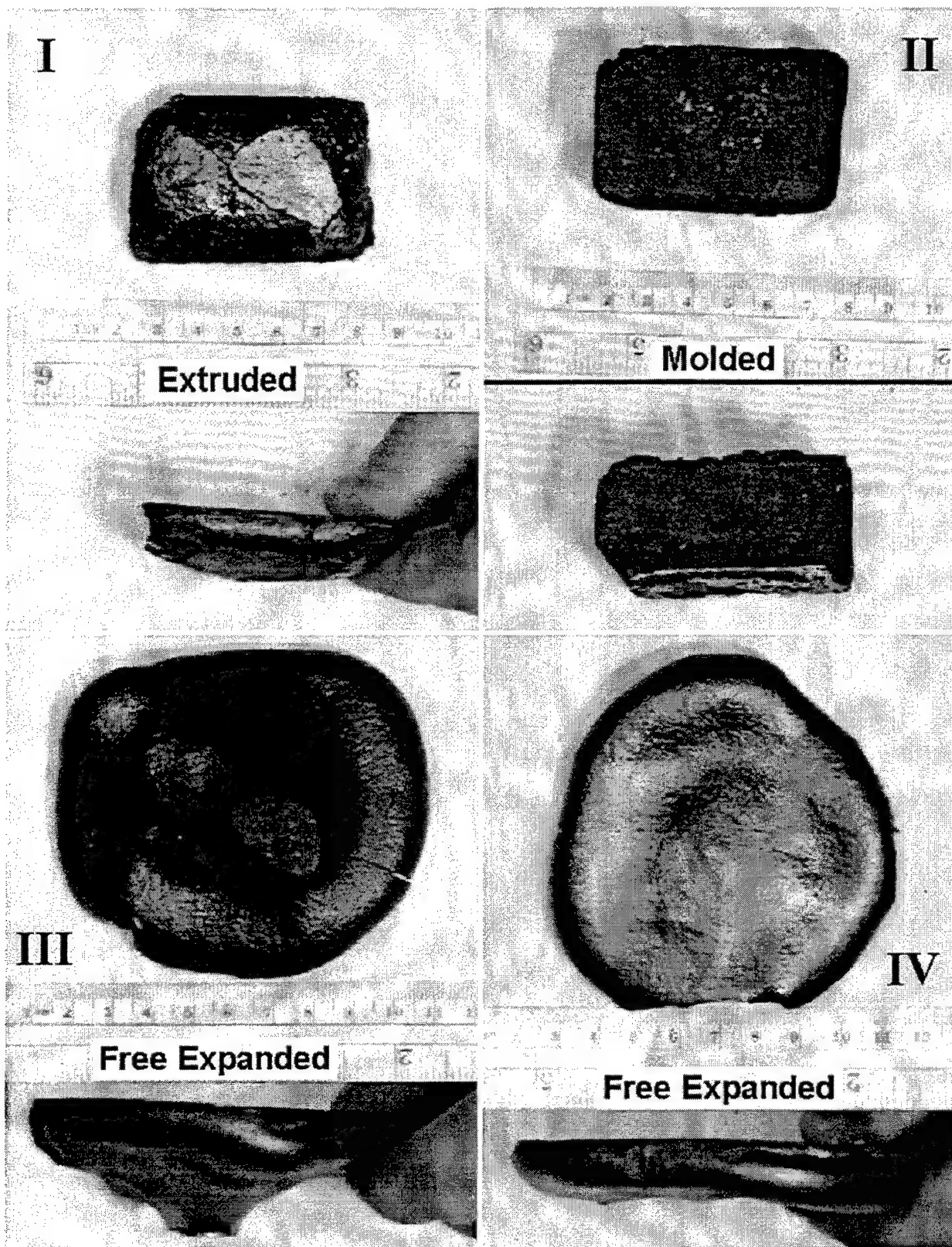


Figure 61. Photographs of "Net-Shaped" Foams.

into circular cross-section pieces. The foam blocks were classified as "rectangular" for the first two processing methods and "circular" for the freely-expanded processing method. The four samples were examined by optical microscopy as functions of location both from the foam center to outside edge and top to bottom. The viewing orientation was also varied for each of the samples. The orientations of observation were arbitrarily set as "B" to reveal surfaces normal to the foam's long in-plane direction or surfaces normal to the cylinder radial direction; "C" to reveal surfaces normal to the foam's short in-plane direction or surfaces normal to the cylinder hoop direction; and "D" to reveal surfaces normal to the through-the-thickness direction.

Image analysis of the fluorescent images to measure porosity was straightforward; the open-cell bubbles fill with the fluorescent resin and appear yellow against the black carbon struts. There did not appear to be a significant variation in porosity as a function of processing path, position in the foam samples, or orientation of observation. The foams had average porosity values of 81-82 percent. Deviations from the average in any particular view were due more to potting resin infiltration differences than from sample variations. The Archimedes displacement measurements gave porosity values of 87-89 percent.

The Archimedes "apparent porosity" results are shown in Figure 62. The average "apparent bulk densities" were even less variable with location. The average values for each of the samples are given in Table 12 along with the "apparent porosity" and "apparent density" values.

Bubble uniformity can be determined from the bubble size measurements but can also be evaluated qualitatively from a simple examination of an SEM photo.

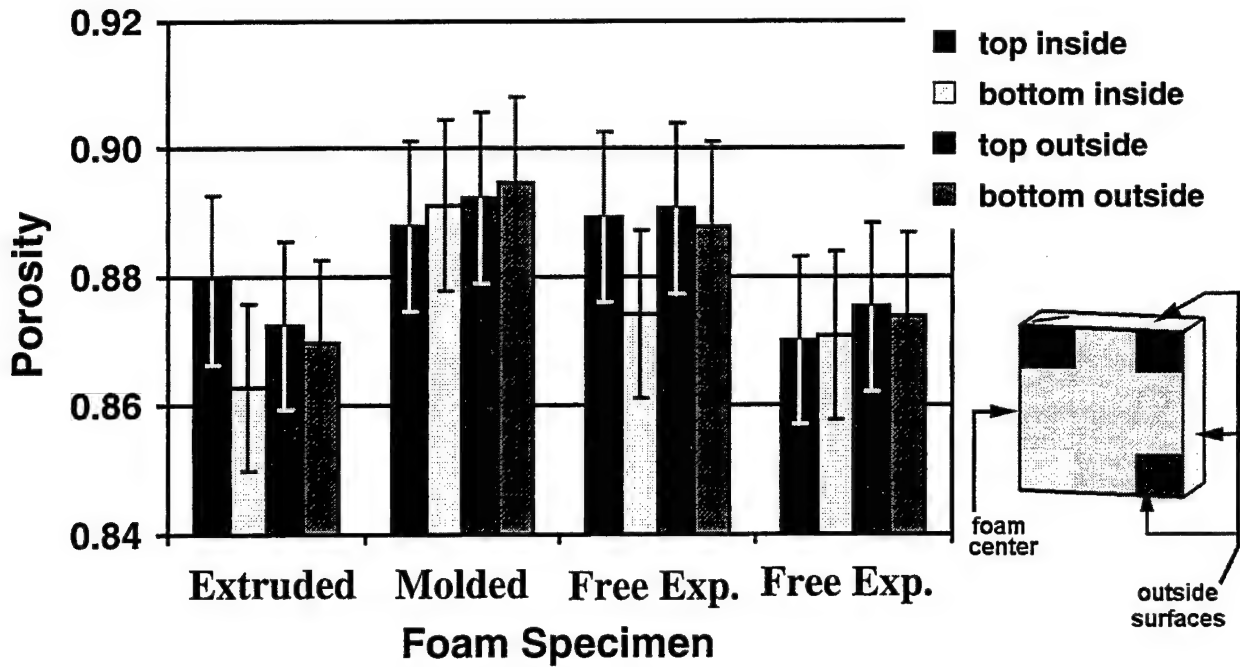


Figure 62. Archimedes "Apparent Porosity" Results by Sample and Location.

TABLE 12  
Archimedes Displacement Average Results

Sample Number	Apparent Porosity	Apparent Bulk Density (Mg/m <sup>3</sup> )	Apparent Density (Mg/m <sup>3</sup> )
I	0.871	0.241	1.871
II	0.892	0.206	1.911
III	0.885	0.220	1.916
IV	0.872	0.242	1.891

Figure 63 shows a typical SEM of molded foam. All of the foam samples showed similar uniformity of cell sizes.

Figure 64 shows the cell (or bubble) sizes as a function of viewing direction in the center of each specimen. Basically no major differences were noted within

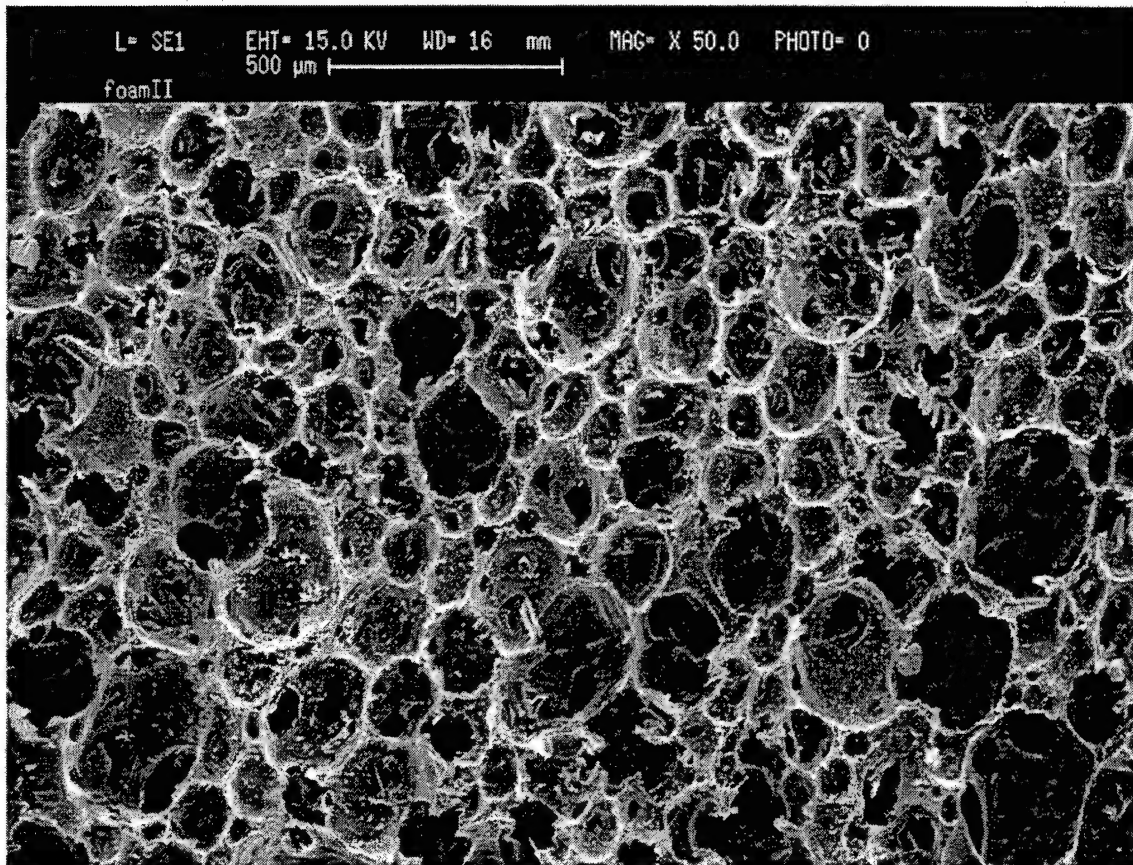


Figure 63. SEM of Molded Foam: Typical Uniformity of all the Foam Samples.

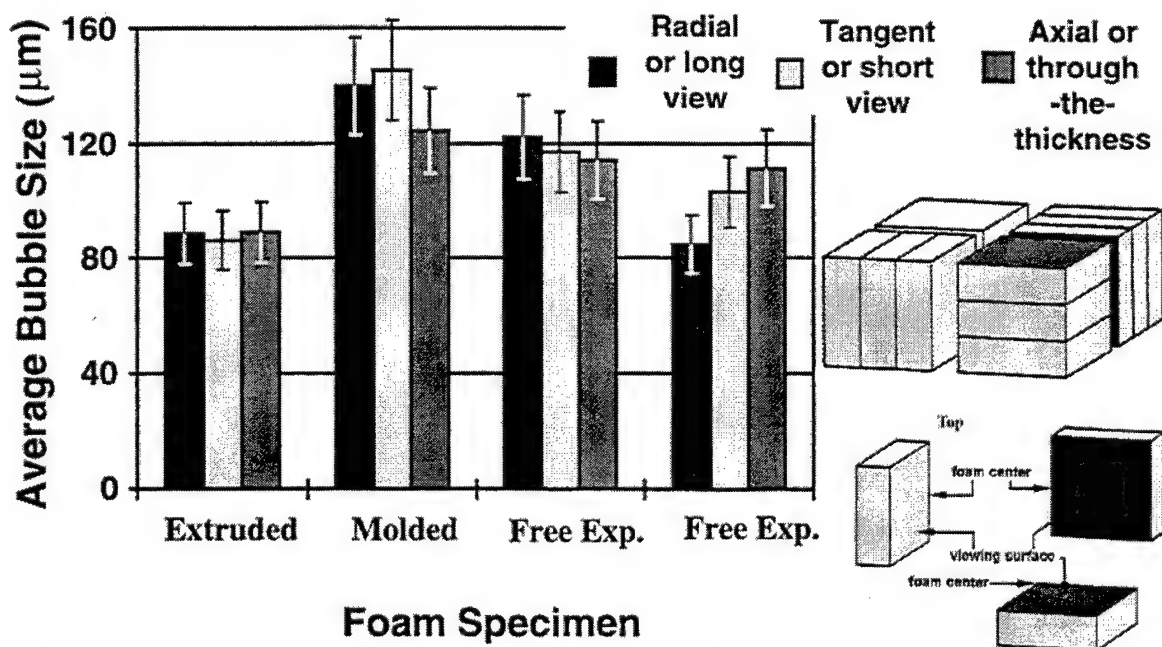
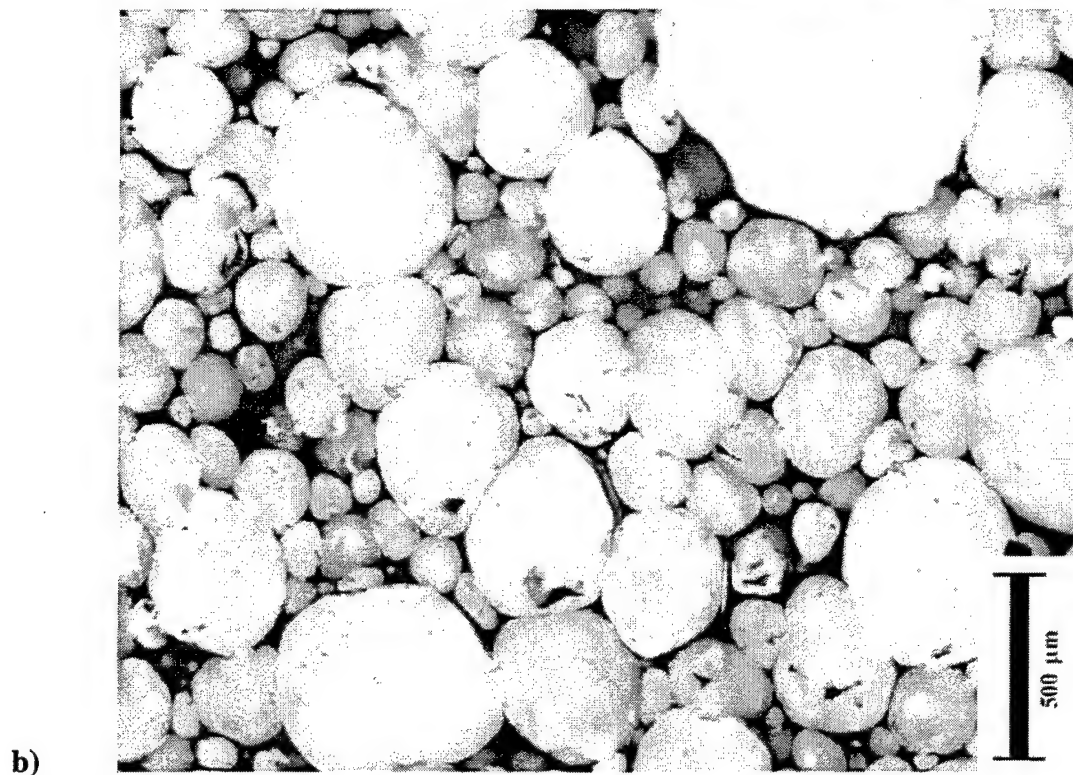
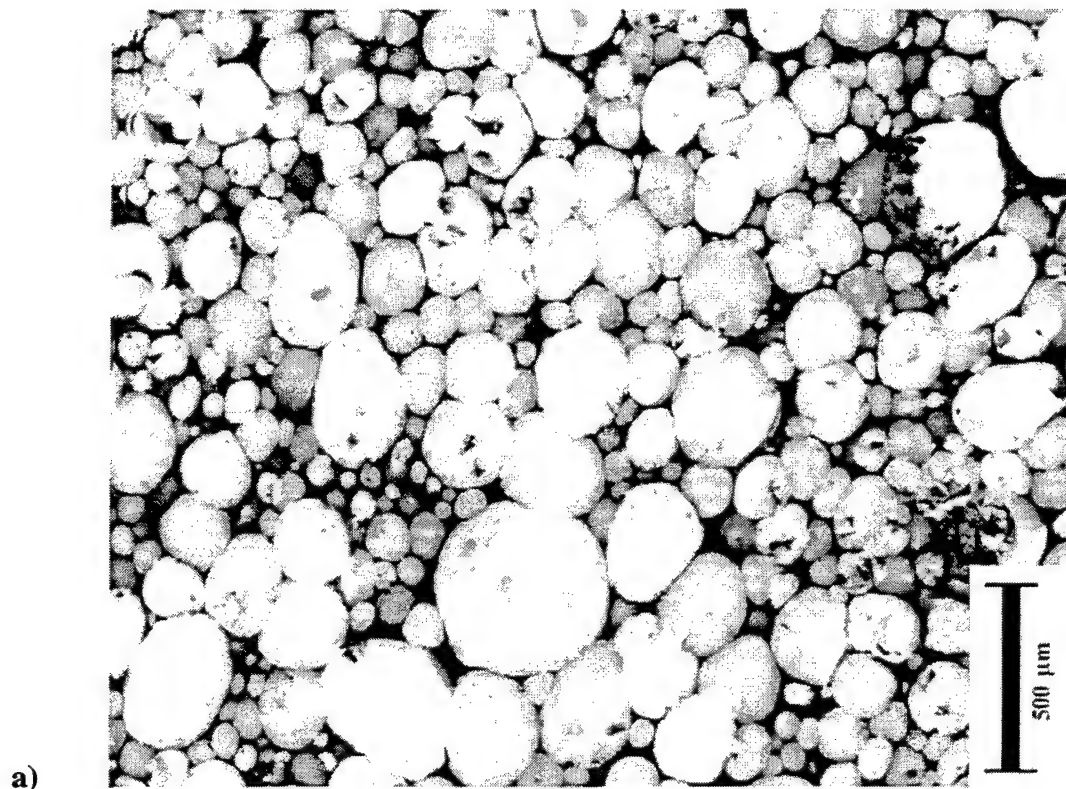


Figure 64. Average Bubble Sizes in the Center of the Foam Specimens as a Function of Viewing Direction.





**Figure 65. Fluorescent Micrographs of Foams: a) Typical Small-Celled Foam and b) Typical Large-Celled Foam.**

samples, which means that the bubbles are isotropic in this part of the foams. The difference in appearance of the largest to smallest bubble sizes is shown in Figure 65.

There were some differences among the foam specimens, but this can be seen more easily in Figure 66. This figure shows the average bubble sizes in the central part of the foam specimens as a function of location within the foam. The measurements were taken at the center of the foam and then at several other locations towards the outer part, but not at the very edges of the foams. The average bubble size of the extruded foam and one free expanded foam was slightly more than 80  $\mu\text{m}$ , the other free expanded foam was 110 to 120  $\mu\text{m}$ , and the molded was about 140  $\mu\text{m}$ .

More interesting are the differences from the center of the foams to the outer edges. Figure 67 shows the size average results. Only the molded foam appears to show much difference with the edges having a much smaller average size bubble than the center areas. What is not reflected in this figure is that the regions picked to count cells deliberately avoided some regions. In the extruded foam there were regions containing collapsed cells, apparently crushed during the extrusion operation. This is shown in Figure 68. Several attempts to produce a foam by extrusion showed that the foam had to be extruded when it was first removed from the blowing chamber and a hot mold used. Since no attempt was made to optimize these conditions, this technique might work without crushing cells if the problems of handling hot pitch and a hot mold together can be solved.

The crushed cells were one of three regions avoided during the cell size measurement operation. A skin, tens of micrometers thick, was on the very outside edge of each foam. The third region was one with very large cells, several millimeters in diameter; these were present in the latter three foams along the bottom edge, and these regions were



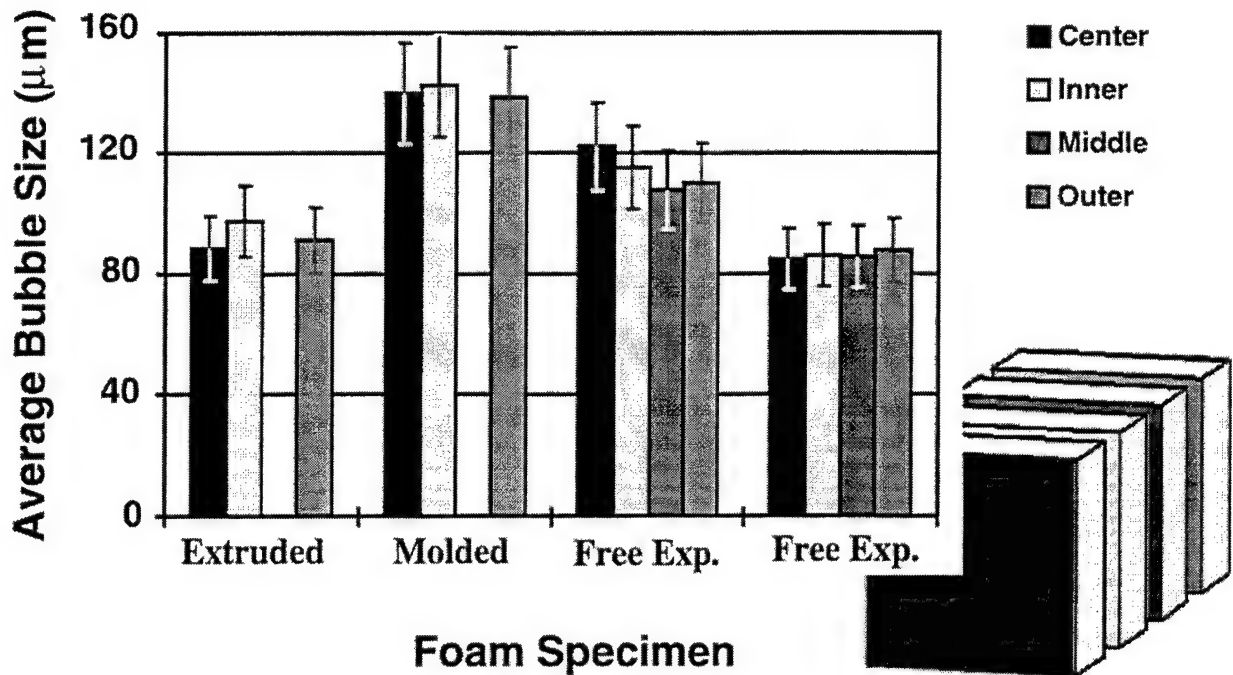


Figure 66. Average Bubble Sizes in the Central Part of the Foam Specimens as a Function of LOCATION from the Center of the Foam to the Outer Part (but not at the Edges).

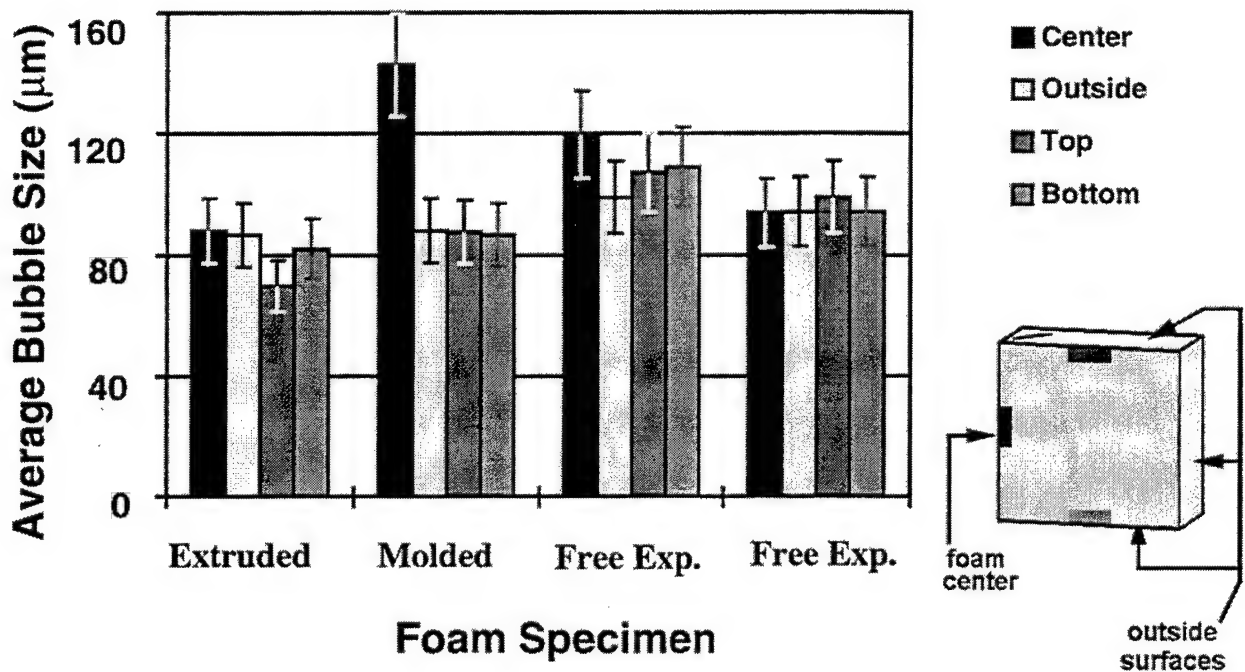
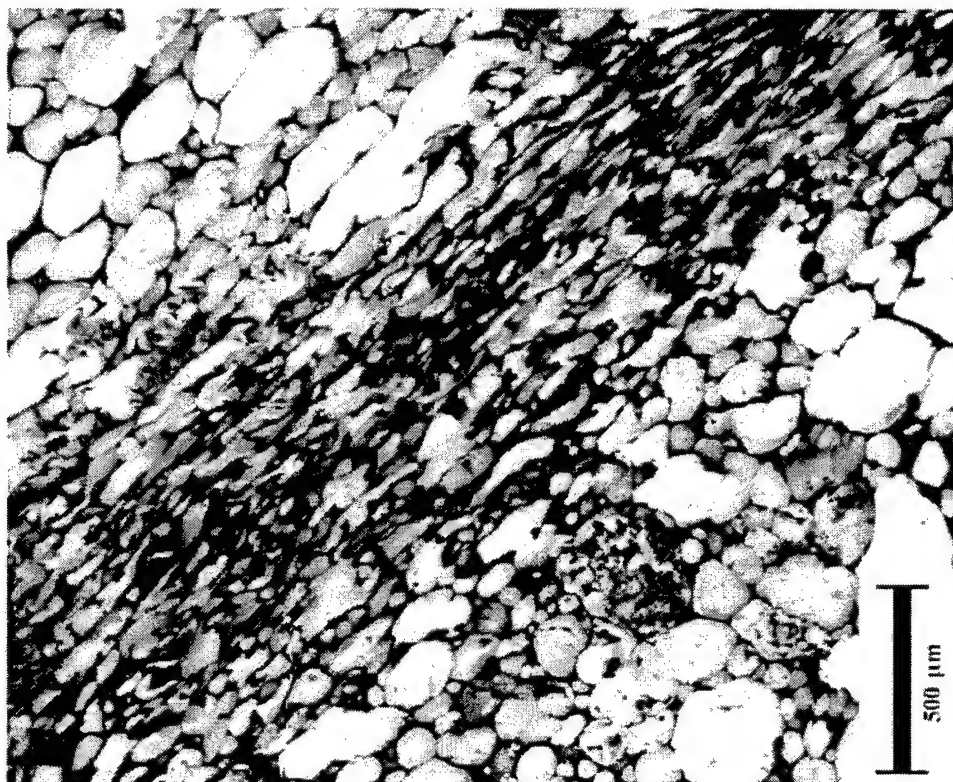


Figure 67. Average Bubble Sizes in the Central Part of the Foam Specimens as a Function of POSITION from the Center of the Foam to the Outside Edge, Top Edge and Bottom Edge.



**Figure 68. Example of Crushed Cells in the Extruded Foam.**

also avoided (see for example Figure 69). The latter represents the most common form of nonuniformity in these samples. It is unknown if large bubbles were formed in the extruded foam but collapsed during the extrusion process.

Foaming into a mold produces the best net shape, the final foam retaining the shape of the mold. The extrusion process in this study apparently crushed some cells but this could be dependent on the temperature of the foams and extruding molds which were not examined in detail. Foaming a shaped preform without restriction results in a circular foam and does not retain the preform shape. The cell size, porosity, and density for all the “net-shape” processing samples were relatively uniform. While the absolute sizes of the cells were somewhat dependent on the shaping method, other studies have shown a much greater dependence of these variations on other processing parameters [50,53,54].

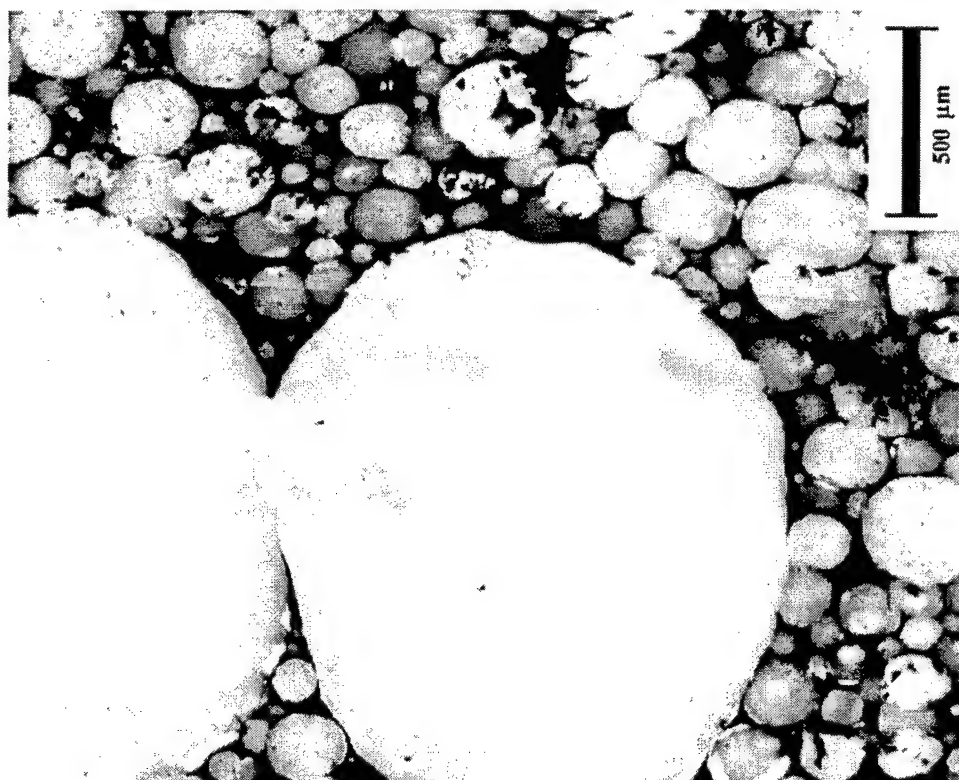


**Figure 69. Example of Occasional Very Large Cells.**

#### 4.2.2 Characterization of Foams made with Various Blowing Gases

In the past year foams made using both helium and argon gases were characterized. The results of these tests have been added to our knowledge of foams made using nitrogen and carbon dioxide. Both optical microscopy and Archimedes displacement were used to get foam porosity, density, bubble size, etc. values. The results for helium were presented in a paper at SAMPE [57], and a comparison of results for all four gases was made in a paper presented at the Material Research Society national meeting [58].

Each of the four gases was used to blow foams from the Mitsubishi AR pitch in a  $4^2$  factorial statistical matrix of eight samples: high and low levels of initial gas pressure (except  $\text{CO}_2$ ), final gas pressure, final temperature, and hold time at temperature.

Figure 70 shows the results from the volume expansion measurements during foaming. Note that each bar is an average of the four samples at the designated level

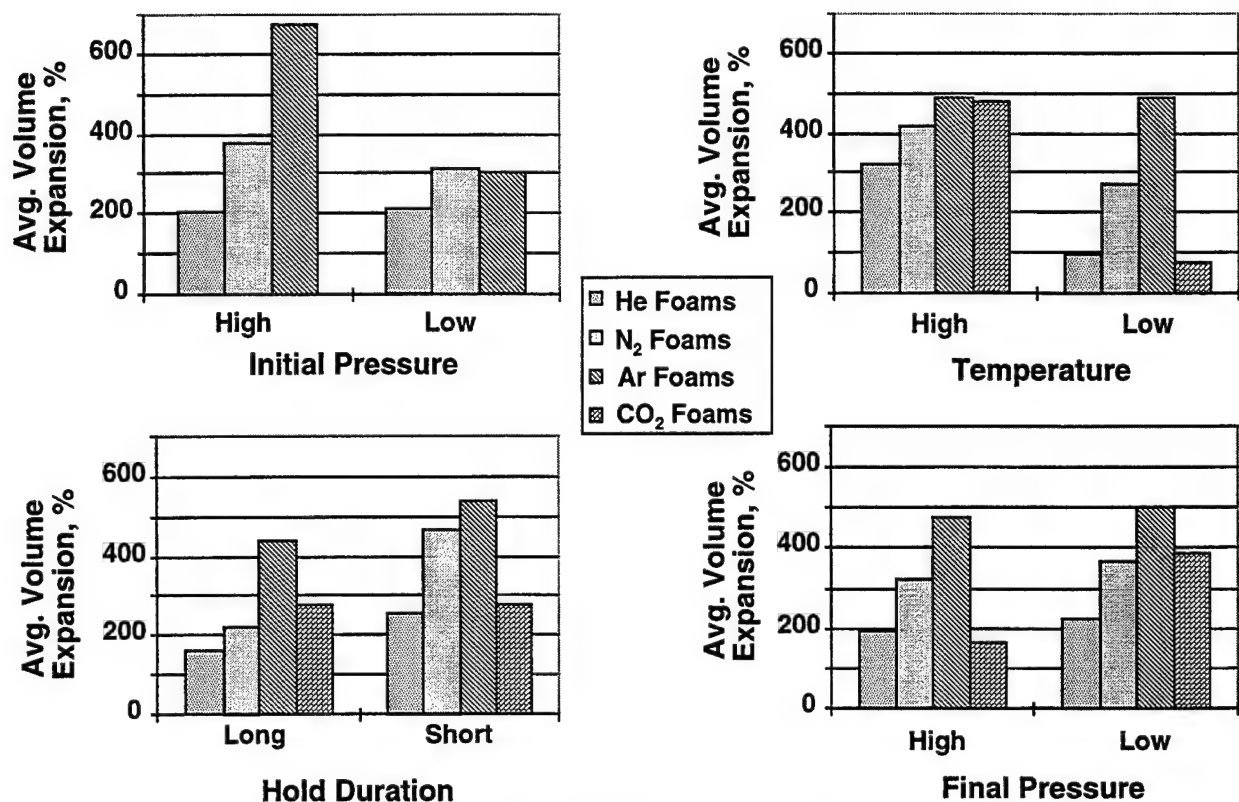


Figure 70. Volume Expansion during Foaming.

(i.e. all the samples at high initial pressure were averaged together, even though those samples had two foams at high temperature and two at low temperature, etc.).

The porosity data followed the expansion data directly although not to the same scales as shown in Figure 71. The bulk density was inversely related to those measurements as shown in Figure 72.

For the noninteractive gases (CO<sub>2</sub> was interactive), the first thing to note is that “final” pressure has little effect. The hold duration also did not have a large influence. The “initial” pressure shows a molecular mass effect of the gases; the larger mass produced more expansion at higher pressure while smaller masses (progressively) expanded less. At higher temperatures the lightweight gases expand more than at the lower temperatures, while the heavier gas (argon) expanded the same independent of temperature.

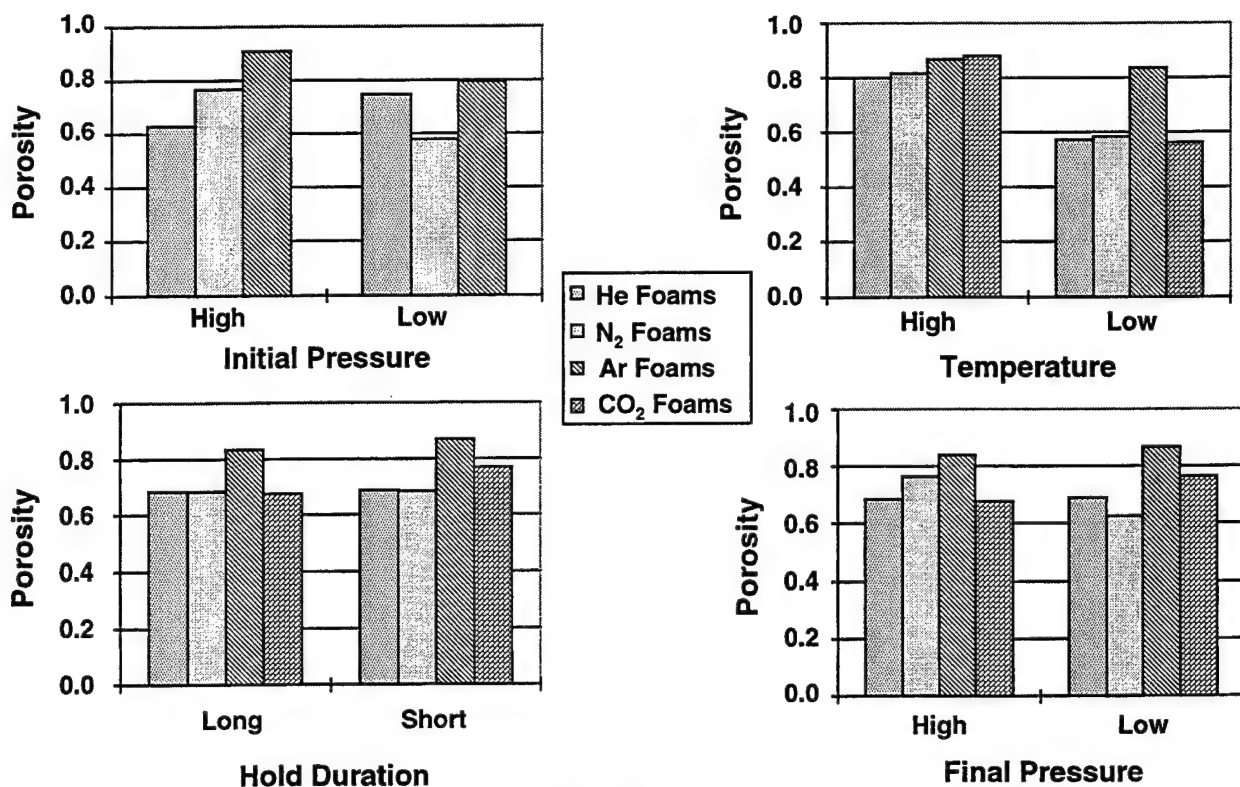


Figure 71. Porosity Data for the Foams.

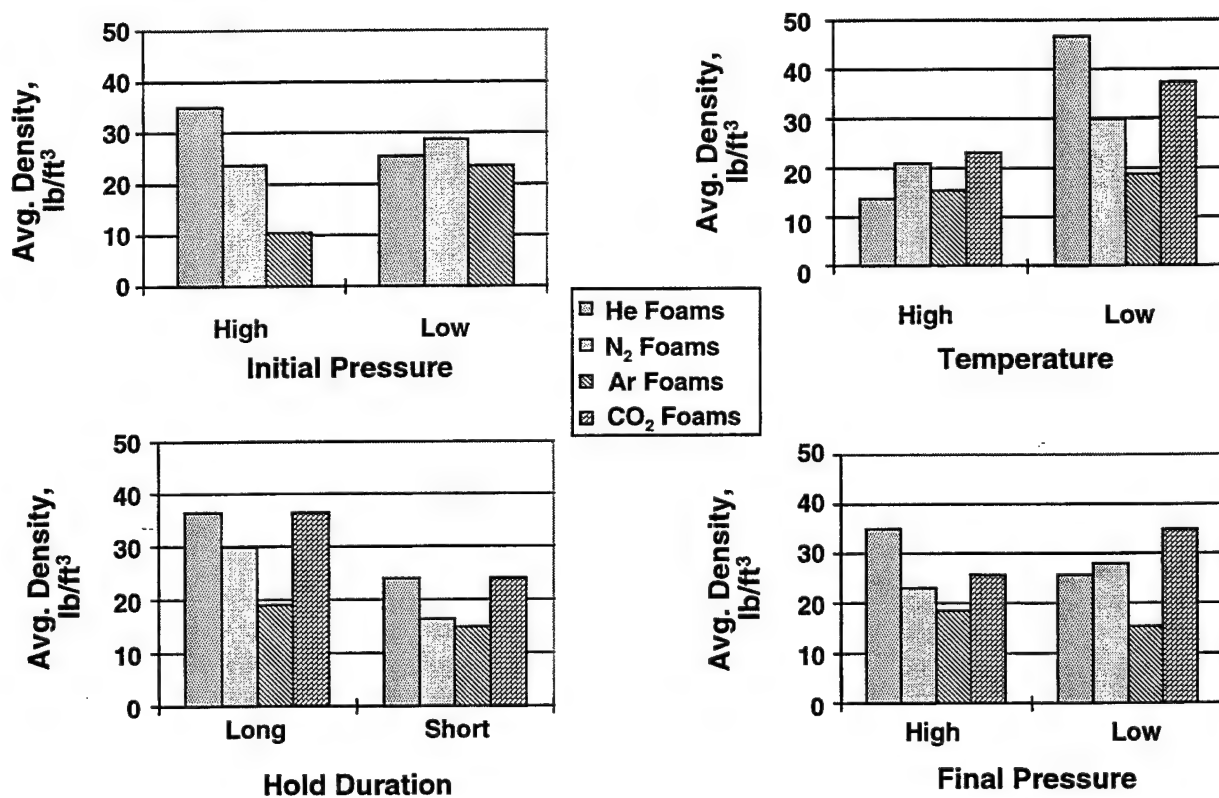


Figure 72. Bulk Density Results for the Foams.

One theory to explain this data is that the gas penetrates the interstitial spaces between particles in the disk preform during the initial pressurization and heat-up (~1-1/2 hours). At the higher temperature, either more spaces may be sealed off trapping more gas, or, more likely, the lower viscosity of the pitch offers less resistance to deformation when the pressure is reduced.

When the pressure is released several things occur:

- Gas molecules which can escape from the spaces do so.
- Gases that cannot escape cause the pitch to foam.
- Spaces that have connections large enough for the gases to flow between will coalesce into single bubbles.
- Eventually the foam expands to the point where the gas can escape to the outside rather than continuing to foam the pitch.

Because the spaces containing the foaming gas are already sealed off before the application of the final pressure, this parameter does not have an effect and the hold time is also irrelevant. The lower pitch viscosity at higher temperatures offers less resistance to expansion, so the volume increases more for the smaller molecules; it is harder for the larger molecules to escape so the temperature has less effect. Likewise at higher pressures the large molecules expand to their fullest extent, while the smaller gas molecules expand only until they can escape, regardless of the pressure which ends the foam expansion. A simple calculation of the volume expansion of the gases at the processing conditions shows that if full expansion occurs at the lower pressure to give 300 percent volume expansion, then the higher pressure would expand 750 percent, which is very close to that observed for argon.

The helium-blown foam does not produce an open-cell structure because it can more easily escape as the foam expands. The closed-cell foam that is produced is difficult to stabilize for further processing. Figure 73 shows fluorescent microscopy pictures of two helium-blown foams; the foam in 73b clearly shows bubble collapse. The cells of the helium-blown foams appear much larger than those formed from nitrogen blowing. This is consistent with the explanation of the gas in the pitch either blowing a foam with coalesced bubbles or it escapes. The amount of gas in any given final bubble will be dependent on how much coalescence occurs; helium should be subject to the most coalescence. Also when expanding, the helium can escape easier because of its small size leaving closed cells. Since argon is larger than He or N<sub>2</sub>, it cannot easily escape and so it continues to expand the pitch longer. This also is indicated by the overall higher porosity of the argon foam.

Initial gas pressure was not included in the CO<sub>2</sub> foam study, because there was insufficient pressure to achieve the highest final pressure. Therefore, an initial pressure was chosen to give the desired final pressure. The major observation from the CO<sub>2</sub> foams is the very small cell sizes at the lower temperature (largest change for all the gases, see Figure 74). This also corresponds to a significantly larger volume expansion as well. Whether these results are from an increased amount of gas initially available at the higher temperature or the lower pitch viscosity is not known. The pressure effect on expansion is also opposite from what was expected from the noninteractive gases (higher pressure gave less expansion).

The helium molecule being very small produces a closed-cell structure possibly due to its ability to escape the pitch more rapidly than the other gases. The effusion rate (gas diffusion rate across a barrier) of helium is almost four times as fast as N<sub>2</sub> and Ar only 83 percent as fast. The larger argon molecules expand the pitch more and produce



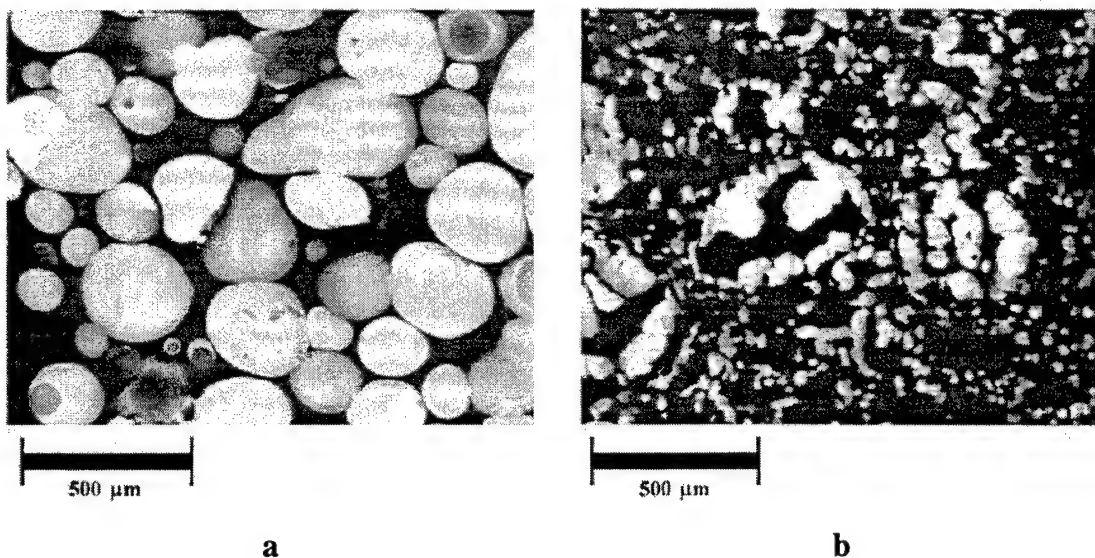


**Figure 73. Fluorescent Micrograph of Stabilized Helium Foams showing a) an Open Cellular Structure and b) a Collapsed Cellular Structure.**

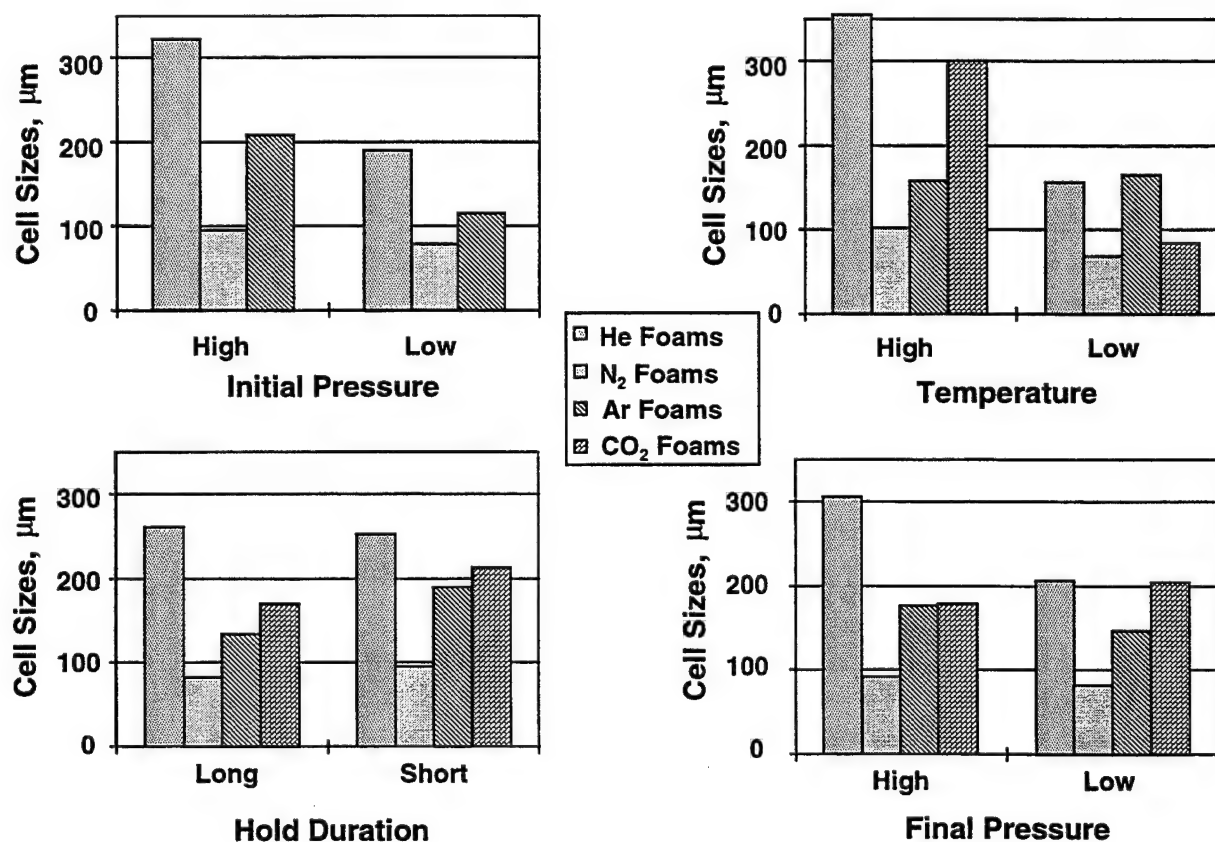


**Figure 74. Cell Size Results for the Foam Samples.**



larger, more open cells than nitrogen. The higher temperature gives more expansion probably from the lower pitch viscosity. More expansion occurs at higher pressure probably due to more gas being available to expand the pitch. The CO<sub>2</sub> foams cannot be easily explained in the same fashion and need to be studied in more detail. Further efforts will concentrate on determining the mechanism in which these foams are being produced.

#### 4.2.3 Foam Structural Modeling

A state-of-the-art CAD program (Design CAD 97) was evaluated by drawing progressive foam growth according to the modeling principles established several years ago [59]. The CAD program was found to easily accomplish the task of visualizing the bubble growth. The drawings more clearly showed the enormous strain which aligns the basic structural units of the pitch during initial bubble growth (see Figure 75). The drawings were also able to show breakthrough of the cell walls to form an open-celled structure. The change from having a balance of material in the strut and juncture up to near 90 percent porosity and the juncture-heavy structure at higher porosities was visualized for the first time; structural foams with porosities above 90 percent will clearly not be efficient.

#### 4.2.4 X-ray Diffraction of Graphitic Foams from Several Sources

In order to determine the effects of heat treatment (HT) on the AR foam strut properties, a series of AR fibers were heat treated to temperatures from 300°C up to 2875°C by a summer faculty. These fibers were examined by x-ray diffraction (XRD) and the results plotted against the HT temperature. The d-spacings were found to fall linearly with HT temperature from amorphous carbon to 80 percent graphite (see Figure 76). At the same time the crystallite sizes changed very little up to 1200°C and then rapidly increased in

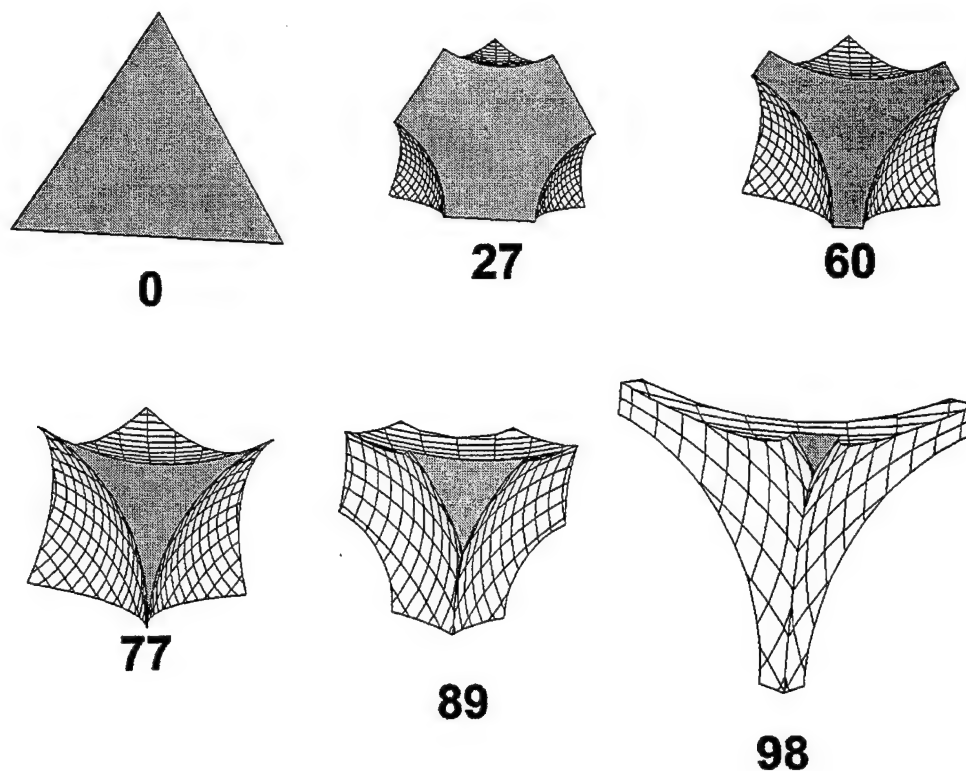


**Figure 75. Model Results for a Constant Volume Strut Expanding. The numbers are the percent porosity in the models with breakthrough to open cells at the 77% porosity level.**

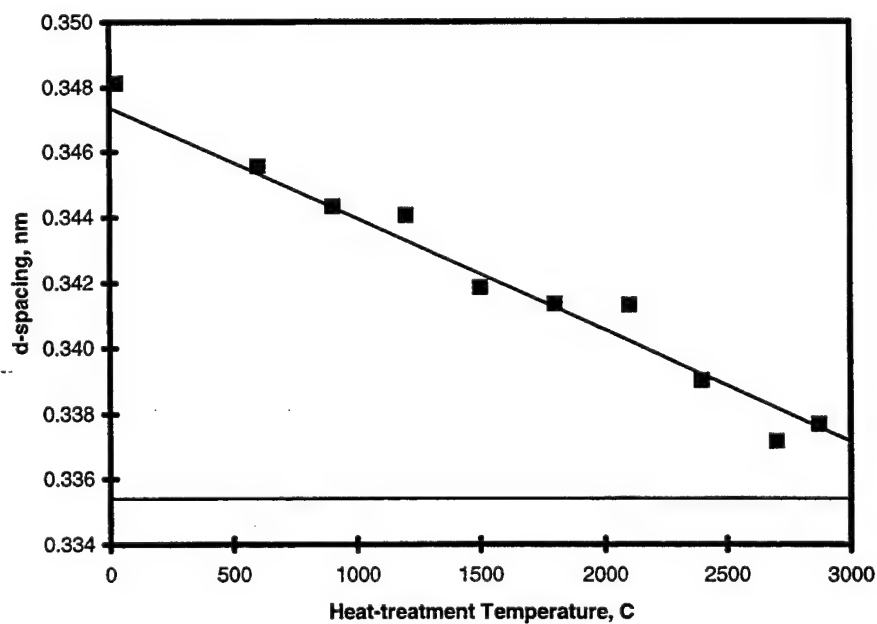


**Figure 76. D-Spacing versus Heat-Treatment Temperatures in AR Pitch-Based Fibers.**

size up to 2400°C to near the limit of resolution (~25 nm) (see Figure 77). The orientation increase followed the crystallite size trends.

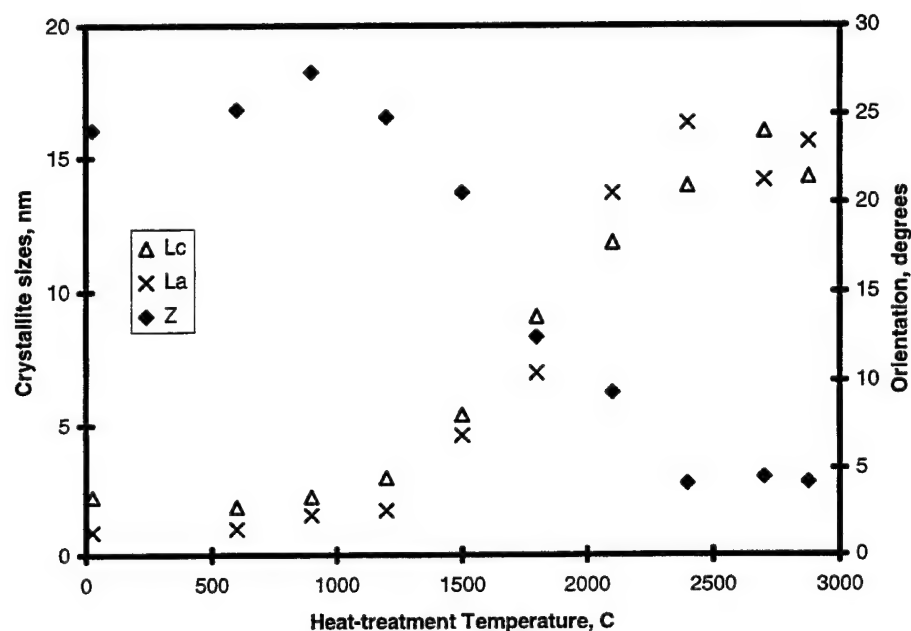


**Figure 77. Crystallite Sizes and Orientations versus Heat-Treatment Temperatures in AR Pitch-Based Fibers.**

### 4.3 Technical Assessment of Critical AF Materials Issues and Opportunities

Two major technical assessment reports were completed on critical Air Force materials issues and opportunities: (a) competitive uses of bulk pyrolytic graphite (PG) and carbon-carbon composite (CCC) materials for satellite and aerospace thermal management of electronic waste heat; and (b) the influence of 650°C (1200°F) aerodynamic air on the mechanical properties of CCC structural materials.

PG plates have been used for many years in various satellite passive thermal protection schemes. PG, with the proper microstructure, has a very high room-temperature thermal conductivity (k) in the a-b direction, i.e. parallel to the flat surface of the chemically

vapor-deposited (CVD) plate. Typical values range from about 190 to over 1300 W/m-K in the a-b direction and only a very small fraction of these values in the "c" direction, i.e. perpendicular to the surface of the flat plate. PG has other properties and characteristics of interest, including (a) high thermal stability, (b) low density, (c) high mechanical properties in-plane, (d) low-to-no outgassing, (e) moderate specific heat, (f) moderate costs, and (g) other features. High thermal conductivity (high-k) CCC materials are increasingly becoming more competitive with bulk PG. In the plane of reinforcement, the k value of mesophase pitch-based fiber-reinforced CCC materials were about 724 W/m-K for a density of 1.89 g/cm<sup>3</sup>. For satellite systems where specific properties are important, the high-k CCC materials have performance features exceeding those of PG. In summary, it was concluded that PG plates are optimum for heat sink/thermal transport when thick plates can be tolerated. On the other hand, high-k CCC plates are preferred for electronic applications involving thin plates. Additional information is contained in the UDRI Assessment Report No. 98-05, *Pyrolytic Graphite and Carbon-Carbon Composite Materials for Satellite Thermal Management*, authored by Mr. D. Schmidt, June 12, 1998.

CCC materials are unique structural materials at high temperatures, but in the presence of oxidizing species, their mechanical properties are lowered. The magnitude of the degradation has been quantified in limited cases, but for the most part there is an incomplete understanding of this phenomenon.

An investigation of all relevant factors was conducted, including basic science, experimental data, and prototype evaluations. Oxidation of CCC materials results in mass loss, which in turn may influence other composite properties such as mechanical properties. In general, oxidative carbon loss from the CCC material at 650°C (1200°F) takes place on

and near the surface region. At higher temperatures oxygen penetrates into the interior via pores and microcracks, and then attacks the various forms of carbon encountered.

Preferential loss of the carbonaceous forms is typically observed, particularly at the interface regions of the fiber-matrix and fiber bundle regions. The addition of particulate inhibitors reduces substrate (below the surface) oxidation, but certain mechanical properties may be degraded due to the presence of the fillers. After exposure to high-temperature oxidation, the particulate-containing CCC materials exhibited higher matrix-dominated mechanical properties (interlaminar shear strength, interlaminar tensile strength, and in-plane shear modulus). The composite in-plane tensile strength was sharply reduced, but the in-plane compressive strength was reduced only slightly. Improved mechanical properties were attributed to the formation of glassy phases from the particulate oxidation inhibitors. The situation is quite complex, but for those interested in more details, please refer to UDRI Assessment Report No. 98-04, *Influence of 650°C (1200°F) Air on the Mechanical Properties of Carbon-Carbon Composite Materials*, authored by D. L. Schmidt, April 30, 1998.

## **5. PUBLICATIONS AND PRESENTATIONS**

The following is a list of presentations and publications that were generated during this contractual period.

Kearns, K. M., D. P. Anderson, & H. J. Anderson. (1998). Structural Graphitic Carbon Foams. In D. S. Schwartz, D. S. Shih, A. G. Evans, & H. N. G. Wadley, eds., *Porous and Cellular Materials for Structural Applications, Proc. of Mater. Res. Soc. 521* (185-190).

Anderson, D. P., K. M. Kearns, C. Tucci, & G. Mestemaker. (1998). The Cellular Structure of Net-Shaped Pitch-Based Microcellular Carbon-Foams. *Proc. of 43<sup>rd</sup> ISSE*.

- Anderson, H. J., D. P. Anderson, & K. M. Kearns. (1998). Microcellular Pitch-Based Carbon-Foams Blown with Helium Gas. Proc. of 43rd ISSE.
- Roy, A. K., D. Pullman, and K. M. Kearns. (1998). Experimental Methods for Measuring Tensile and Shear Properties of Graphitic Foam. Proc. of 43rd ISSE.
- Anderson, D. P., C. W. Williams, Jr., & K. M. Kearns. (1998). Problems Associated with Making Composites from a Series of Allyl- and Propargyl-Substituted Cyclopentadiene Resins. Proc. of 43rd ISSE.
- Whitney, J. M. (1998). Effect of Transverse Ply Cracks on the Effective Thermal Expansion Coefficients of Bidirectional Laminates. In R. F. Gibson and G. M. Newaz, eds., Proc. of 8th Japan-US Conf. on Composite Materials (167-176). Lancaster, PA: Technomic Publishing Co.
- Whitney, J. M. (1998). Stress Analysis of Cylindrical Composite Lap Joints. Proc. of 39th AIAA/ASME/ASCE/AHS/ASC Structures, Structural Dynamics, and Materials Conf., Part 2 (1589-1593). Reston, VA: AIAA.
- Forte, M. S., J. M. Whitney, & N. J. Pagano. (1998). Influence of Adhesive Reinforcement on the Mode I Fracture Toughness of a Bonded Joint. Proc. of 39th AIAA/ASME/ASCE/AHS/ASC Structures, Structural Dynamics, and Materials Conf., Part 2 (1605-1615). Reston, VA: AIAA.
- Whitney, J. M. (1998). Effect of Load Distribution and Placement in the Iosipescu Shear Test. J. of Reinf. Plas. and Compos. 17(1) (26-38).
- Whitney, J. M. (1997). Analysis of a Composite Notched-Lap Joint Using Higher Order Plate Theory. ). In R. F. Gibson and G. M. Newaz, eds., Proc. of the ASC 12th Tech. Conf. (746-755). Lancaster, PA: Technomic Publishing Co.
- Han, K., C. W. Lee, & B. Rice. (1998). Permeability Measurements of Fiber Preforms for Aerospace Applications. Proc. of ASC 13th Tech. Conf.
- Crasto, A., & R. Kim. (1998). On the Estimation of Shrinkage and Thermal Strains During Composite Cure. Proc. of 8th Japan-US Conf. on Composite Materials.
- Kim, R., & G. P. Tandon. (1998). Interfacial Normal Strength Evaluation in Unidirectional AS4/Epoxy Composites. Proc. of 8th Japan-US Conf. on Composite Materials.
- Roy, A. K. (1998). Three-Dimensional Mixed Variational Micromechanics Model for Textile Composites. Proc. of AIAA SDM Conf.
- Roy, A. K., & S. L. Donaldson. (1997, November). Experimental Investigation of Crack-Front Profile in Bonded Composite Materials. Presented at ASME/IMECE, Dallas, TX.

Thorp, K. E. G., & A. S. Crasto. (1998). Accelerated Hygrothermal Aging of Polyimides in Saturated Steam at Elevated Pressure. *Proc. of High Temple Workshop XVIII*.

Crasto, A. S., & R. Y. Kim. (1998). Hygrothermal Degradation of Polyimides and Its Influence on Mechanical Properties. *Proc. of High Temple Workshop XVIII*.

## 6. REFERENCES

1. Crasto, A. S., R. Y. Kim, C. Fowler, & J. P. Mistretta. (1996). Rehabilitation of Concrete Bridge Beams with Externally-Bonded Composite Plates (Part I). *Int. Conf. on Composites in Infrastructure 1* (857).
2. Crasto, A. S., R. Y. Kim, & J. P. Mistretta. (1996). Rehabilitation of Concrete Bridge Beams with Externally-Bonded Composite Plates (Part II). *Int. SAMPE Symp. 41* (1269-1279).
3. Crasto, A., R. Y. Kim, J. P. Mistretta, & M. Dougherty. (1997). Rehabilitation of Concrete Bridge Beams with Fiber-Reinforced Composites. *Int. SAMPE Symp. 42*.
4. Shyprekevich, P. (1995). Characterization of Bolted Joint Behavior: MIL-HDBK-17 Accomplishments at Standardization. *J. of Composites Tech. & Research 17*(3) (260-270).
5. Lekhnitskii, S. G. (1968). *Anisotropic Plates*. Gordon and Breach Science Publishers.
6. Iarve, E. V. (1996). Spline Variational Three-Dimensional Stress Analysis of Laminates with Open Holes. *Int. J. of Solids & Structures 33*(14) (2095-2118).
7. Iarve, E. V. (1995). Three-Dimensional Stress Analysis of Fastener Hole Composites. *IMECE, AMD-Vol. 69-1*, Amer. Soc. of Mech. Eng.
8. Park, C. H., & H. L. McManus. (1994). Thermally-Induced Damage in Composite Space Structures: Predictive Methodology and Experimental Correlation. *Proc. of Amer. Soc. of Composites 9* (161-168).
9. McManus, H. L., D. E. Bowles, & S. S. Tompkins. (1996). Prediction of Thermal Cycling Induced Matrix Cracking. *J. Reinforced Plast. Compos. 15* (124-139).
10. Kim, R. Y., & A. S. Crasto. (1995). Dimensional Stability of Composites in Space: CTE Variations and their Prediction. *Proc. Int. Conf. Compos. Mater. (ICCM-10, Vol. IV, p. 513)*.
11. Pagano, N. J. (1998). On the Micromechanical Failure Modes in a Class of Ideal Brittle Matrix Composites, Part 1: Coated-Fiber Composites. *Composites Part B 29B* (93-119).

12. Tandon, G. P., & R. Y. Kim. (1997). Test Methods for Estimation of Interfacial Normal Strength in Unidirectional Fiber Reinforced Composites. *J. of Reinforced Plastics & Composites* 16(17) (1550-1565).
13. Gundel, D. B., B. S. Majumdar, & D. B. Miracle. (1995). Evaluation of the Intrinsic Transverse Response of Fiber-Reinforced Composites Using a Cross-Shaped Geometry. *Scripta Metall.* 33 (2057).
14. Tandon, G. P., R. Y. Kim, S. G. Warrier, & B. S. Majumdar. (1997). Influence of Edge Effects in Estimating Interfacial Normal Strength in Model Unidirectional Composites. *Proc. of Amer. Soc. for Composites 12th Tech. Conference* (1176-1185). Technomic Publishing Co., Inc.
15. Majumdar, B. S., D. B. Gundel, R. E. Dutton, S. G. Warrier, & N. J. Pagano. (In Press). Evaluation of the Tensile Interface Strength in Brittle Matrix Composite Systems. *J. of Amer. Ceramic Society*.
16. Highsmith, A. L., & K. L. Reifsnider. (1982). Stiffness-Reduction Mechanisms in Composite Laminates. Damage in Composite Materials (ASTM STP 775). In K. L. Reifsnider, ed., *American Society for Testing and Materials* (103-117).
17. Lee, J. W., & I. M. Daniel. (1990). Progressive Cracking of Cross-Ply Composite Laminates. *J. of Composite Materials* 24 (1225-1242).
18. Tsai, C. L., & I. M. Daniel. (1992). The Behavior of Cracked Cross-Ply Composite Laminates under Shear Loading. *Int. J. of Solids and Structures* 29 (3251-3267).
19. Hashin, Z. (1985). Analysis of Cracked Laminates: A Variational Approach. *Mechanics of Materials* 4 (121-136).
20. Nuismer, R. J., & S. C. Tan. (1988). Constitutive Relations of a Cracked Composite Lamina. *J. of Composite Materials* 22 (306-321).
21. Tao, J. X., & C. T. Sun. (1996). Effect of Matrix Cracking on Stiffness of Composite Laminates. *Mechanics of Composite Materials and Structures* 3 (225-239).
22. Yuan, F. G., & M. C. Selek. (1993). Transverse Cracking and Stiffness Reduction in Composite Laminates. *J. of Reinforced Plastics and Composites* 12(9) (987-1015).
23. Schoeppner, G. A., & N. J. Pagano. (1998). Stress Fields and Energy Release Rates in Cross-Ply Laminates. *Int. J. of Solids and Structures* 35(11) (1025-1055).
24. Pagano, N. J., & G. A. Schoeppner. (1997). Some Transverse Cracking Problems in Cross-Ply Laminates. *Proc. of the 38th AIAA /ASME/ASCE/AHS/ASC Structures, Structural Dynamics, and Materials Conference*.



25. Pagano, N. J. (1978). Stress Fields in Composite Laminates. *Int. J. of Solids and Structures* 14 (385-400).
26. Schoeppner, G. A., & N. J. Pagano. (1998). Stress Fields and Energy Release Rates in Cross-Ply Laminates. *Int. J. of Solids and Structures* 35(11) (1025-1055).
27. Pagano, N. J., & G. A. Schoeppner. (1997). Some Transverse Cracking Problems in Cross-Ply Laminates. (1997). *Proc. of the 38th AIAA /ASME/ASCE/AHS/ASC Structures, Structural Dynamics, and Materials Conference*.
28. Pagano, N. J. (1978). Stress Fields in Composite Laminates. *Int. J. of Solids and Structures* 14 (385-400).
29. Anderson, G. P., S. J. Bennett, & K. L. DeVries. (1977). *Analysis and Testing of Adhesive Bonds* (11-12). New York: Academic Press.
30. Zhang, Y. C., & J. Harding. (1990). A Numerical Micromechanics Analysis of the Mechanical Properties of a Plain Weave Composite. *Computers and Structures* 36(5) (839-844).
31. Naik, N. K., & V. K. Ganesh. (1992). Prediction of On-Axes Elastic Properties of Plain Weave Fabric Composites. *Composites Science and Technology* 45 (135-152).
32. Hahn, H. T., & R. Pandey. (1994). A Micromechanics Model for Thermoelastic Properties of Plain Weave Fabric Composites. *J. Eng. Materials & Technology* 116(4) (517-523).
33. Yurgartis, S. W., & J. P. Maurer. (1993). Modeling Weave and Stacking Configuration Effects on Interlaminar Shear Stresses in Fabric Laminates. *Composites* 24 (651-658).
34. Marrey, R. V., & B. V. Sankar. (1995). *Micromechanical Models for Textile Structural Composites* (NASA CR 198229).
35. Chou, T., & F. K. Ko. (1989). *Textile Structural Composites, Chapter 7*. New York: Elsevier.
36. Naik, N. K., & V. K. Ganesh. (1994). Failure Behavior of Plain Weave Fabric Laminates Under In-Plane Shear Loading. *J. of Composites Technology & Research* 16(1) (3-20).
37. Karayaka, M., & P. Kurath. (1994). Deformation and Failure Behavior of Woven Composite Laminates. *J. of Engineering Materials & Technology* 116(2) (222-232).
38. Whitcomb, J. D. (1991). Three-Dimensional Stress Analysis of Plain Weave Composites. In T. K. O'Brien, ed., *Composite Materials: Fatigue and Fracture (3rd*

Vol) (ASTM STP 1110, 417-438). Philadelphia, PA: American Society for Testing and Materials.

39. Roy, A. K. (1994). Experimental Observation of Damage in 8HS Fabric Composites in Tensile Loading. *Proc. 9th Technical Conference, American Society for Composites* (1273-1280). Lancaster, PA: Technomic Publishing.
40. Roy, A. K. (1996). In Situ Damage Observation and Failure in Model Laminates Containing Planar Yarn Crimping of Woven Composites. *Mechanics of Composite Materials and Structures* 3 (101-117).
41. Roy, A. K. (In Press). Comparison of In Situ Damage Assessment in Unbalanced Fabric Composite and Model Laminate of Planar (One-Directional) Crimping. To appear in *J. of Composites Science and Technology*.
42. Reissner, E. (1950). On a Variational Theorem in Elasticity. *J. of Mathematics and Physics* (90-95).
43. Crasto, A. S., & R. Y. Kim. (1993). On the Determination of Residual Stresses in Fiber-Reinforced Thermoset Composites. *J. of Reinforced Plastics and Composites* 12 (545).
44. Pagano, N. J., & H. T. Hahn. (1977). Evaluation of Composite Curing Stresses. *Composite Materials: Testing and Design (Fourth Conference)* (ASTM STP 617, 317-329).
45. Daniel, I. M., J. L. Mullineaux, F. J. Ahimaz, & T. Liber. (1972). The Embedded Strain Gage Technique for Testing Boron/Epoxy Composites. *Composite Materials: Testing and Design (Second Conference)* (ASTM STP 497, 257-272).
46. Daniel, I. M., T. Liber, & C. C. Chamis. (1975). Measurement of Residual Strains in Boron-Epoxy and Glass-Epoxy Laminates. *Composite Reliability* (ASTM STP 580, 340-351).
47. Daniel, I. M., & T. Liber. (1977). Lamination Residual Strains and Stresses in Hybrid Laminates. *Composite Materials: Testing and Design (Fourth Conference)* (ASTM STP 617, 317-329).
48. White, S. R., & H. T. Hahn. (1990). Mechanical Property and Residual Stress Development during Cure of a Graphite/BMI Composite. *Polymer Engineering and Science* 30(22) (1465).
49. Crasto, A. S., et al. (1998). *Core Programs of High-Performance Composite Materials* (AFRL-ML-WP-TR-1998-4021) (82-83). Dayton, OH: U.S. Air Force.

50. Anderson, D. P., M. I. Martinez, A. K. Roy, G. J. Tregre, & L. J. Mathias. (1997). Carbon-Carbon Composites from a New Class of High-Char Yield Resins. *23rd Biennial Conference on Carbon Extended Abstracts II* (476).
51. Mathias, L. J., & J. Muthiah. (1994). Synthesis and Characterization of a New Class of Thermosetting Resin: Allyl and Propargyl Substituted Cyclopentadiene Derivatives. *Polymer Composites 15* (464).
52. Mathias, L. J., & G. J. Tregre. (1997). Synthesis, Cure Analysis, and Composite Properties of Allylated Cyclopentadiene Resins. *Polymer Composites 18* (509).
53. Anderson, D. P., C. W. Williams, Jr., & K. M. Kearns. (1998). Problems Associated with Making Composites from a Series of Allyl- and Propargyl-Substituted Cyclopentadiene Resins. *Proc. of SAMPE 43rd ISSE*.
54. Hall, R. B., & J. W. Hager. (1993). Graphitic Foams as Potential Structural Materials. *21st Biennial Conference on Carbon Extended Abstracts* (100).
55. Kearns, K. M., & D. P. Anderson. (1997). Microcellular Graphitic Foam Processing. *Proc. of ICCM-11* (825).
56. Anderson, D. P., K. M. Kearns, C. Tucci, & G. Mestemaker. (1998). The Cellular Structure of Net-Shaped Pitch-Based Microcellular Carbon-Foams. *Proc. of SAMPE 43rd ISSE*.
57. Anderson, H. J., D. P. Anderson, & K. M. Kearns. (1998). Microcellular Pitch-Based Carbon-Foams Blown with Helium Gas. *Proc. of SAMPE 43rd ISSE*.
58. Kearns, K. M., D. P. Anderson, & H. J. Anderson. (1998). Structural Graphitic Carbon Foams. In D. S. Schwartz, D. S. Shih, A. G. Evans, & H. N. G. Wadley, eds., *Porous and Cellular Materials for Structural Applications*. *Proc. Mater. Res. Soc.* 521 (185-190).
59. Anderson, D. P., K. E. Gunnison, & J. W. Hager. (1992). Ligament Structure of Open-Cell Carbon Foams and the Construction of Models Based on that Structure. In C. L. Renschler, J. J. Pouch, & D. M. Cox, eds., *Novel Forms of Carbon*. *Proc. Mater. Res. Soc.* 270 (47-52).